Liquid Film Formation and Heat Transfer Characteristics of a Liquid Jet Obliquely Impinging onto a Wall

Noritaka Sako

Contents

Chapter 1 Introduction

Bipropellant thrusters are used for orbit maneuvering and attitude control of satellites and small size spacecraft. In bipropellant thrusters, a liquid film cooling technique is employed to protect the chamber wall from high-temperature combustion gases. In the present thesis, the formation processes of the liquid film by a liquid jet impingement are discussed. Chapter 1 provides an introduction of the present study.

1.1 Background

In recent years, the space industry has made remarkable progress, and many countries around the world are making great efforts for space development. Additionally, private companies have been actively entering the market of the space industry, as seen in the example that Space X succeeded for the first time in human spaceflight as a private company. Therefore, the market size of the space industry is expected to exceed 100 trillion yen by 2040 [1] due to the increase in the number of countries engaged in space development and the expansion of commercial use of space.

One of space developments in Japan is represented in "Hayabusa" which succeeded in returning to Earth with planetary materials (sample return) from the asteroid "Itokawa" in 2010 [2]. The subsequent project of "Hayabusa2" succeeded in sample return from the asteroid "Ryugu" in 2020 very recently [3]. The next Japanese flagship launch vehicle H-III rocket [4] has planned to be launched, and new lander missions such as SLIM (Smart Lander for Investigating Moon) [5] and MMX (Martian Moons eXploration) [6] are also going to be conducted.

In the various missions mentioned above, rocket propulsion systems play an important role. Rocket propulsion systems are mainly classified into chemical rocket propulsion, nuclear rocket propulsion, and electric rocket propulsion, according to the types of energy sources [7, 8]. The following is an overview of the mechanism for each propulsion system.

1) Chemical rocket propulsion

In a chemical rocket propulsion system, the combustion reaction of the chemical propellant, which is generally a combination of a fuel and an oxidizer, occurs, and then, the high-temperature combustion gases are accelerated through a nozzle to produce thrust. Chemical rocket engines are used most commonly for any kind of mission because they cover a varied range of thrust by types of chemical propellants.

2) Nuclear rocket propulsion

In a nuclear propulsion system, the thermal energy from the nuclear reaction is transferred into the propellant to produce a high-speed jet. In the past, some ground tests were conducted, but nuclear rocket engines are expected not to be further investigated from the viewpoint of public concerns about the spreading of radioactive materials.

3) Electric rocket propulsion

In electric rocket propulsion systems, thrust is produced from electric energy whose source originates in nuclear, solar radiation, or batteries. The three basic types (electrothermal, ion, and electromagnetic propulsion) are included in electric rocket propulsion systems. The specific impulse I_{sp}, which is a key indicator of the rocket performance, takes a higher value than in chemical propulsion, while obtained thrust is limited to a relatively low value.

There are several propulsion systems other than those mentioned above, but the chemical rocket propulsion system is currently the common one. Therefore, the present study focuses on chemical rocket propulsion. The next section outlines the classification of rocket engines using a chemical rocket propulsion system.

1.2 Rocket engine with chemical propulsion system

Rocket engines using a chemical propulsion system are classified into liquid or solid propellant rockets depending on the phase state of the propellant.

Rocket engines with solid propellants are commonly called as solid propellant rocket "motors" [7, 8]. In solid propellant rocket motors, propellants are stored in the combustion chamber as "*grain*", which means the solid body of the hardened propellant and occupies a large portion of the total motor mass (82-94%). The propellants can be directly stored within the combustion chamber for a long time (5-20 years). In addition, solid propellant rocket motors are easily mounted owing to their simple structure and can produce a large thrust compared to liquid propellant rockets. On the other hand, the specific impulse is lower than that of the liquid propellant rockets, and the thrust is difficult to control because the combustion reactions proceed automatically when it is ignited. Therefore, solid propellant rocket motors are mainly used to support launching a rocket as a booster. From the viewpoint that fine adjustment of thrust is needed for such as attitude control of

spacecraft, the liquid propellant rocket is rather favorable.

Liquid propellant rockets are classified into monopropellant and bipropellant rocket engines. Monopropellant rocket engines generate thrust by producing high-temperature gases from the decomposition reaction of monopropellants such as hydrogen peroxide and hydrazine under catalysts, heating, or pressurization. Since the monopropellant rocket engine has simple supply and control system of propellants, it has been applied to practical use. However, the obtained thrust and specific impulse of the monopropellant rocket are low. Thus, the monopropellant rocket is used as secondary power sources and have limited applications. In contrast, bipropellant rocket engines can produce a wider range of thrust by the combustion reactions from the combinations of liquid fuels and liquid oxidizers. Additionally, they are easily controlled owing to their ability to interrupt and restart combustion. Because of these advantages, bipropellant rocket engines are mainly used in many rocket engines.

For the attitude control and orbit maneuvering of satellites and small-scale spacecraft, small bipropellant rocket engines, which are called bipropellant thrusters, have been generally used due to their large thrust (from ten to several hundreds of newtons [9]) and ability to repeat the start and stop operations of the combustion. Bipropellant thrusters have ever been employed in many satellites and small spacecraft such as Hayabusa [2], HTV (H-II Transfer Vehicle) [10], and Hayabusa2 [3] and are planned to be applied in the next-generation spacecraft such as HTV-X [11], SLIM, and MMX [12]. To accomplish the next space missions with higher difficulty, higher performance and reliability of bipropellant thrusters are strongly required. For achieving higher performance and reliability, it is necessary to investigate the phenomena occurring in the thrusters and reveal the important factors for the phenomena among the numerous design factors.

1.3 Key physical phenomena inside bipropellant thruster

Bipropellant thrusters are operated using both steady-state and pulse firing mode. The time scales of steady state firing mode ranges $O(10^1\text{-}10^3)$ s, while that of pulse firing mode is $O(10^{-2}\text{-}10^{-1})$ s [13]. In the bipropellant thrusters, a combination of a hydrazine-derivative fuel [(e.g. hydrazine (N_2H_4), monomethylhydrazine (MMH and CH_3NHNH_2), unsymmetrical dimethylhydrazine (UDMH and $(CH_3)_2NNH_2$)) and nitrogen tetroxide (NTO and N_2O_4) is favorable to use because these combinations react and auto-ignite immediately after contact of liquid fuel and liquid oxidizer without any ignition sources even at low pressures and temperatures [14-16]. This unique feature of chemical reaction is called "hypergolicity" [7, 17]. To take advantage of hypergolicity, unlike-impingement

type injectors are generally employed in bipropellant thrusters [7] as shown in Fig. 1.1. Additionally, a part of the liquid fuel is injected onto the chamber wall for the cooling of the chamber. The injector and chamber are carefully designed to achieve high performance in the steady-state mode, fast ignition response in the pulse mode, and high heat resistance. However, the development of thrusters primarily relies on the conduction of multiple cost- and time-intensive tests because the complicated multi-physics phenomena occurring in the combustion chamber remain insufficient in terms of in-depth understanding [18]. Therefore, the design and development process based on an understanding of physical phenomena, independent of the time-and-cost-consuming hot firing test, is desirable.

As mentioned above, a series of complex physical phenomena, which include impinging atomization and spray formation, liquid phase reaction in the vicinity of the impingement point, evaporation, mixing of fuel and oxidizer gas, combustion and liquid film cooling, simultaneously occur inside the chamber of bipropellant thrusters as shown in Fig. 1.1. With a deeper understanding of the phenomena, optimal design or new design concepts of the thrusters can be developed without the need for numerous combustion tests. Therefore, studies mainly on impinging atomization, combustion reaction of hypergolic propellants, and liquid film cooling have been conducted. The following is an overview of previous research on the above topics.

1.3.1 Impinging atomization

Liquid atomization means the transformation of a bulk liquid into sprays through a sequential process that a liquid jet or a liquid film is formed from a bulk liquid by external force and eventually disintegrates into ligaments and then sprays by the growth of small disturbances [19, 20]. In bipropellant thrusters, sprays are formed through the impingement of liquid jets leading to liquid sheet formation, the breakup of the sheet into ligaments, and then disintegration into droplets. The spray characteristics such as liquid sheet breakup length, mean diameter of droplets, droplet size distribution, and spray flux distribution are important information for predicting the performance of thrusters.

Many researches have been devoted to the spray characteristics of the impinging atomization. In this section, some of the major studies are introduced. Ryan et al. [21] experimentally investigated the droplet size distribution of the sprays formed by the impingement of both laminar and turbulent jets with the PDPA (Phase Doppler Particle Anemometry). They identified that the breakup length of the liquid sheet and droplet sizes were strongly affected by the initial conditions of the liquid jets; the sheet breakup length
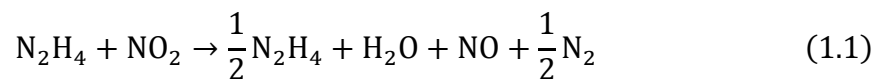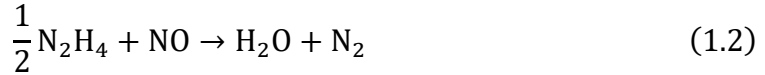
and the droplet sizes in the case of the turbulent jets impingement were shorter and smaller respectively than in the laminar jets impingement. They also developed the empirical correlations of the sheet breakup length and mean diameter of droplets following the existing empirical models. Inoue et al. [22] conducted numerical simulations with the CIP-LSM (CIP-based Level Set & Mars) method [23] to clarify the effect of the injection velocity distribution of the liquid jets on the atomization characteristics of the liquid sheet. They found that the non-uniform distribution of the injection velocity resulted in the velocity distribution with an inflection point in the liquid sheet, leading to the formation of the unstable liquid sheet and enhanced atomization. Strakey and Talley [24] investigated the effect of the ambient pressure on droplet sizes with the laser diffraction particle size analysis; the droplet sizes non-linearly decreased with the increase in the ambient pressure. Karikawa et al. [25] measured the droplet size and velocity with PDA (Phase Doppler flux of droplets was measured by using phase Doppler Anemometry) and simultaneously obtained spray flux distribution by using a two-dimensional patternator. They indicated that droplets were distributed not only in the in-sheet direction but also in the normal direction of the liquid sheet (i.e., sheet thickness direction). Recently, Inoue et al. [26, 27] measured the spray flux distribution with the 3D printed patternator and clarified the global length scale of the spray structure.

1.3.2 Combustion reaction of hypergolic propellants

As mentioned at the beginning of this chapter, bipropellant thrusters employ hypergolic propellants (especially the combinations of hydrazine (N_2H_4) or monomethylhydrazine (MMH and CH_3NHNH_2)/nitrogen tetroxide (NTO, N_2O_4)), which indicate the unique chemical reactions; the auto-ignition occurs upon contact with liquid fuel and oxidizer without any ignition devices. For improving the performance of thrusters and achieving stable combustion, chemical reactions and flame structures of hypergolic propellants have been extensively investigated. Here, some of the studies about them are described below.

For the chemical reactions, the reactions of hydrazine derivative fuels/nitrogen dioxide (NO_2) need to be discussed because NTO is instantaneously decomposed to NO_2 in the gas phase [28]. Sawyer [29] proposed the two-step global reaction mechanism of N_2H_4/ NO_2 as indicated in Eqs. (1.1) and (1.2), for the first time.

$$N_2H_4 + NO_2 \rightarrow \frac{1}{2}N_2H_4 + H_2O + NO + \frac{1}{2}N_2 \qquad (1.1)$$

$$\frac{1}{2} \mathrm{N_2H_4} + \mathrm{NO} \rightarrow \mathrm{H_2O} + \mathrm{N_2} \qquad (1.2)$$

Ohminami et al. [30] developed a detailed mechanism of $\mathrm{N_2H_4}$/ $\mathrm{NO_2}$ including 22 species and 61 reactions. In their model, combustion was initiated relying on the radical formation from the thermal decomposition of $\mathrm{N_2H_4}$, and auto-ignition phenomena under the conditions of low pressure and room temperature could not be predicted. For reproducing the auto-ignition phenomena, Daimon et al. [31] focused on the H atom abstraction reaction from $\mathrm{N_2H_n}$ (n = 1-4) by $\mathrm{NO_2}$, in which the reactions for n = 1-3 are exothermic and the heat released by the reaction for n = 1 is large owing to $\mathrm{N_2}$ production, and developed a detailed mechanism with 39 species and 268 reactions, which can predict the auto-ignition under low pressure and room temperature conditions. For MMH/$\mathrm{NO_2}$ reaction, Kanno et al. investigated rate coefficients of reactions related to MMH/$\mathrm{NO_2}$ [32] and developed a detailed mechanism with 119 species and 887 reactions [33].

Researches on the flame structures have been widely conducted, ranging from experiments on the single droplet to those under conditions close to the actual operation. Lawver [34] measured the temporal change of the temperature and diameter of the $\mathrm{N_2H_4}$ single droplet suspended from a thermocouple in an NTO vapor environment. In his experiment, two flame regions were observed around the droplet; the decomposition flame of $\mathrm{N_2H_4}$ on the inside and the oxidation flame in the outer region. Daimon et al. [35] conducted a high-speed imaging of a $\mathrm{N_2H_4}$ droplet falling into NTO liquid pool and obtained information about the probability and strength of explosions and the ignition delay. Hayashi et al. [36] experimentally and numerically investigated a counterflow pool flame of gaseous NTO and liquid MMH pool. From the high-speed image, two orange flames were observed on MMH and NTO sides, respectively. The luminescence on the fuel side was derived from NH$_2$* produced by MMH decomposition, while that on the oxidizer side was derived from $\mathrm{NO_2}$ recombination. Additionally, blue/white flame with CH* and OH* chemiluminescence appeared between two orange flames. Tani et al. [13] conducted high-speed imaging of liquid jet impingement of MMH and MON3 (NTO containing 3 wt% NO) and captured orange and blue/white flames. Tani et al. [37] and Daimon et al. [38] conducted Computational Fluid Dynamics (CFD) analysis of flame structures of $\mathrm{N_2H_4}$/NTO co-flowing gas jets and impinging gas jets respectively with the detailed mechanism [31]. Tani et al. confirmed two types of flames between co-flowing gas jets; diffusion flame derived from the oxidation of $\mathrm{N_2H_4}$ and flame from the thermal decomposition of $\mathrm{N_2H_4}$. Daimon et al. introduced the new flame indexes, which can determine the diffusion and decomposition flames, and captured both flames in impinging

gas jets.

1.3.3 Liquid film cooling

Thermal management is an important issue for developing liquid rocket engines [39], and therefore, some kinds of cooling techniques (regenerative cooling, film cooling, radiation cooling, transpiration cooling, ablative cooling, and so on) are applied by coupling some of them or alone to prevent chambers and nozzles from thermal failure [40]. Bipropellant thrusters employ a liquid film cooling technique, in which liquid fuel jets are injected from the injector faceplate (see Fig. 1.2) onto the combustion chamber wall and liquid films are formed to prevent the wall surface from being exposed to the high-temperature combustion gases [18] as shown in Fig. 1.1. The liquid films are gradually heated and evaporate as they move downstream due to the heat input from the combustion gases and the chamber wall, and eventually, dry-out at a certain axial position. For avoiding thermal failure, the chamber wall needs to be sufficiently cooled by the liquid films. However, the liquid films are considered to reduce the temperature of the combustion gases, leading to the performance loss of the rocket engines [41]. Additionally, the liquid films of fuel may not sufficiently mix with the core flow and eventually reach the chamber outlet without complete combustion, which results in reducing the thrust performance [42]. Actually, the specific impulse I_{sp} of rocket engines with film cooling was reduced in some experiments [43, 44, 45]. Inoue et al. [46] theoretically analyzed the effect of the film cooling ratio, which means the ratio of the mass flow rate of liquid fuel for film cooling to the total mass flow rate of liquid fuel, on the characteristic exhaust velocity c^* (performance indicator of the chemical rocket combustion chamber [7,8]); the maximum value of c^* monotonically decreases with the increase in the film cooling ratio. Therefore, the flow rate of fuel for liquid film cooling should be minimized and optimized while achieving sufficient cooling [41, 47].

One of the important indexes for evaluation of the cooling performance is the liquid film length, which is the length of the liquid-cooled region [48]. To predict the chamber wall temperature, and thus for better thermal management of bipropellant thrusters, the liquid film length needs to be predicted depending on the operation conditions. Stechman et al. [48] predicted the liquid film length by only considering the convective heat transfer from the combustion gases to the liquid film. Shine et al. [49] proposed a one-dimensional analytical model of liquid film length including the effects of not only the convective and radiative heat transfer but also gas-liquid interface instability due to the strong shear by the fast gas stream as experimentally visualized in [50, 51]. Recently, Inoue et al. [47]

developed the theoretical model for the evaporating liquid film, in which the three-dimensional wavy structure of the liquid film with role and ripple waves owing to Kelvin-Helmholtz and Rayleigh-Taylor instabilities resulted in the expansion of the heating area and the entrainment of the liquid droplets from the liquid film to the core flow.

Whereas the above theoretical models have advanced our understandings of the physical phenomena inherent in liquid film cooling, the above models do not account for heat transfer between the liquid film and the chamber wall. Grisson [52] pointed out that the absorbed heat in the wall was transferred to the liquid film by boiling, which could cause the burnout of the liquid film. Purohit et al. [53] numerically predicted the temperature distribution of the chamber wall of a bipropellant thruster with liquid film cooling. In their calculation, the convective, nucleate boiling and transition boiling heat transfer between the liquid film and the chamber wall were considered. The calculation results showed good agreement with the test data in both the steady-state and pulse operation although the limited test results were used for comparison. Recently, Fu et al. [54] conducted a CFD analysis of a bipropellant rocket engine with a droplet/wall impact model incorporating five impacting and formation processes of droplets and films. The five modes (1) stick/spread, (2) boiling with breakup, (3) suspend, (4) rebound, and (5) splash, depending on the conditions of the droplet Weber number and wall surface temperature. The calculation result with the new model was compared to that with a spray/wall interaction model by O'Rourke and Amsden [55] and showed better agreement with the experiment data of the temperature distribution of the chamber wall due to the formation of smaller droplets and thinner liquid film resulted from boiling phenomena. These results suggest that a deeper understanding of the liquid formation processes including boiling phenomena is required to reveal the whole aspect of the liquid film from inception to dry-out.

So far, the physical phenomena in bipropellant thrusters have been introduced with examples of the previous research. While there have been a relatively large number of studies on impinging atomization and combustion of hypergolic propellants, studies on liquid film cooling are limited and a deep understanding of it is a long way as pointed out in a recent review of the film cooling by Shine and Nidhi [56]. Especially for the interaction between the liquid film and the chamber wall has not been considered in depth. Actually, for the film cooling model in the CFD analysis of bipropellant thrusters, the liquid film on the wall is reproduced by distributing the small droplets on the wall and the heat transfer coefficient of the liquid film is arbitrarily tuned [18, 42]. Therefore, the present thesis focuses on the formation processes of the liquid film formed through the

liquid jet impingement onto the wall, in both conditions of non-heat-input from the wall and heat-input with boiling phenomena, for a deeper understanding of the liquid film cooling.

1.4 Previous research on formation processes of liquid film

The actual operation patterns of bipropellant thrusters are described, and the circumstances under which the liquid films are formed are summarized. Figure 1.3 shows the schematic illustration of the operation patterns of bipropellant thrusters. The liquid jets are injected mainly against two wall conditions to form liquid films. One is the cold wall surface of its temperature below the saturation temperature of the liquid fuel. This situation is observed at the start of steady-state mode (rated combustion) as shown in Fig. 1.3. The other is the hot wall surface with a spatial temperature gradient along the axial direction. The surface temperature exceeds the saturation temperature or the Leidenfrost temperature of the liquid fuel. The circumstance can be observed in pulse firing mode. During the steady state of the rated combustion operation, the highest wall temperature appears around the throat part, and a large temperature gradient is formed from the throat to the injector side [18, 57]. After the injection of the propellant is cut off, the stored heat around the throat is transferred towards the injector side due to the solid heat conduction inside the chamber wall. This is known as heat soak-back [58]. If the interval between each firing pulse is too short to allow for sufficient cooling of the chamber wall, the fuel for film cooling is injected onto the hot wall with a spatial temperature gradient.

As discussed above, the liquid films are formed against two conditions of the wall temperature. Therefore, the formation processes of the liquid film by the jet impingement on both cold and hot surfaces are the target of the present thesis. In the following, the previous studies on the liquid film on cold and hot surfaces are described.

1.4.1 Liquid film formed by liquid jet impingement on cold wall

Liquid jet impingement on the solid wall with the formation of a liquid film is a physical phenomenon frequently seen both in our daily life and in many industrial fields. In terms of engineering application, the distribution of the liquid film (film shape, thickness, velocity, and so on) is an important factor. Therefore, many studies have been conducted to theoretically predict the distribution of the liquid film, as well as to

experimentally investigate the effects of physical parameters on it. An early theoretical model is Watson's model [59]. Watson predicted the liquid film distribution formed by a laminar or turbulent jet impinging vertically onto the solid wall from the similarity solution of the laminar boundary layer equation. Ishigai et al. [60] conducted a theoretical analysis of the liquid film through vertical water jet impingement with the integral method by approximating the velocity distribution across the laminar boundary layer with the quartic equation. They also measured the liquid film thickness by the needle contact method and compared the theoretical models of them and Watson with the measurement results; the model by Ishigai et al. showed good agreement while that of Watson underpredicted the thickness in the downstream region of radial flow. Morison and Thorpe [61] experimentally investigated the wetting of two different surfaces (acrylic and stainless steel) by a liquid jet of water and aqueous solutions (1 wt% NaOH or 0.5 wt% dish-washing detergent) in connection with applications of cleaning. Wilson et al. [62] developed a model of the liquid film shape, considering the effects of the mass flow rate, viscosity, surface tension, contact angle, density, and gravity. This model could be used to predict the wetted width and radius of a hydraulic jump, which occurs when the momentum of the radially outward flow is balanced by surface tension, and the results were noted to be in good agreement with the experimental data reported by Morison and Thorpe [61] and obtained by themselves. Recently, Bhagat et al. [63] experimentally and theoretically indicated that gravity had no important effect on determining the radial position of a hydraulic jump; it was governed by the condition that the momentum in the liquid film was balanced with the viscosity force and surface tension.

The above studies focused on the film formed by a single jet vertically impinging on a solid surface. Inamura et al. [64] theoretically analyzed the distribution of the liquid film formed by an oblique jet impingement onto the wall with the integral method the same as Ishigai et al. [60]. Their model did not include the effect of the surface tension of the liquid. The theoretical model was compared with the measurement results of the liquid film thickness with the needle contact method taken by themselves; the model agreed well with the experimental data except for the periphery of the liquid film where the surface tension was predominant. Good and Nollet [65] experimentally investigated the effects of flow rate and impingement angle on the liquid film width and observed a linear relationship between the liquid jet velocity and the maximum film width. Wang et al. [66] experimentally investigated the liquid film shape by an oblique jet impingement under the various conditions of nozzle diameter of 2 − 4 mm, impingement angle of 45° − 135°, and mass flow rate of 7 − 133 g/s. In their results, the three flow patterns were observed depending on flow rate, impingement angle, and contact angle whereas the

effect of contact angle diminished at a higher flow rate. They also modified the theoretical model of Wilson et al. [62] so that it could be applied to an oblique impingement jet by incorporating the model of the flow distribution in the jet impingement zone, which originated from Hasson and Peck's jet-jet impingement model [67] and was implemented to the situation of an oblique jet impingement onto the solid wall by Kate et al. [68]. Although their model reasonably predicted the liquid film shape and the effects of physical parameters, further improvements to the theoretical model are still being made with dedication by Wilson's group as seen in [69, 70].

As introduced above, the effects of geometry and physical parameters on the liquid film distribution on the cold wall have been investigated in detail. However, the studies on the liquid film formed through a jet obliquely impinging onto the wall are still relatively few compared to the studies on gas jets or on the vertical impingement of a liquid jet [70]. Especially, the liquid film distribution under the conditions of quite low flow rate (< 7.0 g/s), small nozzle diameter (< 2 mm), and small impingement angle (< 25°), which range in the design conditions of actual bipropellant thrusters, have rarely been investigated [65]. Therefore, the formation processes of the liquid film under such conditions should be explored.

1.4.2 Formation processes and heat transfer characteristics of liquid film on hot surface

In cooling processes demanding high heat dissipation, jet impingement cooling, as a liquid film, is one of the most effective techniques owing to the high heat removal rate by the latent heat through a phase change from liquid to vapor [71]. Therefore, the cooling method is widely employed also in material processes and the cooling of nuclear reactor cores, and numerous investigations have been devoted to the heat transfer characteristic between the hot surface and the liquid film formed through especially a vertical jet impingement.

When the liquid jet is injected onto a hot surface whose temperature exceeds the saturated temperature or the Leidenfrost temperature of the liquid (superheated surface), most of the liquid is deflected away from the leading edge of the liquid film because of the vapor flow induced by vigorous boiling. The boundary between the wetted region and the dry region is called as the wetting front (WF) [72, 73, 74]. During the cooling processes, different cooling modes, such as single-phase forced convection, nucleate boiling, transition boiling, and film boiling coexist, which makes it difficult to understand

the cooling processes [75]. The position of the maximum heat flux, essential for understanding the quenching phenomena, was located within the wetted region rather than at the WF [74]. The WF moves downstream with the passage of time, and the velocity of the WF and the value of the maximum heat flux decrease with the radial position of the WF [72, 73].

For the WF propagation, Yamanouchi [76] proposed a one-dimensional model to predict the velocity of the WF. The model considered the distribution of the temperature and heat transfer coefficient only in the flow direction of the liquid film and postulated the value of the Leidenfrost temperature and the spatial distribution of the heat transfer coefficient as two-region partitioning of the wetted and dry region. Subsequently, a lot of models have been developed that use the partitioning model with various kinds of distributions of the heat transfer coefficient, which were summarized in the review paper of the analytical models for the prediction of the WF velocity [77]. However, the previous models postulated the value and distribution of the heat transfer coefficient due to the lack of experimental data. Recently, Okawa et al. [78] and Umehara et al. [79] derived the distribution of the heat transfer coefficient from measured wall temperature by a high-speed infra-red camera and applied the distribution to the calculation of the WF velocity. Although these models approximated a quasi-steady state leading to the constant value of the WF velocity in the flow direction, the velocity of the WF decreased further downstream [80, 81] because the temperature and the heat transfer coefficient varied with time at any location during the transient cooling such as the jet impingement cooling. The position of WF has often been correlated with the power function of the elapsed time, as shown in Eq. (1.3) [72, 74, 82-84].

$$x_{\text{wf}} = a \cdot t^n, \qquad (1.3)$$

where x_{wf} is the distance from the impingement point of the liquid jet to the position of the WF. Hatta et al. [82] conducted cooling tests of stainless steel plate with a temperature of 900°C under the conditions of a flow rate of 0.1 − 7.0 L/min and nozzle diameter of 10 mm. They observed that the WF radius increased in proportion to the square root of time (i.e., n = 0.5). Mitsutake and Monde [72] investigated the effects of the liquid jet velocity (5, 10, and 15 m/s), liquid subcooling (20, 50, and 80 K), and thermal properties of the test blocks (copper, brass, and carbon steel) on the constant a and exponent n. The constant a increased linearly with liquid jet velocity and liquid subcooling and assumed a higher value for a smaller value of the thermal inertia of the test blocks. The exponent n was observed to be independent of the liquid jet velocity and the thermal

property of the block, and weakly affected by the liquid subcooling. The tendency of the WF denoted as Eq. (1.3) was observed both in the plate with the lab-scale size [83] and in that with the industrial scale size [84]. The value of the exponent n ranged in roughly $0.3 - 0.6$ while that of the constant a took various values depending on conditions in the precious studies. Karwa et al. [74] remarked that there were two possible reasons for the decrease of the WF velocity. One of the reasons was the deceleration of the liquid film that relates to its ability to detach the bubbles from the surface. The other reason was that the liquid was more superheated as the distance traveled by the liquid increases with the expanding WF position, leading to a reduction in the ability to condense the bubbles at the WF.

The heat transfer characteristics in the wetted region, which are of critical importance to the WF behavior and the cooling processes, have also been examined in previous studies. The maximum heat flux, which appeared in the vicinity of the WF and separated the nucleate boiling region and the transition boiling region, is of particular interest, and several parameters affecting the boiling phenomena have been investigated. Mozumder et al. [85] extensively investigated the effects of jet velocity (3, 5, 10, and 15 m/s), degree of subcooling (5, 20, 50, and 80 K), metal properties (copper, brass, and carbon steel), and initial metal temperature (250, 300, 350, and 400°C) on the maximum heat flux. They found that the jet velocity and material properties of the metal had significant effects on the maximum heat flux, while the effects of the degree of subcooling and initial metal temperature were moderate and weak, respectively. Additionally, they proposed the correlation for predicting the maximum heat flux, which included these physical parameters, based on the correlation of the critical heat flux for the steady-state jet impingement cooling developed by Monde et al. [86]. The correlation could accurately predict the maximum heat flux except for the carbon steel case. Butterfield et al. [87] evaluated the effect of the wettability on the water jet impingement cooling by using hydrophilic, hydrophobic, and superhydrophobic surfaces with contact angles of 55°, 120°, and 150° respectively. Results showed that the lowest value of the maximum heat flux was always achieved on the superhydrophobic surface, although they evaluated not the local heat flux value but the value averaged over the radial region. Gomez et al. [88] examined the effect of the surface roughness by employing two types of surface finishing approaches which resulted in the average value of each surface roughness of 0.3 μm and 5 μm. From the results, they concluded that the rougher surface led to the earlier wetting of the liquid film, resulting in the achievement of the higher heat flux while the value of the heat flux in the film boiling regime showed no difference. Lee et al. conducted the cooling tests by single [89], two [90], and seven hexagonally arranged [91] water jets and

13

evaluated the effect of liquid film interference on heat transfer characteristics.

The successive investigations have improved the comprehension of the jet impingement cooling. Nevertheless, the physical dynamics of the WF (i.e., the mechanism of the liquid film splashing, the heat flow inducing the vigorous bubble expansion, and the dominant factors for them) has not still been elucidated [83, 92, 93]. In addition, many previous studies focused on the vertical jet impingement and relatively high flow rate conditions ($\sim O(1\text{-}100)$ L/min) because a large amount of water is used in material processes and cooling of nuclear reactor cores. Results for the film formation processes under the conditions of very low flow rate and small impingement angle as seen in bipropellant thrusters have not been well reported, as mentioned in Section 1.4.1.

1.5 Objectives and framework of this thesis

The performance of bipropellant thrusters must be further improved for the high-accuracy operation of next-generation small spacecraft and satellites. In bipropellant thrusters, liquid fuel jets are obliquely injected from the small nozzle holes onto the chamber wall with a low flow rate and shallow angle to form liquid films and protect the chamber wall from the high-temperature combustion gases. To achieve a better performance of the thrusters under the trade-off relationship between the thrust and cooling performances, the reduction and optimization of the fuel flow rate for the liquid film cooling are required. In the design and development processes of the thrusters, however, the optimization strongly relies on the time- and money-consuming combustion tests. Additionally, the operational range of the thrusters needs to be expanded for enabling the various operation patterns of the small-scale spacecraft, but it is restricted due to the heat resistance of the thrusters. These current situations are due to the lack of understanding of the fundamental physics of liquid film cooling phenomena. Therefore, the present thesis focuses on the formation processes of the liquid film formed by an oblique liquid jet impingement onto the wall. The objective of this study is to extract the physical factors that determine liquid film formation and to clarify the relationship between the factors and the phenomenon. The contents of each chapter in the present thesis are listed below.

Chapter 2 focused on the liquid film distribution on a cold wall, considering that liquid jets are injected onto the wall surface below the saturated temperature of the liquid at the start of the steady-state firing operation of the thrusters. A liquid film formed by a liquid jet obliquely impinging onto the metal plate at the steady state was taken by a still camera.

The effects of various injection parameters such as liquid flow rate, nozzle diameter, impingement angle, and the liquid jet length on the liquid film shape were comprehensively evaluated in the experiments. From the experimental results, the important physical parameters for the liquid film shape were extracted, and then, the theoretical model for predicting the maximum film width, which is one of the important length scales for representing the liquid film distribution, was developed.

Chapter 3 focused on the liquid film behavior and heat transfer characteristics on a superheated surface. The quenching of a heated metal plate with a spatial temperature gradient by a liquid jet impingement was experimentally investigated, assuming the situation that fuel liquid jets are possible to be injected onto a hot surface due to the heat soak-back. The liquid film behavior and the temperature distribution of the metal plate were simultaneously measured by using a high-speed camera and an infra-red camera, respectively. In the experiment, the effects of liquid flow rate and liquid jet velocity on the formation processes of the liquid film were evaluated by varying the nozzle diameter and liquid flow rate.

Chapter 4 focused on the transient cooling of a superheated surface by an intermittent injection of a liquid jet to enrich the understanding of the liquid film behavior during the pulse operation. The liquid flow rate was found to be the dominant parameter to the formation processes of the liquid film in chapter 3. Additionally, in chapter 3, the numerical scheme for solving the inverse problem of the transient three-dimensional heat conduction was developed. Therefore, in chapter 4, the pulsed cooling tests with the same usage of the liquid but with different liquid flow rates and duty cycle (the injection duration to one period) were conducted, and the measurement and analysis methods developed in chapter 3 were applied to evaluate the heat transfer characteristics of the liquid film during the pulsed cooling. In addition, the effects of the thermal properties of the metal plate on the cooling performance were investigated by employing two types of metal plates because the heat transfer characteristics of the liquid film and the temperature change of the metal plate were affected by the thermal properties of the metal plate.

Chapter 5 focused on the atomization processes that appeared in the liquid film on a superheated surface because dispersed droplets from the liquid film produced through the boiling phenomena are considered to possibly reduce the flow rate of the liquid film for cooling. The sequential events of the boiling induced atomization which appeared in the liquid film were visualized through magnified high-speed imaging with the backlight

technique. From the visualization images, experimental findings such as bubble radius, droplet diameter, and velocity of droplet were obtained, and then, the theoretical model for the size of the dispersed droplet was developed. Finally, the amount of dispersed droplets were estimated by using the measurement results.

In chapter 6, the findings obtained in this study were summarized, and the remaining issues and the recommendations for future work on the topic were discussed.

References

[1]   https://www.morganstanley.com/ideas/investing-in-space

[2]   M. Yoshikawa, J. Kawaguchi, A. Fujiwara, and A. Tsuchiyama, "Hayabusa sample return mission," in *Asteroids IV*, pp. 397-418, 2015.

[3]   M. Hirabayashi and Y. Tsuda, "Hayabusa2 Asteroid Sample Return Mission: Technological Innovation and Advances," *Elsevier*, 2022.

[4]   Y. Mihara, H. Ashida, and O. Kitayama, "The Latest Development Status of H3," *Proceedings of the International Astronautical Congress, IAC*, vol. D2, 2021.

[5]   T. Yoshimitsu, S. Sawai, T. Mizuno, S. Fukuda, N. Bando, S. Sakai, K. Higuchi, T. Okada, T. Kubota, and D. Kobayashi, "Proposal of smart lander for investigating moon," *Proceedings of the International Astronautical Congress, IAC*, vol. 2, pp. 1096-1100, 2009.

[6]   K. Kuramoto, Y. Kawakatsu, M. Fujimoto, A. Araya, M. A. Barucci, H. Genda, N. Hirata, H. Ikeda, T. Imamura, J. Helbert, S. Kameda, M. Kobayashi, H. Kusano, D. J. Lawrence, K. Matsumoto, P. Michel, H. Miyamoto, T. Morota, H.Nakagawa, T. Nakamura, K. Ogawa, H. Otake, M. Ozaki, S. Russell, S. Sasaki, H. Sawada, H. Senshu, S. Tachibana, N. Terada, S. Ulamec, T. Usui, K. Wada, S. Watanabe, and S. Yokota, "Martian moons exploration MMX: sample return mission to Phobos elucidating formation processes of habitable planets," *Earth, Planets and Space*, vol. 74, Article 12, 2022.

[7]   G. P. Sutton and O. Biblarz, "Rocket propulsion elements 9ᵗʰ Edition," *John Wiley & Sons*, 2016.

[8]   I. Kimura, "rocket kougaku," *Yokendo*, 1993 (in Japanese).

[9]   Y. Oishi, S. Tauchi, and C. Inoue, "Unsteady stream-tube model for pulse performance of bipropellant thrusters," *Journal of Propulsion and Power*, Article in Advance, 2022.

[10]   S. Nakai, T. Shiiki, M. Yamamoto, H. Okudera, and S. Ishizaki, "Development

status of HTV (H-II Transfer Vehicle) propulsion system," *IHI ENGINEERING REVIEW*, vol. 49, no. 3. pp. 143-149, 2009 (in Japanese).

[11] A. Noumi, R. Ujiie, S. Ueda, K. Someya, N. Ishihama, and Y. Kondoh, "Verification of HTV-X resilient design by simulation environment with model-based technology," *AIAA Modeling and Simulation Technologies Conference*, AIAA-2018-1926, 2018.

[12] H. Shimoji and T. Inoue, "Spacecrafts to Moon and Mars satellite," *Mitsubishi Electric technical report*, vol. 95, no. 2, pp. 113-116, 2021 (in Japanese).

[13] H. Tani, Y. Daimon, M. Sasaki, and Y. Matsuura, "Atomization and hypergolic reactions of impinging streams of monomethylhydrazine and dinitrogen tetroxide," *Combustion and Flame*, vol. 185, pp. 142–151, 2017.

[14] W. T. Webber and R. J. Hoffman, "Mechanistic model for analysis of pulse-mode engine operation," *Journal of Spacecraft and Rockets*, vol. 12, no. 2, pp. 113-117, 1975.

[15] S. Iihara, H. Miyajima, and R. Nagashima, "Hydrazine/NTO liquid apogee engine for the ETS-VI," *23rd AIAA/SAE/ASME/ASEE Joint Propulsion Conference*, AIAA-87-1936, 1987.

[16] Y. Matsuura, S. Iihara, and Y. Tashiro, "Hypergolic propellant ignition phenomenon associated with two-phase oxidizer flow injection," *Journal of Propulsion and Power*, vol. 30, no. 5, pp. 1399-1409, 2014.

[17] S. M. Davis and N. Yilmaz, "Advances in hypergolic propellants: Ignition, hydrazine, and hydrogen peroxide research," *Advances in Aerospace Engineering*, vol. 2014, pp. 1-9, 2014.

[18] Y. Daimon, H. Negishi, H. Tani, Y. Matsuura, S. Iihara, and S. Takata, "Flow field and heat transfer analysis in a MON/MMH bipropellant rocket engine," *International Journal of Energetic Materials and Chemical Propulsion*, vol. 16, no. 3, pp. 263-280, 2017.

[19] A. H. Lefebvre and V. G. McDonell, "Atomization and sprays 2nd Edition," *CRC Press*, 2017.

[20] ILASS-Japan, "Atomization technology," *Morikita Publishing Co., Ltd.*, 2001 (in Japanese).

[21] H. M. Ryan, W. E. Anderson, S. Pal, and R. J. Santoro, "Atomization characteristics of impinging liquid jets," *Journal of Propulsion and Power*, vol. 11, no. 1, pp. 135-145, 1995.

[22] C. Inoue, T. Watanabe, and T. Himeno, "Liquid sheet dynamics and primary breakup characteristics at impingement type injector," *45th*

AIAA/SAE/ASME/ASEE Joint Propulsion Conference, AIAA-2009-5041, 2009.

[23] T. Himeno, T. Watanabe, and A. Konno, "Numerical analysis for propellant management in rocket tanks," *Journal of Propulsion and Power*, vol. 21, no. 1, pp. 76-86, 2005.

[24] P. A. Strakey and D. G. Talley, "Spray characteristics of impinging jet injectors at high back-pressure," *8th International Conference on Liquid Atomization and Sprays Systems ICLASS*, 2000.

[25] S. Karikawa, J. Hayashi, Y. Daimon, H. Negishi, and F. Akamatsu, "Disintegration Degree of Liquid Fan Formed with Impingement of Two Liquid Jets," *Proceedings of 16th Annual Conference on ILASS-Asia*, 2013.

[26] C. Inoue, J. Kouwa, T. Watanabe, T. Himeno, S. Uzawa, and S. Matsuno, "Normalized spray flux distribution in impinging atomization," *Transactions of the Japan Society for Aeronautical and Space Sciences, Aerospace Technology Japan*, vol. 60, no. 4, pp. 255-258, 2017.

[27] C. Inoue, Y. Takeuchi, K. Nozaki, T, Himeno, T. Watanabe, G. Fujii, and Y. Daimon, "Unified length scale of spray structure by unlike impinging jets," *Transactions of the Japan Society for Aeronautical and Space Sciences, Aerospace Technology Japan*, vol. 62, no. 4, pp. 213-218, 2019.

[28] H. Tani, "Chemical kinetic mechanism, auto-ignition and flame dynamics of hypergolic propellant," *Nagare*, vol. 34, pp. 25-32, 2015 (in Japanese).

[29] F. Sawyer and I. R. Glassman, "Gas-phase reaction of hydrazine with nitrogen dioxide, nitric oxide, and oxygen," *Proceedings of the Combustion Institute*, vol. 11, issue 1, pp. 861-869, 1967.

[30] K. Ohminami, S. Sawai, K. Uesugi, N. Yamanishi, and M. Koshi, "Hydrazine and di-nitrogen tetroxide combustion model inside film-cooled bipropellant thruster," *45th AIAA/SAE/ASME/ASEE Joint Propulsion Conference*, AIAA-2009-5044, 2009.

[31] Y. Daimon, H. Terashima, and M. Koshi, "Chemical kinetics of hypergolic ignition in N_2H_4/ N_2O_4-NO_2 gas mixstures," *Journal of Propulsion and Power*, vol. 30, no. 3, pp. 707-716, 2014.

[32] N. Kanno, H. Terashima, Y. Daimon, N. Yoshikawa, and M. Koshi, "Theoretical study of the rate coefficients for CH_3NHNH_2 + NO_2 and related reactions," *International Journal of Chemical Kinetics*, vol. 46, issue. 8, pp. 489-499, 2014.

[33] N. Kanno, H. Tani, Y. Daimon, H. Terashima, N. Yoshikawa, and M. Koshi, "Hypergolic ignition mechanism of Monomethylhydrazine/nitrogentetroxide bipropellant," *Proceedings of 52nd Combustion Symposium*, pp. 124-125, 2014 (in

Japanese).

[34] B. R. Lawve, "Some observations on the combustion of N_2H_4 Droplets," *AIAA Journal*, vol. 4, no. 4, pp. 659-662, 1966.

[35] W. Daimon, M. Tanaka, and I. Kimura, "The mechanisms of explosions induced by contact of hypergolic liquid propellants, hydrazine and nitrogen tetroxide," *Proceedings of the Combustion Institute*, vol. 20, issue 1, pp. 2065-2071, 1984.

[36] J. Hayashi et al., "Multilayer reaction zones of a counterflow flame of gaseous Nitrogen Tetroxide and a liquid Monomethylhydrazine pool," *Combustion and Flame*, vol. 201, pp. 244-251, 2019.

[37] H. Tani, H. Terashima, M. Koshi and Y. Daimon, "Hypergolic ignition and flame structures of hydrazine/nitrogen tetroxide co-flowing plane jets," *Proceedings of the Combustion Institute*, vol. 35, pp. 2199-2206, 2015.

[38] Y. Daimon, H. Tani, H. Terashima, and M. Koshi, "Three-dimensional structures in hypergolic ignition process and flame-holding mechanisms for hydrazine/nitrogen dioxide un-like doublet impinging gas jets," *54th AIAA Aerospace Sciences Meeting*, AIAA-2016-0691, 2016.

[39] K. Suzuki, "Rocket engine," *Morikita Publishing Co., Ltd.*, 2004 (in Japanese).

[40] C. D. Coulbert, "Selecting cooling techniques for liquid rockets for spacecraft," *Journal of Spacecraft and Rockets*, vol. 1, no. 2, pp. 129-139, 1964.

[41] R. P. Miller and E. G. Coy, "Studies in optimizing the film flow rate for liquid film cooling," *47th AIAA/SAE/ASME/ASEE Joint Propulsion Conference*, AIAA-2011-5779, 2011.

[42] H. Tani, "Research direction for modeling the liquid film cooling in the combustion analysis of bipropellant chemical thrusters," *Private communication*.

[43] R. H. Borden and Y. Mich, "Heat transfer in rocket motors and the application of film and sweat cooling," *Transactions of the American Society of Mechanical Engineers*, vol. 73, issue 4, pp. 385-390, 1951.

[44] G. Morrell, "Investigation of internal film cooling of 1000 pound thrust liquid ammonia-liquid oxygen rocket engine combustion chamber," *Technical Report NACA-RM-E51E04*, 1951.

[45] A. E. Abramso, "Investigation of internal film cooling of exhaust nozzle of a 1000 pound thrust liquid ammonia-liquid oxygen rocket," *Technical Report NACA-RM-E52C26*, 1952.

[46] C. Inoue, G. Fujii, and Y. Daimon, "Mixing length scale of bi-propellant thrusters for characteristic velocity formulation," *International Journal of Energetic Materials and Chemical Propulsion*, vol. 16, no. 3, pp. 281-294, 2017.

[47] T. Inoue, C. Inoue, G. Fujii, and Y. Daimon, "Evaporation of Three-Dimensional Wavy Liquid Film Entrained by Turbulent Gas Flow," *AIAA Journal*, vol. 60, no. 6, pp. 3805-3812, 2022.

[48] R. C. Stechman, J. Oberstone, and J. C. Howel "Design criteria for film cooling for small liquid-propellant rocket engines," *Journal of Spacecraft and Rockets*, vol. 6, no. 2, pp. 97-102, 1969.

[49] S. R. Shine and S. S. Kumar, and S.S. Suresh "A new generalised model for liquid film cooling in rocket combustion chambers," *International Journal of Heat and Mass Transfer*, vol. 55, pp. 5065–5075, 2012.

[50] G. R. Kinney, A. E. Abramson, and J. L. Sloop, "Internal-liquid-film-cooling experiments with air-stream temperatures to 2000°F in 2- and 4-inch-diameter horizontal tube," *NACA TR 1087*, 1952.

[51] A. V. Cherdantsev, D. B. Hann, and B. J. Azzopardi, "Study of gas-sheared liquid film in horizontal rectangular duct using high-speed LIF technique: Three-dimensional wavy structure and its relation to liquid entrainment," *International Journal of Multiphase Flow*, vol. 67, pp. 52-64, 2014.

[52] W. M. Grisson, "Liquid film cooling in rocket engines," *Technical Report AEDC-TR-91-1,* DTIC, 1991.

[53] G. P. Prohit, P. A. Donatelli, and J. R. Ellison, "Transient thermal model of a film-cooled bipropellant thruster," *38th AIAA Aerospace Sciences Meeting*, AIAA-2000-1072, 2000.

[54] P. Fu, L. Hou, Z. Ren, Z. Zhang, X. Mao, and Y. Yu, "A droplet/wall impact model and simulation of a bipropellant rocket engine," *Aerospace Science and Technology*, vol. 88, pp. 32–39, 2019.

[55] P. O'Rourke and A. Amsden, "A spray/wall interaction submodel for the KIVA-3 wall film model," *SAE Technical Paper*, 2000.

[56] S. R. Shine and S. S. Nidhi, "Review on film cooling of liquid rocket engines," *Propulsion and Power Research*, vol. 7, no. 1, pp. 1–18, 2018.

[57] G. Fujii, Y. Daimon, K. Furukawa, C. Inoue, D. Shiraiwa, and N. Tanaka, "Visualization of Coolant Liquid Film Dynamics in Hypergolic Bipropellant Thruster," *Journal of Propulsion and Power*, vol. 38, no. 2, pp. 267-273, 2022.

[58] S. Takata, Y. Daimon, K. Sugimori, N. Matsuda, and Y. Tashiro, "Design verification results of japanese 120N Bi-propellant thrusters (HBT-1) based on its first flight in HTV3," *49th AIAA/ASME/SAE/ASEE Joint Propulsion Conference*, AIAA-2013-3754, 2013.

[59] E. J. Watson, "The radial spread of a liquid jet over a horizontal plate," *Journal of*

Fluid Mechanics, vol. 20, part 3, pp. 481-499, 1964.

[60] S. Ishigai, S. Nakanishi, M. Mizuno, and T. Imamura, "Heat transfer of the impinging round water jet in the interference zone of film flow along the wall," *Transactions of the JSME (in Japanese)*, vol. 42, no. 357, pp. 1502-1510, 1976.

[61] K. R. Morison and R. J. Thorpe, "Liquid distribution from cleaning-in-place sprayballs," *Food and Bioproducts Processing*, vol. 80, issue 4, pp. 270-275, 2002.

[62] D. I. Wilson, B. L. Le, H. D. A. Dao, K. Y. Lai, K. R. Morison, and J. F. Davidson, "Surface flow and drainage films created by horizontal impinging liquid jets," *Chemical Engineering Science*, vol. 68, pp. 449-460, 2012.

[63] R. K. Bhagat, N. K. Jha, P. F. Linden, and D. I. Wilson, "On the origin of the circular hydraulic jump in a thin liquid film," *Journal of Fluid Mechanics*, vol. 851, p. R5, 2018.

[64] T. Inamura, H. Yanaoka, and T. Tomoda, "Prediction of Mean Droplet Size of Sprays Issued from Wall Impingement Injector," *AIAA Journal*, vol. 42, no. 3, pp. 614–621, 2004.

[65] R. M. Good and W. K. Nollet, "Fluid film distribution investigation for liquid film cooling application," *53rd AIAA/ASME/SAE/ASEE Joint Propulsion Conference*, AIAA-2017-4920, 2017.

[66] T. Wang, D. Faria, L. J. Stevens, J. S. C. Tan, J. F. Davidson, and D. I. Wilson, "Flow patterns and draining films created by horizontal and inclined coherent water jets impinging on vertical walls," *Chemical Engineering Science*, vol. 102, pp. 585-601, 2013.

[67] D. Hasson, R. E. Peck, "Thickness distribution in a sheet formed by impinging jets," *AIChE Journal*, vol. 10, no. 5, pp. 752-754, 1964.

[68] R. P. Kate, P. K. Das, and S. Chakraborty, "Hydraulic jumps due to oblique impingement of circular liquid jets on a flat horizontal plate," *Journal of Fluid Mechanics*, vol. 573, pp. 247-263, 2007.

[69] R. K. Bhagat and D. I. Wilson, "Flow in the thin film created by a coherent turbulent water jet impinging on a vertical wall," *Chemical Engineering Science*, vol. 152, pp. 606-623, 2016.

[70] M. W. L. Chee, P. Chauhan, J. Georgiou, and D. I. Wilson, "Flow distribution in the liquid film created by a coherent circular water jet impinging obliquely on a plane wall," *Experimental Thermal and Fluid Science*, vol. 140, Article 110748, 2023.

[71] M. T. Meyer, I. Mudawar, C. E. Boyack, and C. A. Hale, "Single-phase and two-phase cooling with an array of rectangular jets," *International Journal of Heat and*

Mass Transfer, vol. 49, pp. 17-29, 2006.

[72] Y. Mitsutake and M. Monde, "Heat transfer during transient cooling of high temperature surface with an impinging jet," *Heat and Mass Transfer/Waerme- und Stoffuebertragung*, vol. 37, no. 4–5, pp. 321–328, 2001.

[73] N. Karwa, T. Gambaryan-Roisman, P. Stephan, and C. Tropea, "Experimental investigation of circular free-surface jet impingement quenching: Transient hydrodynamics and heat transfer," *Experimental Thermal and Fluid Science*, vol. 35, no. 7, pp. 1435-1443, 2011.

[74] N. Karwa and P. Stephan, "Experimental investigation of free-surface jet impingement quenching process," *International Journal of Heat and Mass Transfer*, vol. 64, pp. 1118-1126, 2013.

[75] M. Monde, "Heat Transfer Characteristics during Quench of High Temperature Solid," *Journal of Thermal Science and Technology*, vol. 3, no. 2, pp. 292-308, 2008.

[76] A. Yamanouchi, "Effect of core spray cooling in transient state after loss of coolant accident," *Journal of Nuclear Science and Technology*, vol. 5, no. 11, pp. 547-558, 1968.

[77] S. K. Sahu, P. K. Das, and S. Bhattacharyya, "Analytical and semi-analytical models of conduction controlled rewetting," *Thermal Science*, vol. 19, no. 5, pp. 1479-1496, 2015.

[78] T. Okawa, K. Yamagata, and Y. Umehara, "Measurement of heat transfer coefficient profile during quenching of a vertical hot wall with a falling liquid film," *Nuclear Engineering and Design*, vol. 363, Article 110629, 2020.

[79] Y. Umehara, K. Yamagata, and T. Okawa, 'Spatial distribution of heat transfer coefficient in the vicinity of wetting front during falling liquid film cooling of a vertical hot wall', *International Journal of Heat and Mass Transfer*, vol. 185, Article 122422, 2022.

[80] C. Agrawal, R. Kumar, A. Gupta, and B. Chatterjee, 'Rewetting and maximum surface heat flux during quenching of hot surface by round water jet impingement', *International Journal of Heat and Mass Transfer*, vol. 55, pp. 4772-4782, 2012.

[81] B. Wang, D. Lin, Q. Xie, Z. Wang, and G. Wang, "Heat transfer characteristics during jet impingement on a high-temperature plate surface," *Applied Thermal Engineering*, vol. 100, pp. 902-910, 2016.

[82] N. Hatta, J. Kokado, K. Hanasaki, "Numerical Analysis of Cooling Characteristics for Water Bar," *Transactions of the Iron and Steel Institute of Japan*, vol. 23, no. 7, pp. 555-564, 1983.

[83] Y. Liu, H. Nakai, Y. Mitsutake, and M. Monde, "Experimental study on transient boiling heat transfer around wetting front during subcooled jet impingement quenching," *Thermal Science and Engineering*, vol. 29, no. 1. pp. 9-17, 2021.

[84] A. V. S. Oliveira, D. Marechal, J. -L. Borean, V. Schick, J. Teixeira, S. Denis, and M. Gradeck, "Experimental study of the heat transfer of single-jet impingement cooling onto a large heated plate near industrial conditions," *International Journal of Heat and Mass Transfer*, vol. 184, Article 121998, 2022.

[85] A. K. Mozumder, M. Monde, P. L. Woodfield, and M. A. Islam, "Maximum heat flux in relation to quenching of a high temperature surface with liquid jet impingement," *International Journal of Heat and Mass Transfer*, vol. 49, pp. 2877-2888, 2008.

[86] M. Monde, K. Kitajima, T. Inoue, and Y. Mitsutake, "Critical heat flux in forced convective subcooled boiling with impinging jet (Effect of subcooling)," *Transactions of the JSME (in Japanese)*, vol. 60, no. 571, pp. 932-939, 1994.

[87] D. J. Butterfield, B. D. Iverson, D. Maynes, and J. Crockett, "Transient heat transfer of impinging jets on superheated wetting and non-wetting surfaces," *International Journal of Heat and Mass Transfer*, vol. 175, Article 121056, 2021.

[88] C. F. Gomez, C. W. M. van der Geld, J. G. M. Kuerten, M. Bsibsi, and B. P. M. van Esch, "Film boiling in quench cooling with high-temperature jets," *International Journal of Heat and Mass Transfer*, vol. 164, Article 120578, 2021.

[89] S. G. Lee, M. Kaviany, C. J. Kim, and J. Lee, "Quasi-steady front in quench subcooled-jet impingement boiling: Experiment and analysis," *International Journal of Heat and Mass Transfer*, vol. 113, pp. 622-634, 2017.

[90] S. G. Lee, M. Kaviany, and J. Lee, "Quench subcooled-jet impingement boiling: Two interacting-jet enhancement," *International Journal of Heat and Mass Transfer*, vol. 126, pp. 1302-1314, 2018.

[91] S. G. Lee, M. Kaviany, and J. Lee, "Quench subcooled-jet impingement boiling: Staggered-array jets enhancement," *International Journal of Heat and Mass Transfer*, vol. 136, pp. 888-898, 2019.

[92] A. H. Nobari, V. Prodanovic, and M. Militzer, 'Heat transfer of a stationary steel plate during water jet impingement cooling', *International Journal of Heat and Mass Transfer*, vol. 101, pp. 1138–1150, 2016.

[93] S. Waldeck, H. Woche, E. Specht, and U. Fritsching, "Evaluation of heat transfer in quenching processes with impinging liquid jets," *International Journal of Thermal Sciences*, vol. 134, pp. 160-167, 2018.
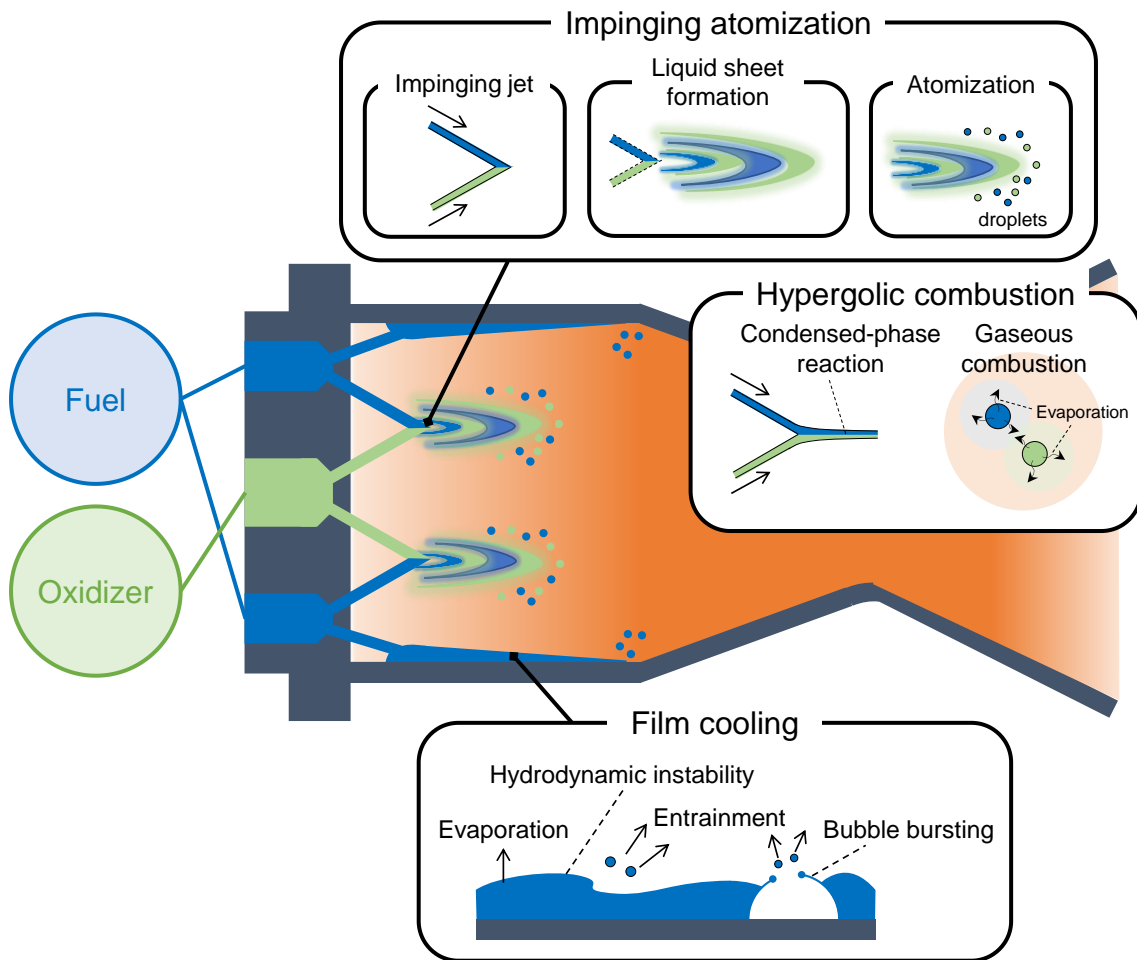
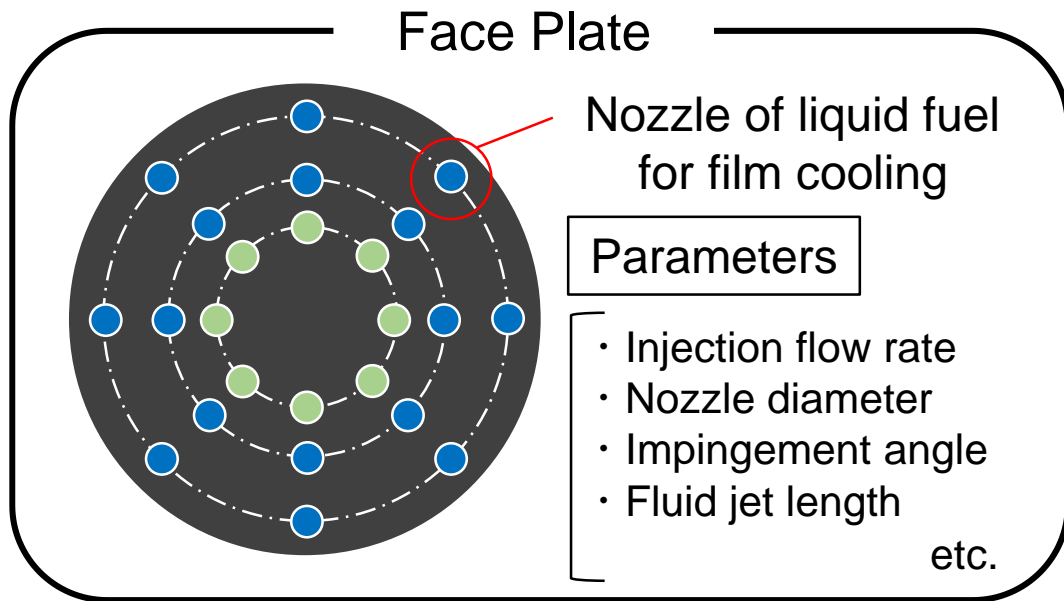Fig. 1.1 Key physical phenomena in bipropellant rocket thrust chamber

Face Plate

Nozzle of liquid fuel for film cooling
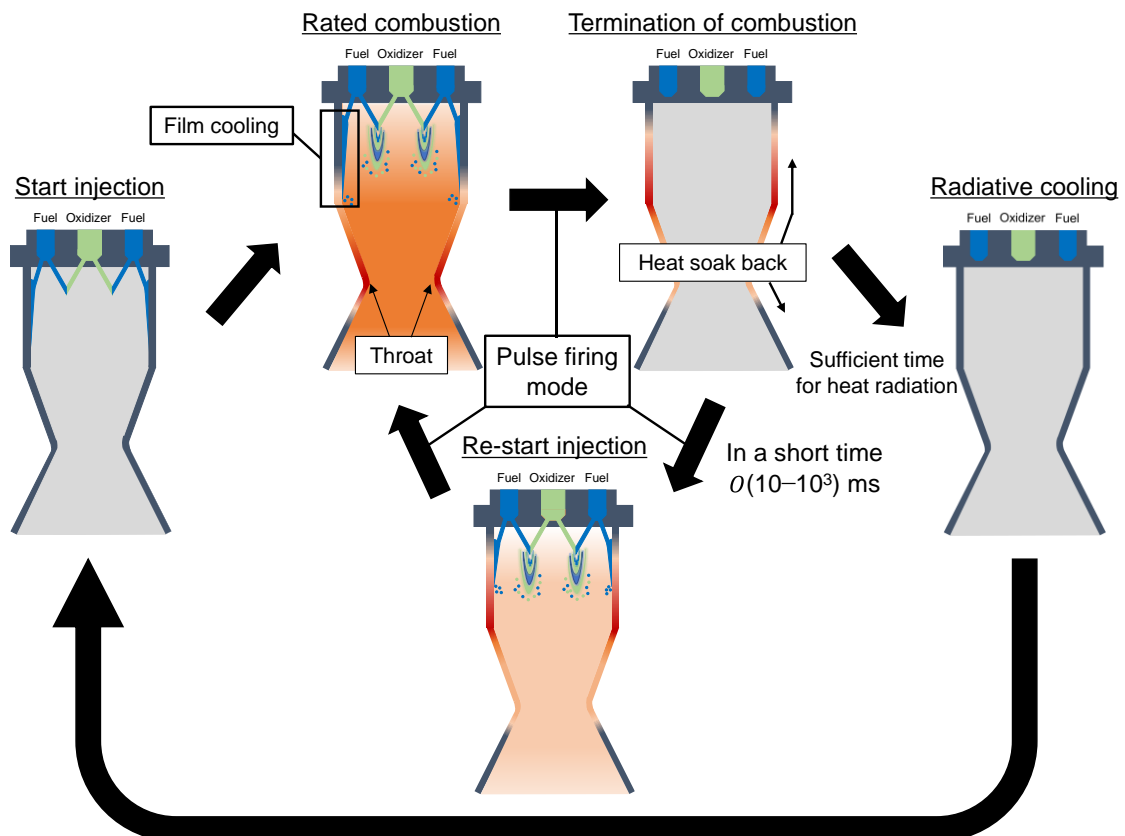
Parameters

· Injection flow rate
· Nozzle diameter
· Impingement angle
· Fluid jet length

etc.

Fig. 1.2 Schematic of injector face plate

Rated combustion

Fuel Oxidizer Fuel

Film cooling

Throat

Termination of combustion

Fuel Oxidizer Fuel

Heat soak back

Start injection

Fuel Oxidizer Fuel

Pulse firing mode

Radiative cooling

Fuel Oxidizer Fuel

Sufficient time for heat radiation

In a short time $O(10-10^3)$ ms

Re-start injection

Fuel Oxidizer Fuel

Fig. 1.3 Schematic of operation pattern of bipropellant thruster

Chapter 2 Spreading of a liquid film on a cold surface formed by an oblique jet impingement

2.1 Introduction

Bipropellant thrusters generally employ a film cooling technique, in which a part of the liquid fuel is obliquely injected onto the chamber wall to form liquid films, for protecting the chamber wall from high-temperature combustion gases and preventing thermal failure. The flow rate of the fuel for film cooling needs to be reduced and optimized for achieving a higher specific impulse and the heat resistance of the chamber wall [1]. At the start of the steady state firing mode, fuel liquid jets are injected from the outermost injection holes of the face plate as shown in Fig. 1.3 onto the cold surface whose temperature is below the saturated temperature of the fuel. In the product design and development of the face plates, the nozzle diameter, interval between each injection hole, impingement angle, and distance from the face plate to the chamber wall (i.e., liquid jet length) are the important design parameters that can affect the cooling performance. In the development stage, the decision on the geometry of the face plate strongly depends on multiple cost- and time-consuming combustion tests to understand the sensitivities of the parameters to the cooling performance [2, 3]. To achieve the reduction and optimization of the liquid fuel used for the liquid film cooling based on the physical phenomena, a deeper understanding of the formation processes of the liquid film is required.

However, there are few studies on the liquid film formation through an oblique jet impingement onto the cold wall [4]. The distribution of the liquid film under the conditions of the extremely low flow rate (< 7 g/s), small nozzle diameter (< 2 mm), and shallow impingement angle (< 25°), which is in the range of the design values of the face plates, have not been examined especially [5]. Consequently, in this chapter, to understand the formation processes of a liquid film and extract key physical parameters to the liquid film shape, experiments were conducted under conditions involving a low flow rate, small nozzle diameter, and shallow impingement angle as mentioned above. In addition, the effect of the liquid jet length on the film width was investigated, and an experimental analysis of the spread of liquid film was performed. Finally, a theoretical model for predicting the maximum film width, which is one of the representative parameters for the liquid film shape, was developed based on the experimental results.

2.2 Experimental apparatus

In actual bipropellant thrusters, the liquid films injected from multiple injection holes may interfere among one another. However, in this chapter, the liquid film formed by a single liquid jet was considered to understand the film formation process in detail. An experimental apparatus that simulated the method of film formation from a single hole was developed. Figure 2.1 shows a schematic of experimental apparatus. The experimental apparatus consisted of an injector part imitating a single injection hole, a metal plate simulating the chamber wall, an imaging system, and a liquid supply system. In the injector part, straight-type nozzles with different diameters could be employed to evaluate the effect of the nozzle diameter on the film formation. Nozzle diameters of 0.7 mm and 1.1 mm were considered, which lie in the design range of the actual face plate. The nozzle was a straight shape, and its exit port had no specific treatment. The injector part was set on a three-axis traverse system and a goniometer stage to change the liquid jet length (i.e., the distance between the nozzle and impingement point) and impingement angle. The liquid jet length and impingement angle could be adjusted within the design range. On the three-axis traverse system, the injector part moved ± 6.5 mm and ± 5 mm on the XY and Z axes with a precision of 0.01 mm. The dimensionless liquid jet length, that is, the ratio of the liquid jet length to the nozzle diameter was set as 6, 8, 10, and 20. Although the value of 20 was beyond the design range, the test was conducted to investigate the effect of the liquid jet length in detail. The goniometer could be adjusted in the angle range of ± 20° with a precision of 0.1°. The impingement angle was varied from 10° to 25° in increments of 5°.

Water was used as the test liquid instead of liquid fuels for avoiding the toxicity of hydrazine-derivative fuels. The density and surface tension of water are similar to those of hydrazine, which make water a suitable test liquid to investigate the film spread phenomenon. In the experiments, water was supplied to the nozzle from the test liquid tank which was pressurized by air. The mass flow rate was varied from 3.0 g/s to 6.0 g/s in increments of 1.0 g/s by using a mass flow meter with a needle valve. A flat plate of stainless steel was used to simulate the chamber wall because the area where a liquid film was formed with respect to the circumference of combustion chamber wall was small. The surface of the plate was polished with #400 buffing. The experimental conditions are listed in Table 2.1. The behavior of the film spreading was observed by using a camera (Baumer VCXG-124M) to perform imaging from the top of the plate. A bright metal halide lamp (Sumita optical glass LS-350) was selected as a light source. The resolution and exposure time was 31 μm/pixel and 20 ms, respectively. Figure 2.2 shows an example

of the film image recorded using the imaging system. Specifically, using this imaging system, the state in which a liquid jet impinges on the wall obliquely and forms a liquid film could be observed. The distance from the impingement point was defined as x, and the half film width at each x was $w/2$. The maximum half-film width at each condition was defined as $(w/2)_{max}$. The half film width value was considered because the light irradiated obliquely from above, and the film width could be measured accurately by considering the brightness of the outer edge of the film on the light source side. Furthermore, the film shape was symmetric, and only the half value of the film width was thus required to be considered.

2.3 Results and discussion

2.3.1 Formation process of liquid film

A liquid film spreads owing to the momentum immediately after the liquid jet impinges onto the wall, and subsequently, the film shrinks because of the surface tension. The shape of the film is a result of the balance between the inertia of the liquid film and surface tension.

When a liquid jet is injected from a nozzle into the ambient air, the unstable waves on the surface of the liquid jet grow owing to the interfacial instability, and the liquid jet breaks up. Since the growth of the unstable waves before the impingement of the liquid jet onto the wall affects the film formation, the effect of L/d on the film formation was investigated. Where L and d represent the liquid jet length and nozzle diameter, respectively. The impingement angle was fixed as 10°, and the nozzle diameter was set as 0.7 mm and 1.1 mm to investigate the effect of the nozzle diameter. Figure 2.3 shows the direct images of the film at each L/d condition with d = 0.7 mm. As the value of L/d increased, droplets appeared around the impingement point. These droplets were thought to be a desecrated from the liquid jet surface owing to the instability on the liquid surface. The deformation on the surface of the liquid jet increased with an increase in the distance to the impingement point (L). However, the film shape did not significantly change with a change in the L/d value. Figures 2.4 and 2.5 show the values of $w/2$ at each x for each L/d value under the conditions of d = 0.7 mm and 1.1 mm. No significant difference in the film width was observed. The breakup length of the inviscid liquid jet, L_b, can be expressed as in Eq. (2.1) [6, 7].

$$\frac{L_\text{b}}{d} = 1.04C\sqrt{We} \qquad (2.1)$$

The Weber number can be expressed as follows.

$$We = \frac{\rho V_0^2 d}{\sigma} \qquad (2.2)$$

where V_0, ρ, and σ denote the liquid jet velocity, the density, and the surface tension coefficient of the liquid, respectively. The value of V_0 was obtained by dividing each mass flow rate by the density and cross-sectional area of the liquid jet. In Eq. (2.1), C indicates the disturbance factor, and a value of $C = 13$ was used in the case of low-viscosity liquid jets, according to Grant and Middleman [8]. Because the experimental conditions in this work involved $We = 143$ to 2438, the breakup length of the liquid jet was calculated as $L_\text{b}/d > 162$ by using Eq. (2.1). The tests were conducted with L/d ranging from 6 to 20, thus the growth of the instability on the surface of the liquid jet was considered to be small. Furthermore, in the experimental conditions of this work, $Re = 3387$ to 10839; therefore, the liquid jets were likely turbulent flows. Consequently, the value of L/d in this chapter was compared with the breakup length of the liquid jet in the turbulence region. According to Grant and Middleman [8], the breakup length of the liquid jet under a turbulent region was expressed as in Eq. (2.3).

$$\frac{L_\text{b}}{d} = 8.51\left(\sqrt{We}\right)^{0.64} \qquad (2.3)$$

Under the lowest value of We in this chapter (i.e., 143), the breakup length of the turbulent liquid jet was calculated as $L_\text{b}/d = 42$ from Eq. (2.3). The value of L/d in this chapter was smaller than $L_\text{b}/d = 42$, and it was considered that the growth of the instability of the liquid jet was small, and the film formation was not affected even if the liquid jet transitioned to the turbulent region. These results indicated that the liquid jet length did not affect the film formation when the value of L/d was within the range of the considered experimental conditions and the design range of actual thrusters.

Figure 2.6 shows the images of the films formed under different conditions of the mass flow rate and nozzle diameter, with the impingement angle fixed as 10°. As shown in Figs. 2.6 (a) and (b) (or (c) and (d)), the width and length of the film, which was defined as the distance from the impingement point to the point where the liquid film shrank to

the width at impingement point, increased with an increase in the mass flow rate because the liquid jet velocity increased with the mass flow rate. In addition, by comparing Figs. 2.6 (a) and (c) (or (b) and (d)), no significant difference was noted between the film width pertaining to d = 0.7 mm and 1.1 mm. Furthermore, the length of the film in the case of d = 0.7 mm was larger than that when d = 1.1 mm under the same mass flow rate, especially for the lower mass flow rates. This is because the liquid jet velocity of d = 0.7 mm was higher than that for d = 1.12 mm under the same mass flow rate.

Figure 2.7 shows the relationship between V_0, and $(w/2)_{max}$ under each nozzle diameter condition. The mass flow rate was set as 3.0, 4.0, 5.0, and 6.0 g/s. The results shown in Fig. 2.7 correspond to the average values of $(w/2)_{max}$ obtained by testing three times for each mass flow rate. It was noted that $(w/2)_{max}$ increased with an increase in V_0. In addition, a linear relationship existed between V_0 and $(w/2)_{max}$ at each nozzle diameter as reported by Good and Nollet [5], although the slope differed depending on the nozzle diameter. This finding suggests that the nozzle diameter is a critical factor that affected the spread of a liquid film.

Figure 2.8 shows the images of the typical film formed on the test plate recorded at each impingement angle condition. The nozzle diameter was 1.1 mm, and the mass flow rate was set as 5.0 g/s. When the impingement angle increased, the liquid film width expanded while its length became shorter. Figure 2.9 shows the relationship between V_0 and $(w/2)_{max}$ under each condition of the nozzle diameter and mass flow rate. It can be found from Fig. 2.9 that the maximum film width increased as the impingement angle increased. Furthermore, the parameters exhibited a linear relationship under all the impingement angle conditions. However, the film length downstream decreased as the impingement angle increased, as mentioned above. These findings pertaining to the width and length of the film indicated that the component of the liquid jet velocity perpendicular to the wall (i.e., $V_0 \sin\theta$, see Fig. 2.1) contributed to the film width, and the horizontal component (i.e., $V_0 \cos\theta$) contributed to the length. Figure 2.10 shows the relationship between $V_0 \sin\theta$ and $(w/2)_{max}$. Under each nozzle condition, the results under different angles shown in Fig. 2.11 corresponded to those pertaining to $V_0 \sin\theta$, and linear relationships between $V_0 \sin\theta$ and $(w/2)_{max}$ were observed under each condition of the nozzle diameter.

2.3.2 Film width characterization

To identify the relationship between $(w/2)_{max}$ and the key factors under various conditions, the parameters influencing the film width were examined, and it was noted

that $V_0 \sin\theta$ and d influenced the film width.

As a linear relationship was noted between $V_0 \sin\theta$ and $(w/2)_{max}$, it could be considered that the scale of $(w/2)_{max}$ could be expressed by the product of $V_0 \sin\theta$ and the characteristic time for the film spread, as the scale of the length can be expressed in terms of the product of the scales of the velocity and time. The characteristic time scale for the film spread, τ_σ, can be expressed as in Eq. (2.4), as determined via a dimensional analysis using the density, surface tension coefficient, and nozzle diameter, which are the key factors influencing the film width. Thus, the scale of $(w/2)_{max}$ can be expressed as in Eq. (2.5).

$$\tau_\sigma \sim \sqrt{\frac{\rho d^3}{\sigma}} \qquad (2.4)$$

$$(w/2)_{max} \sim V_0 \sin\theta \cdot \sqrt{\frac{\rho d^3}{\sigma}} \qquad (2.5)$$

By rearranging Eq. (2.5), the dimensionless maximum film width can be expressed as follows:

$$\frac{(w/2)_{max}}{d} \sim \sqrt{\frac{\rho (V_0 \sin\theta)^2 d}{\sigma}} = \sqrt{We} \cdot \sin\theta \qquad (2.6)$$

In addition, it can be considered that $(w/2)_{max}$ is equal to $d/2$, the radius of the liquid jet, if the liquid jet impinges to the wall with $\theta = 0$. Therefore, a correction term of 0.5 was added to Eq. (2.6), as follows:

$$\frac{(w/2)_{max}}{d} = \sqrt{We} \cdot \sin\theta + 0.5 \qquad (2.7)$$

All the obtained results considering the different parameters are shown in Fig. 2.11. It is found that the results under various conditions of the liquid jet velocity, nozzle diameter, and impingement angle could be uniformly organized although the data indicated a slightly gentle slope than Eq. (2.7). These findings indicate that the maximum film width

31

for a liquid film formed by a single nozzle can predict when the injection conditions have been determined.

2.4 Conclusions

To clarify the key factors affecting the spread of a liquid film and to understand the formation process of such films, an experimental apparatus that simulates the supply system of the fuel in actual thrusters for film cooling has been developed. Experiments, in which a liquid jet was injected onto the cold wall under the different injection conditions, were performed using water as the test liquid. The mass flow rate, nozzle diameter, impingement angle, and liquid jet length were varied. Results showed that the width and length of the film increased when the liquid jet velocity increased. Additionally, a linear relationship existed between the liquid jet velocity and maximum film width. This tendency was observed at all nozzle diameters, although the slopes of the lines were different. These results indicated that the nozzle diameter was one of the factors affecting the film spread. The maximum film width increased under the same mass flow rate as the impingement angle increased, and the vertical component of the liquid jet velocity to the wall exhibited a linear relation with the maximum film width. In addition, the liquid jet length did not exert any significant influence on the film width under the experimental conditions, which were in the design range of bipropellant thrusters. Based on these results, the key factors affecting the film width were extracted, and a general relationship between the key factors and maximum film width under various conditions was identified. The maximum film width divided by the nozzle diameter could be uniformly organized in terms of the product of the Weber number and the sine of the impingement angle, based on dimensional analysis. These findings could provide guidance to determine the shape of an injector for film cooling, based on the physical phenomenon, instead of using a trial-and-error approach that requires experimental tests. In addition, the amount of fuel for film cooling could be optimized while ensuring high performance and sufficient cooling of the thrusters at the same time.

In future work, the effect of the surface tension must be investigated in detail by using different test liquids. In addition, the reason why the data was not completely fitted with Eq. (2.7) needs to be elucidated. For more accurate prediction, it is necessary to consider the effects of the contact angle and modify the characterization parameters suitably.

References

[1] G. Fujii, Y. Daimon, K. Furukawa, C. Inoue, D. Shiraiwa, and N. Tanaka, "Visualization of Coolant Liquid Film Dynamics in Hypergolic Bipropellant Thruster," *Journal of Propulsion and Power*, vol. 38, no. 2, pp. 267-273, 2022.

[2] S. Takata, Y. Daimon, K. Sugimori, N. Matsuda, and Y. Tashiro, "Design verification results of japanese 120N Bi-propellant thrusters (HBT-1) based on its first flight in HTV3," *49th AIAA/ASME/SAE/ASEE Joint Propulsion Conference*, AIAA-2013-3754, 2013.

[3] Y. Daimon, H. Negishi, H. Tani, Y. Matsuura, S. Iihara, and S. Takata, "Flow field and heat transfer analysis in a MON/MMH bipropellant rocket engine," *International Journal of Energetic Materials and Chemical Propulsion*, vol. 16, no. 3, pp. 263-280, 2017.

[4] M. W. L. Chee, P. Chauhan, J. Georgiou, and D. I. Wilson, "Flow distribution in the liquid film created by a coherent circular water jet impinging obliquely on a plane wall," *Experimental Thermal and Fluid Science*, vol. 140, Article 110748, 2023.

[5] R. M. Good and W. K. Nollet, "Fluid Film Distribution Investigation for Liquid Film Cooling Application," *53rd AIAA/SAE/ASEE Joint Propulsion Conference*, AIAA-2017-4920, 2017.

[6] J. W. Strutt and L. Rayleigh, "On the Instability of Jets," *Proceedings of the London Mathematical Society*, Vol.10, No.4, pp.4–13, 1878.

[7] C. Weber, "On the breakdown of a fluid jet", *Zeitschrift für angewandte Mathematik und Physik*, Vol.11, pp.136-159, 1931.

[8] R. P. Grant, and S. Middleman, Newtonian Jet Stability, *AIChE Journal*, Vol.12, No.4, pp.669–678, 1966.
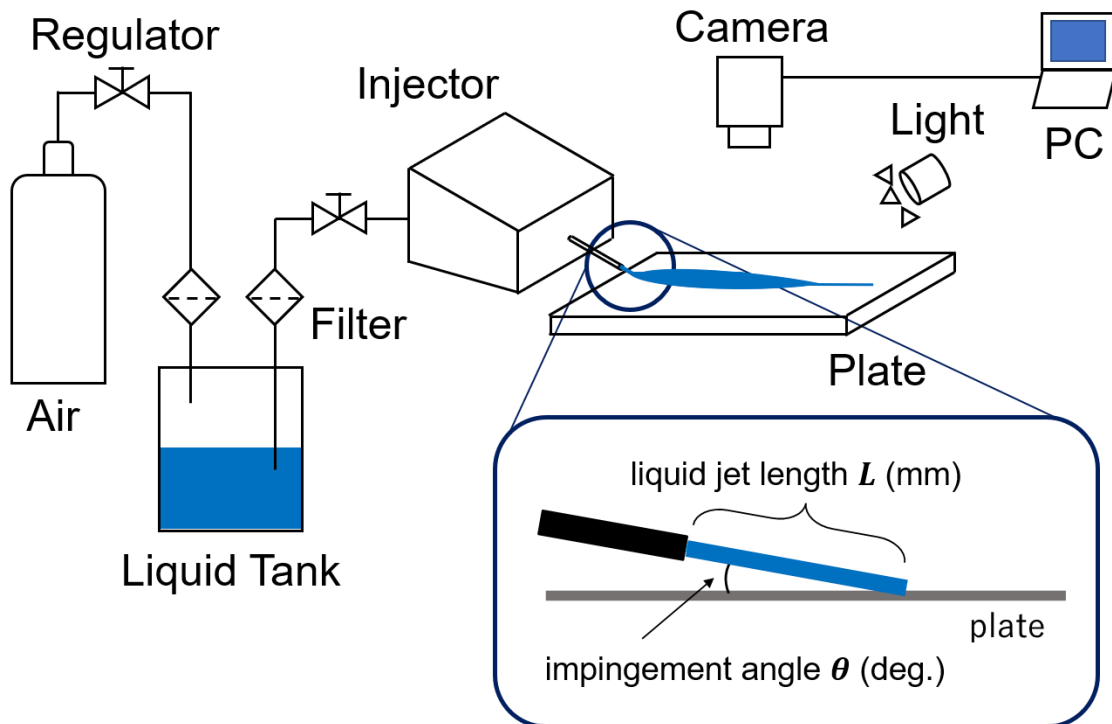
Fig. 2.1 Schematic of the experimental apparatus
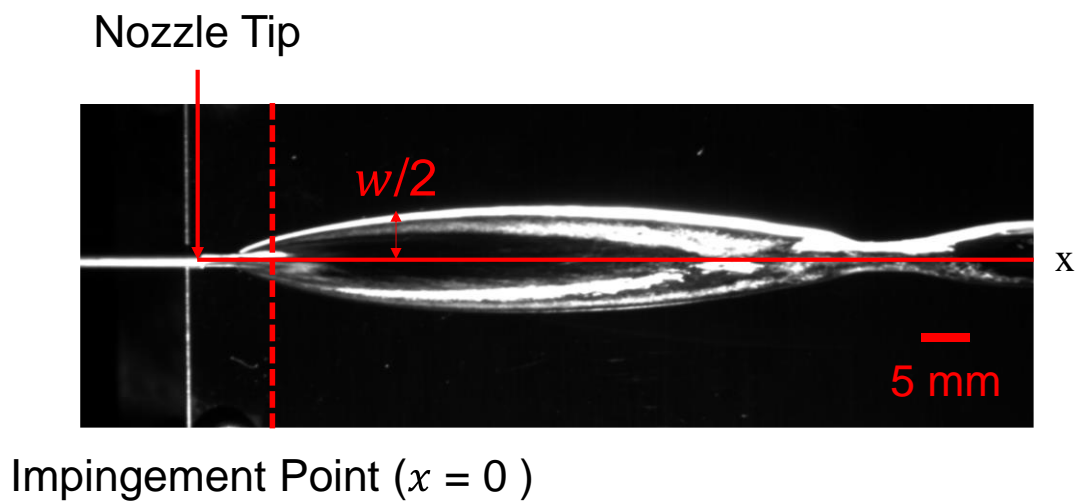
Fig. 2.2 Direct image of film and defined values
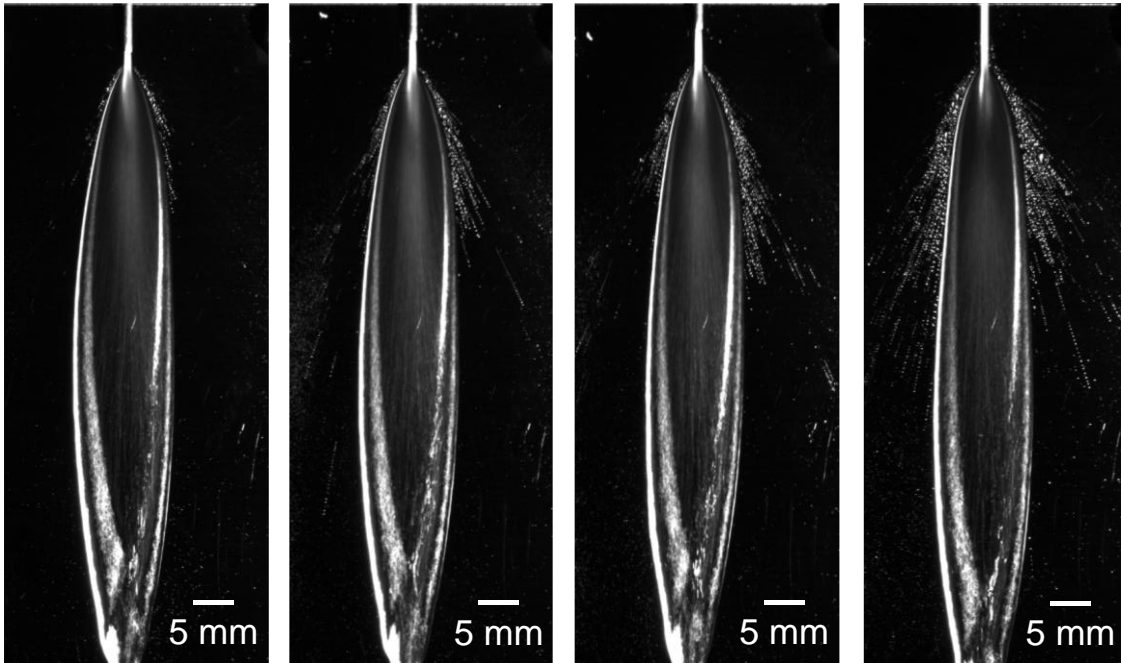
Fig. 2.3 Effect of liquid jet length on the film spread under a nozzle diameter of 0.7 mm
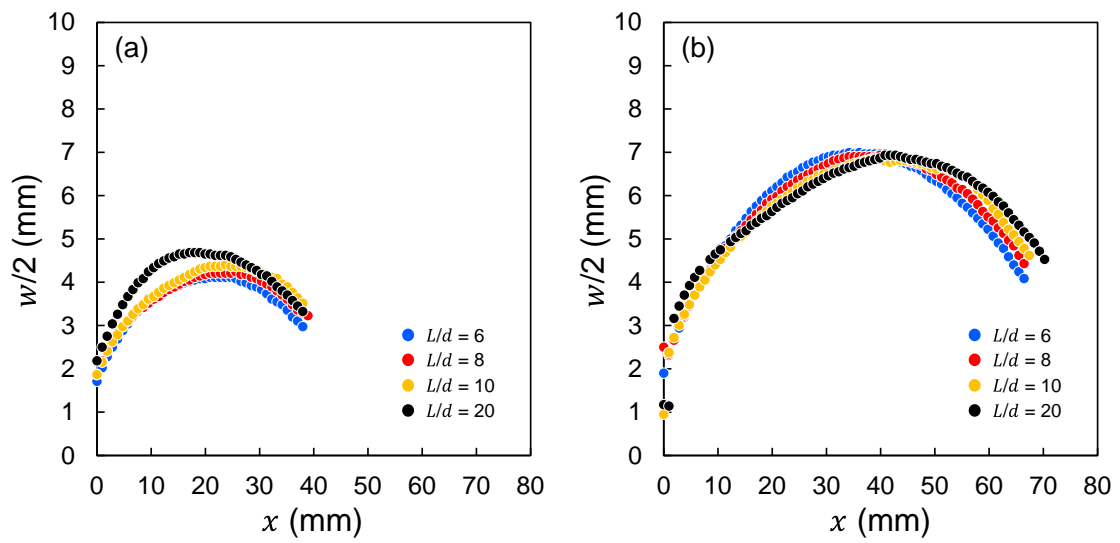
Fig. 2.4 Effect of liquid jet length on film width at d = 0.7 mm; (a) 3.0 g/s, (b) 6.0 g/s
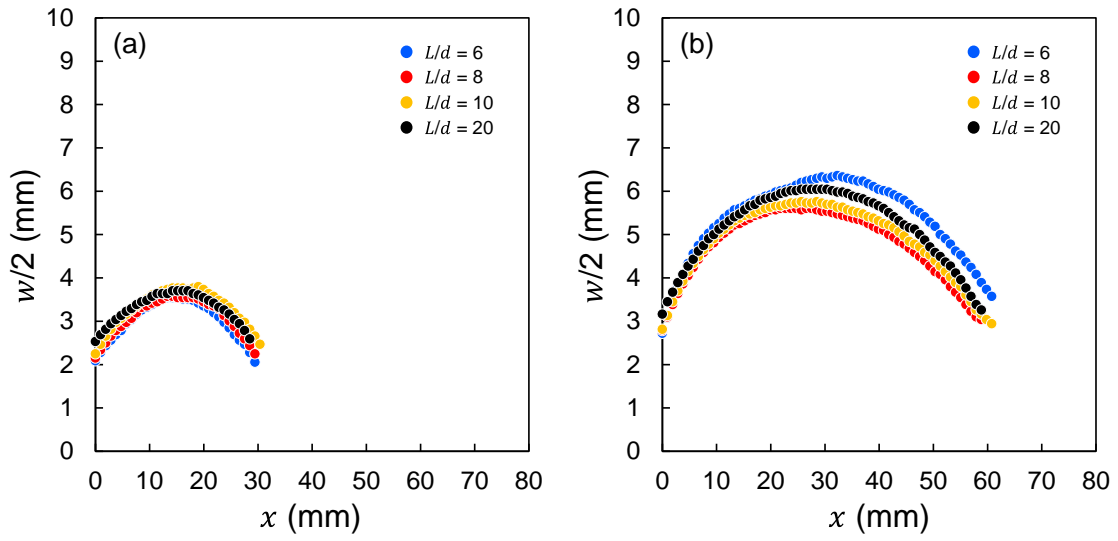
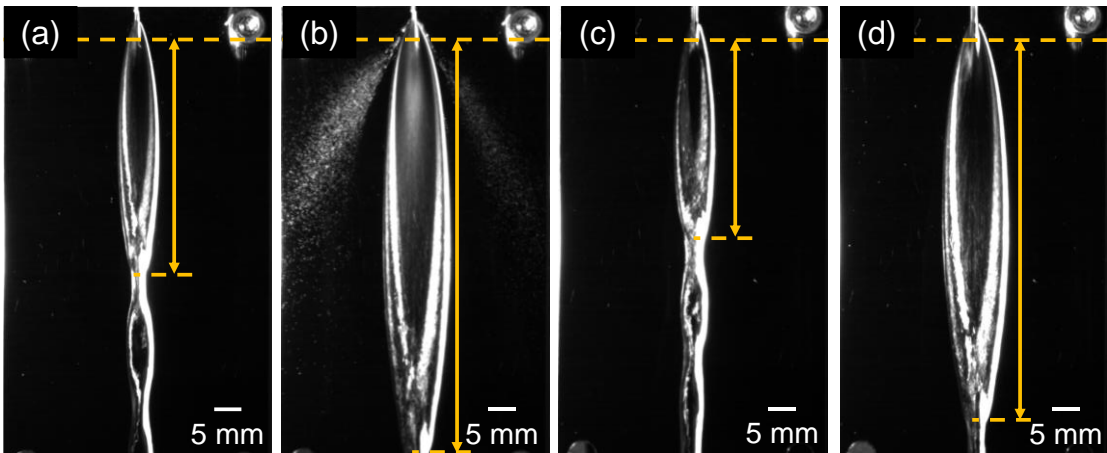Fig. 2.5 Effect of liquid jet length on film width at d = 1.1 mm; (a) 3.0 g/s, (b) 6.0 g/s

Fig. 2.6 Film spreading under different conditions of mass flow rate and nozzle diameter at the impingement angle of 10°. The impingement points were on the upper broken line, and two direction arrows indicated the length of the film under each condition
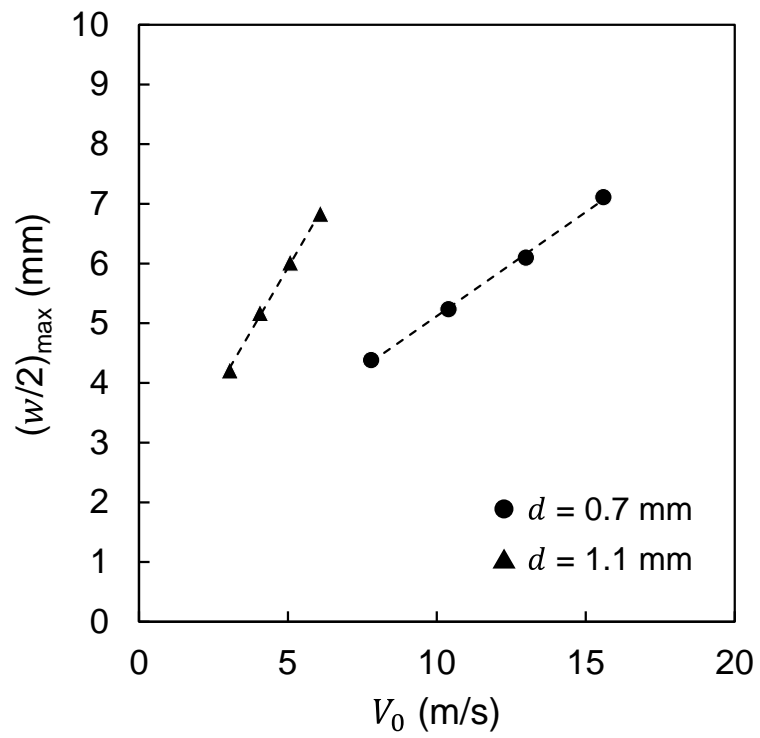
Fig. 2.7 Effect of nozzle diameter on the maximum film width
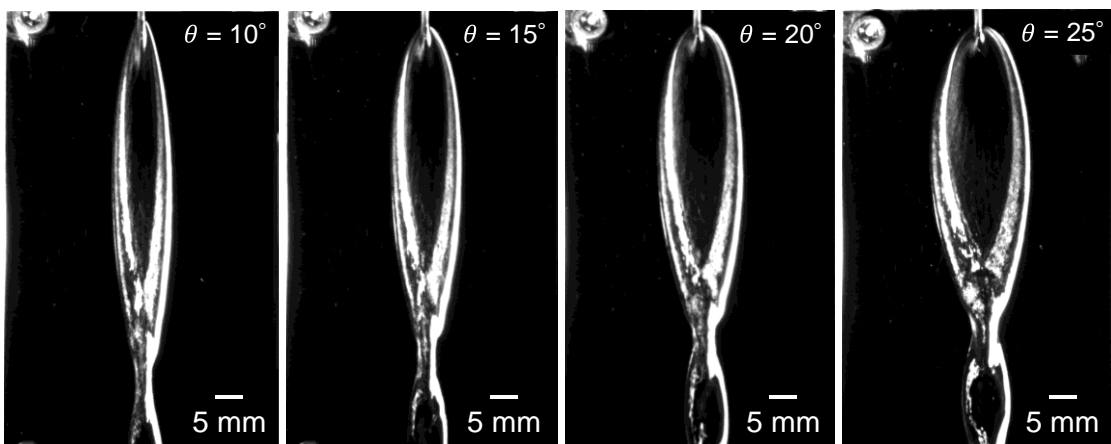
Fig. 2.8 Effect of impingement angle on the film spread
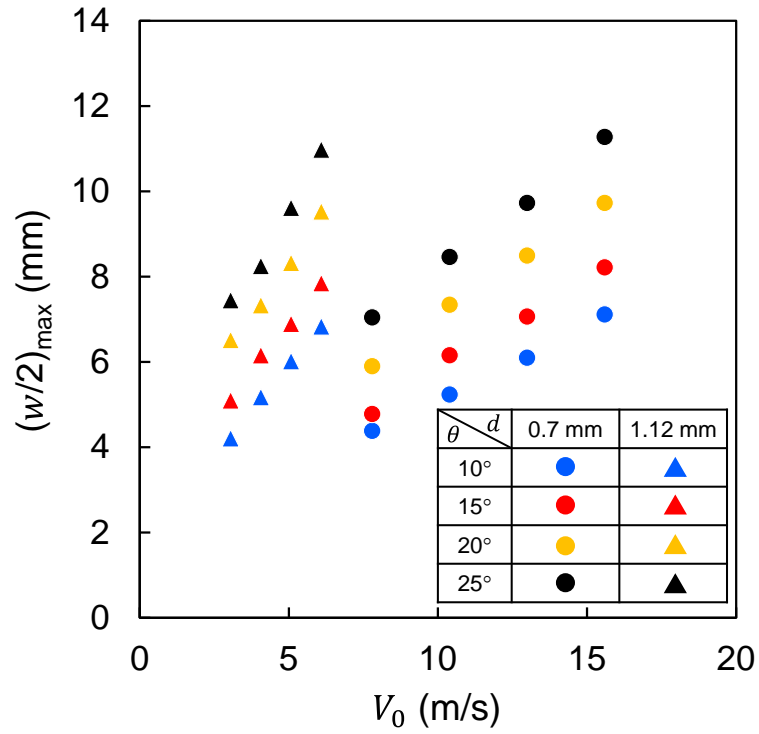
Fig. 2.9 Effect of impingement angle on the maximum film width
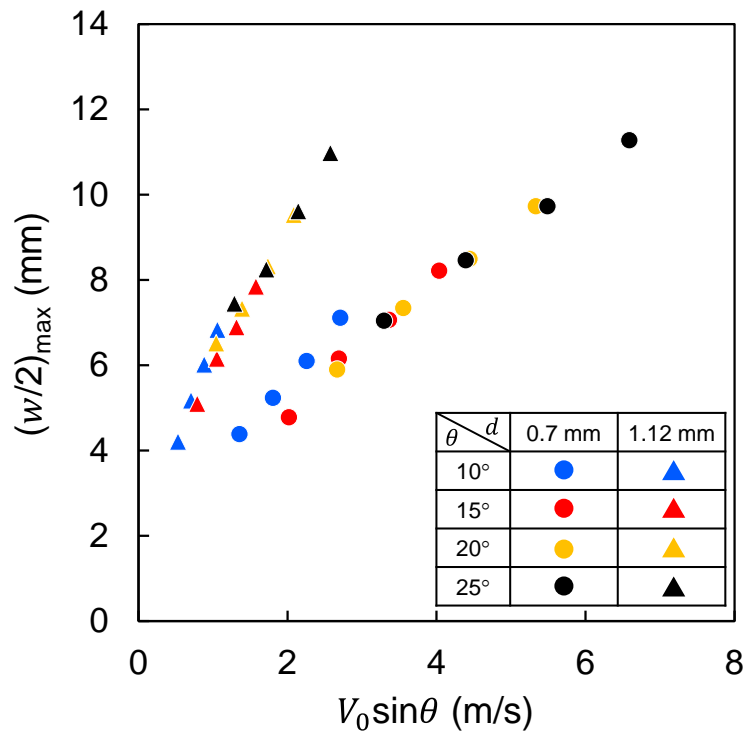
Fig. 2.10 Relationship between the inlet jet velocity perpendicular to the wall and maximum film width
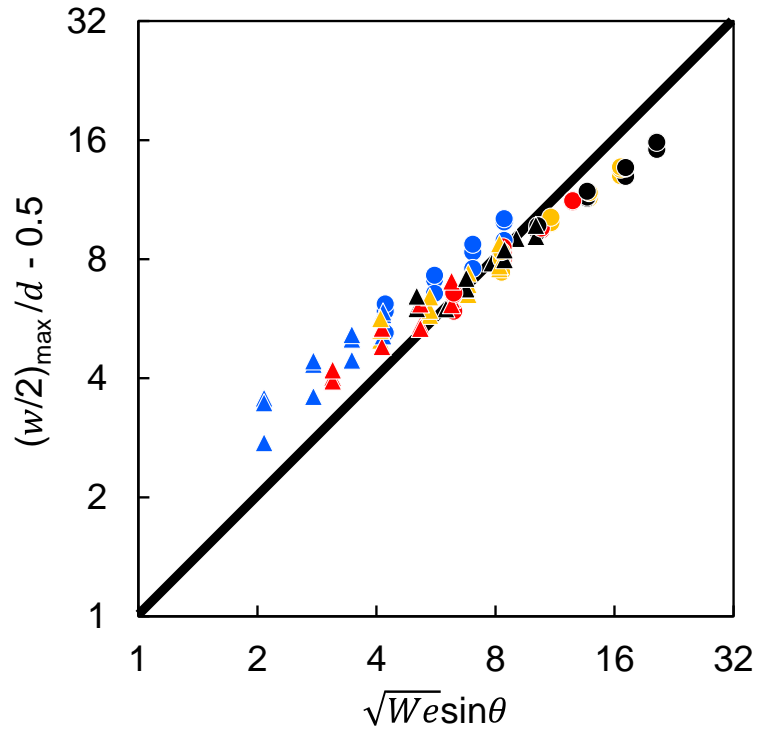
Fig. 2.11 Relationship between dimensionless maximum film width and the product of We and $\sin\theta$. The symbols indicate the experimental data for three experimental runs in each condition. The bold line indicates the results pertaining to Eq. (2.7).

Table 2.1 Experimental conditions and imaging conditions

Mass flow rate of test liquid	[g/s]	3.0, 4.0, 5.0, 6.0
Nozzle diameter	[mm]	0.7, 1.1
Impingement angle	[deg.]	10, 15, 20, 25
Dimensionless length of liquid jet	[-]	6, 8, 10, 20

Chapter 3 Formation processes and heat transfer characteristics of a liquid film on a superheated wall during continuous injection

3.1 Introduction

Impinging jet cooling by forming a liquid film is widely used in many applications demanding high heat dissipation, such as material processes [1, 2, 3] and cooling of nuclear reactor cores [4, 5], because of its high cooling ability by the latent heat through a phase change from liquid to vapor. Bipropellant thrusters for orbit maneuvering and attitude control of satellites and small-scale spacecraft also employ the film-cooling technique using liquid jets of the fuel impinging onto the chamber wall [6, 7]. During the pulse firing mode of the thrusters, liquid fuel jets are possibly to be injected onto the superheated wall with a spatial temperature gradient along the axial direction whose temperature exceeds the saturated temperature or the Leidenfrost temperature of the fuel due to the heat soak-back.

When a liquid jet is injected onto a superheated surface, most of the liquid splashes away from the leading edge of the liquid film because of the vapor flow induced by vigorous boiling; the leading edge, which is the boundary between the wetted region by the liquid film and the dry region, is called as the wetting front (WF) [8, 9]. The WF behavior and the heat transfer characteristics in the vicinity of the WF required to be understood for the well-controlled cooling processes, and therefore, impinging jet cooling has been investigated for a long time. However, the physical model for the WF behavior has not still been elucidated [10], primarily owing to the poor understanding of the physical processes during the transient cooling [11].

Although there were several parameters affecting the film formation processes such as the momentum flow rate per unit length [12] and the impingement angle [13, 14], experimental results for the behavior of the WF and surface heat flux were discussed and organized, mainly focusing on the velocity of the liquid jet that was related to the velocity of the liquid film [15, 16, 17]. On the other hand, it was recently reported that the hydrodynamics of the WF and the heat transfer characteristics were determined by the flow rate of the test liquid [3]. This suggests that the WF behavior was not determined by the liquid film velocity affecting the behavior of the bubbles and vapor film but by the

amount of the liquid supplied to the WF. For a better understanding of the WF behavior, it needs to be confirmed which of the physical parameters are dominant. These physical factors are also considered to have significant effects on liquid film behavior on the chamber wall of the bipropellant thruster. In addition, from the viewpoint of the reduction in propellant consumption that leads to a higher performance of the bipropellant thruster and consequently a longer life of the satellite, the effect of the mass flow rate on the cooling processes needs to be examined further.

The objectives of this chapter are to evaluate whether the effect of the mass flow rate and the liquid jet velocity are dominant to the WF behavior and to investigate the heat transfer characteristics during oblique jet impingement quenching with a small amount of the test liquid in the case of the initial temperature distribution with a spatial gradient. The quenching of a heated metal plate with a spatial temperature gradient by water jet impingement was conducted to examine the effect of the liquid mass flow rate and liquid jet velocity by varying the nozzle diameter.

3.2 Experimental description

3.2.1 Experimental apparatus

Figure 3.1 shows a schematic illustration of the experimental apparatus used in the present chapter. While the liquid films injected from multiple injector holes may interfere with each other in the actual thruster, the quenching processes of a liquid film formed by a liquid jet were considered as the first step for understanding the cooling mechanism in the liquid film cooling. In this chapter, the impingement point of the liquid jet was defined as the origin. The $x, y,$ and z axes represent the direction of the liquid film flow, liquid film width, and perpendicular to the wall, respectively. The experimental apparatus consists of an injector part with a single nozzle, a metal plate (aluminum alloy (A5052), 3 mm thick, 50 mm wide, and 118 mm long), a liquid supply system, a high-speed camera, and an infrared camera. A rod heater was placed in the metal component on one side of the metal plate, and the plate was heated to form a spatial temperature gradient in the x direction. The behavior of the liquid film formed on the heated plate was observed from the front (as shown in Fig.3.2) and the side simultaneously by using two high-speed cameras (Photron FASTCAM SA-1.1 and Vision Research Phantom v2012). The frame rate and exposure time were 500 fps and 20 μs. The spatial resolution for the front view and the side view were 0.14 and 0.09 mm/pixel, respectively. In addition, the temperature distribution of the test plate was measured from the backside using an infrared camera

(NIPPON AVIONICS InfReC R550Pro). The backside of the test plate was coated with black body paint, ensuring an emissivity of 0.94. The frame rate for IR imaging was 60 fps with a spatial resolution of 0.23 mm/pixel. The measurement area for the temperature of the test plate was limited to 60 mm downstream from the impingement point owing to the metal component with the rod heater, as shown in Fig. 3.1.

Water was selected as the test liquid because the density and surface tension of water were similar to those of hydrazine. To investigate the effect of the mass flow rate on the quenching processes, two nozzles with the diameters of 0.7 mm and 1.1 mm were used and the mass flow rate of water was varied from 3.0 g/s to 6.0 g/s in the increment of 1.0 g/s. The ratio of the distance from the nozzle tip to the test plate to the nozzle diameter L/d was set to 6. Although the impingement angle influences the formation of the liquid film [13, 14], the impingement angle θ was selected as 10° to simulate the situation in the actual thruster. The test liquid at room temperature (approximately 20°C) was injected onto the test plate when the temperature of the impingement point was raised to 220°C. The experimental conditions are presented in Table 3.1. For each condition, the cooling tests were conducted five times.

3.2.2 Estimation of the temperature and heat flux of the surface by a liquid film

For the data acquisition of surface temperature and surface heat flux on the cooled surface (front surface), the inverse heat conduction problem should be solved because the value of the Biot number was higher than 0.1 and the temperature distribution in the thickness direction could not be negligible [18]. In the present chapter, a rectangular calculation domain with a length of 70 mm, a width of 50 mm (measurement area), and a thickness of 3 mm consisted of 105×75×30 cells. The time step was dependent on the frame rate of the infrared imaging and 1/60 s. Fujimoto et al. [19] conducted the three-dimensional steady-state inverse heat conduction analysis to estimate the surface heat flux and temperature distribution on the cooled surface of the test plate during the jet impingement cooling of the moving plate by using the measured temperature profile of the rear surface of the test plate. In Ref. [19], the authors applied the finite volume method. Recently, Haramura [20] proposed a robustly stable and easily usable scheme for solving the inverse problem of one-dimensional transient heat conduction with the fully implicit scheme, in which the finite difference method was applied. In the present study, the inverse problem of the transient three-dimensional heat conduction was numerically solved by employing the finite volume method as the discretization method and extending the scheme proposed by Haramura [20] from the one-dimensional problem to the three-

dimensional problem.

The transient heat conduction equation of the plate in the Cartesian coordinate as shown in the plate of Fig. 3.1 is given by Eq. (3.1).

$$\rho_{\mathrm{w}} c_{\mathrm{w}} \frac{\partial T_{\mathrm{w}}}{\partial t} = k_{\mathrm{w}} \left(\frac{\partial^2 T_{\mathrm{w}}}{\partial x^2} + \frac{\partial^2 T_{\mathrm{w}}}{\partial y^2} + \frac{\partial^2 T_{\mathrm{w}}}{\partial z^2} \right) \tag{3.1}$$

In the finite volume method [21], the discretization of Eq. (3.1) with the fully implicit scheme for a control volume P is described as Eq. (3.2). The neighbors of the control volumes are represented as E, W, N, S, T, and B, as shown in Fig. 3.2(a). Subscript of e, w, n, s, t, and b denote each of the faces of the control volumes.

$$a_P T_P = a_E T_E + a_W T_W + a_N T_N + a_S T_S + a_T T_T + a_B T_B + a_P^0 T_p^0 \tag{3.2}$$

Here,

$$a_E = \frac{k_{we} \Delta y \Delta z}{(\delta x)_e},$$

$$a_W = \frac{k_{ww} \Delta y \Delta z}{(\delta x)_w},$$

$$a_N = \frac{k_{wn} \Delta z \Delta x}{(\delta y)_n},$$

$$a_S = \frac{k_{ws} \Delta z \Delta x}{(\delta y)_s},$$

$$a_T = \frac{k_{wt} \Delta x \Delta y}{(\delta z)_t},$$

$$a_B = \frac{k_{wb} \Delta x \Delta y}{(\delta z)_b},$$

$$a_P^0 = \frac{\rho_{\mathrm{w}} c_{\mathrm{w}} \Delta x \Delta y \Delta z}{\Delta t},$$

$$a_P = a_E + a_W + a_N + a_S + a_T + a_B + a_P^0.$$

T_P^0 is the temperature of P in the previous time step. The time step and grid sizes for x, y and z directions were represented as Δt and Δx, Δy, Δz, respectively. The distance between the cells were denoted by δx, δy, and δz in each direction. The front and rear surfaces of the tested plate are set to be the boundaries of the computational domain. Designating the control volumes of row 1 as shown in Fig. 3.2(b), the

43

temperature of the control volumes in the upper row are calculated from Eq. (3.3) which is the rearranged form of Eq. (3.2).

$$T_T = \frac{1}{a_T}(a_P T_P - a_E T_E - a_W T_W - a_N T_N - a_S T_S - a_B T_B - a_P^0 T_P^0) \qquad (3.3)$$

If the boundary condition of the rear surface is given, the temperature of the control volumes in row 1 can be obtained. Then, the temperature in row 2 are obtained by the discretized equation for the control volumes in row 1. Using these values and Eq. (3.3), the temperature for upper rows can be derived in order. The last nodes in row N+1 shown in Fig. 3.2(b) are the virtual points located outside of the plate, and the surface temperature and heat flux are determined from the temperature of the control volumes in rows N and N+1, thermal conductivity, and the distance between row N and row N+1.

When calculating the temperature and heat flux of the front surface, the initial condition should be given. Figure 3.3 shows the difference between the temperature at a certain point on the front surface measured by a K-type thermocouple which has an error of ±2.5°C under the measured temperature range and that on the rear surface measured by an infrared camera, during the plate heating. Owing to the heat resistance of the thermocouple, the range of the measured temperature was below the initial condition, and it was confirmed that there was a slight temperature difference between the front surface and rear surface before the cooling. However, the difference between the two surfaces was within the tolerance of the thermocouple. Therefore, the temperature distribution in the thickness direction of the plate at $t = 0$ s was assumed to be uniform, and the temperature profile of the rear surface was given as the initial condition. For the boundary conditions of the surfaces, zero temperature gradient conditions were given at the side boundaries in the y direction and the rear surface. The upstream side boundary in the x direction was also zero temperature gradient condition, and the downstream side boundary in the x direction was given by the heat flux determined by the thermal conductivity of the plate and the temperature gradient in the x direction at $t = 0$ s. In the present study, the metal properties of the aluminum alloy (A5052) were assumed to be constant ($\rho_w = 2680$ kg/m³, $c_w = 900$ J/ kg・K, and $k_w = 137$ W/m・K).

In this method, the noises superposed on the temperature measurement have quite severe effects on determining the surface temperature and heat flux [19, 20]. Therefore, smoothing operations needed to be performed for the spatial directions and temporal direction before the calculation. The smoothing methods used for the spatial directions and temporal direction in the present study were cubic smoothing splines and the

Savitzky-Golay method [22], which were also used in [19] and [20] respectively. The smoothing procedure was as follows: first, a smoothing operation using cubic smoothing splines was performed on the temperature profile data at each time by using a Python package CSAPS [23], and then the Savitzky-Golay method [22] was applied to the change of the temperature at each point as shown in Fig. 3.4.

3.3 Results and discussion

3.3.1 Wetting front propagation

Figure 3.5 (a) and (b) show the progress of the liquid film and the WF position on the x-axis as measured from the images under the condition of $\dot{m}$ = 5.0 g/s and d = 0.7 mm. As explained later, the red solid line in Fig. 3.5 (b) indicates the fitting result of the WF position obtained by using Eq. (1.3). It can be observed in Fig. 3.5 that the liquid film expanded in the y direction and the WF moved downstream with the elapsed time since the cooling commenced. In addition, the velocity of the WF slowed down as the WF moved downstream, and this trend was also observed in the previous studies on quenching of the hot surface with vertical jet impinging [3, 16, 23, 24].

Figure 3.6 shows the direct image of the liquid film and the distributions of the estimated surface temperature and heat flux at t = 0.6 s after the cooling commenced. The maximum heat flux position lay in the wetted region near the WF as observed in [15, 17, 26] and the WF and maximum heat flux position were quite close [17]. In addition, the WF was located in the region where the spatial temperature gradient in the direction of the liquid film flow was the largest. Figure 3.7 shows the relationship between the position where the temperature gradient along the x direction achieved its maximum value x_{g} and the WF position x_{wf} under the condition of d = 0.7 mm and $\dot{m}$ = 5.0 g/s. These positions were consistent at any location from the impingement point; this agrees with the observations of Karwa and Stephan [17]. From the viewpoint of film cooling in an actual thruster which is difficult to visualize, this suggests that the length of the liquid film can be estimated from the distribution of the wall temperature observed in an actual thruster [27].

The effects of the liquid jet velocity and mass flow rate on the WF propagation were evaluated by varying the nozzle diameter under each mass flow rate condition. Figure 3.8 shows the time taken for WF to reach each position (x = 10, 20, 30, 40, and 50 mm) on the x-axis. The plots indicate the mean values of the five tests, and the error bars represent the maximum and minimum values in the five tests. The time required for the

WF to reach certain positions increased further downstream under all the experimental conditions, which meant that the WF velocity decreased as the WF moved downstream as seen in Fig. 3.5. Although the WF reached the position of $x = 50$ mm faster for the nozzle diameter of 0.7 mm under the conditions of $\dot{m} = 3.0$ and 4.0 g/s, the time required for the WF to reach each position was almost the same under the same mass flow rate conditions. It can also be seen from Fig. 3.8 that regardless of the nozzle diameter the WF moved downstream faster with an increase in the mass flow rate. The liquid jet velocity increased by approximately 2.5 times when the nozzle was changed from 1.1 mm to 0.7 mm, and it led to the difference in the liquid film velocity. However, the effect of the mass flow rate appeared to be greater than that of the liquid jet velocity in the range of the experimental conditions used in this chapter (see Fig. 3.8), which corresponded to the results under the higher flow rate conditions [3].

Figure 3.9 shows the mean velocity of the liquid film and the film mass flow rate per unit liquid film width on the x axis under the condition of $\dot{m} = 5.0$ g/s, which Inamura et al. [13] theoretically predicted for the liquid film formed by an oblique jet impinging on the non-heated wall. The mean liquid film velocity for $d = 0.7$ mm was higher at any position than that for $d = 1.1$ mm, while the film mass flow rate per unit liquid film width was almost the same for both; it was suggested that the mass flow rate, that is, the amount of the liquid supplied to the WF, was highly significant to the reduction of the plate temperature at the WF, leading to the faster movement of the WF with the increase of the mass flow rate.

As indicated in section 1.4.2, Karwa et al. [23] suggested the two possible reasons why the WF velocity decreased further downstream. The liquid film velocity may have negligible effects on the WF propagation. Therefore, the latter reason of Karwa et al. [23], i.e., the degree of heat the liquid film receives from the plate between the impingement point and the WF, may explain the deceleration of the WF propagation; the effect of the thermal boundary layer on the propagation of the WF was significant, compared with the effect of liquid film velocity. When the WF was located relatively close to the impingement point, the thickness of the thermal boundary layer in the liquid film was thin, and the bubbles condensed immediately after the initiation of growth, owing to subcooling. Furthermore, the thermal boundary layer of the liquid film at the WF thickened as the WF moved downstream, and it might have led to the growth of bigger bubbles and the prevention of WF propagation.

In the previous studies [16, 24, 25], the WF position was often expressed using Eq. (1.3). In the present study, the WF position on the x-axis was well-fitted by Eq. (1.3), as shown in Fig. 3.5. Figure 3.10 shows the effects of the mass flow rate and liquid jet

velocity on the constant a and exponent n. As shown in Fig. 3.10(a), the value of constant a increases linearly with an increase in the mass flow rate, implying that the value of constant a was independent of the liquid jet velocity. These results agreed with the results reported in Ref. [16] because the increase in the liquid jet velocity corresponded to an increase in the liquid mass flow rate under the condition of a fixed nozzle diameter. It was also found in Fig. 3.10(b) that the value of the exponent n decreased slightly with the mass flow rate under the condition of d = 0.7 mm, while it remained almost constant under the condition of d = 1.1 mm. Furthermore, the value of exponent n for $d = 0.7$ mm is slightly higher than that for $d = 1.1$ mm, under the same mass flow rate conditions. The values were in the range of approximately $0.4 - 0.5$, close to the values reported in Refs. [16] and [24]. For a constant a and exponent n, the same tendency as that in the previous studies on quenching with vertical jet impingement was observed in this study, where the liquid jet was obliquely injected onto the plate with a spatial temperature gradient.

3.3.2 Heat transfer characteristics during quenching process

Figure 3.11 shows the time history of the temperature for the front and rear sides at each position on the x-axis under the condition of $\dot{m}$ = 5.0 g/s and d = 0.7 mm. The solid lines and broken lines indicate the front and rear surface temperatures, respectively. The black dots indicate the temperature of the front surface when the WF reached each position. The front surface temperature dropped steeply compared to the rear surface temperature. The surface temperature at the instant WF position reached the measurement point took a constant value of approximately 200°C up to around x = 20 mm. That temperature decreased as the WF moved downstream. The temperature decreased from its initial value before the arrival of the WF further downstream. This is due to the conduction of heat by the plate between the wetted regions and dry regions. The area that exhibits temperature decrease, despite not being wetted by the liquid film, is named as the precursory cooling zone (PCZ) [28]. Figure 3.12 shows the value of the Peclet number as defined in Eq. (3.4) [29, 30] at each position.

$$Pe = \frac{u_{\mathrm{wf}}\delta}{\alpha_{\mathrm{w}}}.$$
(3.4)

u_{wf} and α_{w} indicate the WF velocity and thermal diffusivity of the test plate, respectively. In the present study, the WF velocity at each position (x = 10, 20, 30, 40,

and 50 mm) was calculated as the ratio of the distance between each position (10 mm) to the time taken to travel from one position to another. As shown in Fig. 3.12, the value of the Peclet number decreased in the downstream. This means that the effect of the thermal diffusion gradually increased, and it adequately accounted for the prominent precursory cooling effect by the heat conduction through the plate, in the downstream, as shown in Fig. 3.11.

Figure 3.13 shows the time history of the surface heat flux, at each position under the condition of $\dot{m} = 5.0$ g/s and $d = 0.7$ mm, for evaluating the heat transfer characteristics between the liquid film and the test plate. The maximum heat flux at each position was achieved after the WF passed, as discussed in section 3.3.1. Subsequently, the cooling mode gradually shifted from the nucleate boiling to the single-phase forced convection. As shown in Fig. 3.13, the value of the maximum heat flux achieved at each position decreased with an increase in the distance from the impingement point. This tendency was reported in the previous studies on the quenching of hot surfaces with vertical jet impingement [17, 25]. Figure 3.14 shows the boiling curves at each position on the x-axis under the condition of $\dot{m} = 5.0$ g/s for $d = 0.7$ and 1.1 mm. ΔT_{sup} denotes the degree of wall superheat which means the difference between the plate (wall) surface temperature and the saturated temperature of the test liquid. The peak value of the heat flux decreased further downstream as shown in Fig. 3.13, although the degree of wall superheat at the maximum heat flux point was nearly constant. Comparing Fig. 3.14(a) and (b), the heat flux for $d = 0.7$ mm in the single-phase convection regime was higher than that for $d = 1.1$ mm because the liquid film velocity for $d = 0.7$ mm was higher than that for $d = 1.1$ mm as shown in Fig. 3.9, while the values of the maximum heat flux in the nucleate boiling regime were similar at each position, although the liquid jet velocity was approximately 2.5 times different.

Figure 3.15 shows the change in the maximum heat flux q_{max} with the distance from the impingement point. The value of the maximum heat flux decreased with the distance from the impingement point under all conditions because the liquid film temperature increased further downstream from the impingement point. In addition, the maximum heat flux increased with an increase in the mass flow rate because the increase of the liquid temperature was smaller due to the higher heat capacity of the liquid film. From these results, it could be suggested that the WF propagation velocity was determined by the heat removal rate near the WF, leading to the temperature drop, and the effect of the mass flow rate on it was higher than that of the jet velocity, as discussed in section 3.3.1.

3.3.3 Amount of heat removed from plate to liquid film and evaporative fraction

In the present study, the temperature profile in the xy-plane was measured, and the distribution of the surface heat flux in the xy-plane could be estimated by inverse heat conduction analysis. Using the values of the estimated surface heat flux in the xy-plane, the amount of heat removed from the plate to the liquid film and the evaporative fraction of the liquid film were estimated to evaluate the mass fraction of the injected liquid that contributed to the cooling of the test plate. Figure 3.16 shows the liquid film and the surface heat flux distribution at $t = 0.6$ s under the condition of $\dot{m} = 5.0$ g/s and $d = 0.7$ mm. The amount of heat removed from the plate to the test liquid $\dot{Q}$ was calculated for the area where the value of the estimated surface heat flux was positive according to the following equation.

$$\dot{Q} = \iint q_s dx dy. \tag{3.5}$$

Figure 3.17 shows the amount of heat removed from the plate at the elapsed time when the WF reached close to $x = 30$ mm under each mass flow rate condition; $\dot{Q}$ of $\dot{m} = 3.0, 4.0, 5.0,$ and 6.0 g/s corresponded to the value at $t = 1.2, 0.8, 0.6,$ and 0.4 s, respectively (see Fig. 3.8). The liquid film removed more heat from the test plate as the mass flow rate increased for each nozzle diameter because the maximum heat flux assumed a higher value with an increase in the mass flow rate, as shown in Fig. 3.15. An additional reason was that the wetted area increased with an increase of the mass flow rate as discussed in Chapter 2. Comparing the values under the same mass flow rate conditions, the smaller the nozzle diameter, the higher the amount of heat removed from the plate because the maximum heat flux was slightly higher for smaller diameters. In addition, the amount of heat removed from the plate by single-phase forced convection was greater for the smaller diameter owing to the higher velocity of the liquid film as shown in Fig. 3.14.

Next, the mass fraction of the injected liquid that contributed to the cooling of the test plate was evaluated. To evaluate the fraction, the evaporative fraction $\emptyset$ defined in Eq. (3.6) was used.

$$\emptyset = \frac{\dot{Q}}{\dot{m} h_{lv}}. \tag{3.6}$$

h_{lv} denotes the latent heat of the test liquid. Figure 3.18 shows the evaporative fraction

calculated using Eq. (3.6) for the results shown in Fig. 3.17. The fraction of the injected liquid contributing to the cooling of the plate was nearly 10 % in the case of d = 0.7 mm and 8 % in the case of d = 1.1 mm (possibly overestimated due to effect of neglecting the sensible heat) and was almost the same under each mass flow rate condition, while the amount of heat removed from the plate increased with an increase in the mass flow rate. Figure 3.18 suggests that nearly 90 % or more of the injected liquid was splashed away from the WF without evaporation.

3.4 Conclusions

An experimental study on the jet impingement cooling of a heated wall with a spatial temperature gradient was conducted to investigate the effect of the mass flow rate and the liquid jet velocity on the cooling processes, using a liquid film with an oblique impingement jet, by varying the nozzle diameter. Water and aluminum alloy were used as the test liquid and plate, respectively. The behavior of the liquid film on the heated wall was visualized using high-speed imaging. In addition, the temperature distribution of the surface opposite the cooling surface was obtained using infrared images to estimate the surface temperature and heat flux of the cooled side by solving the inverse problem of three-dimensional transient heat conduction.

The WF gradually moved downstream, and the velocity of the WF decreased as it moved downstream. It was notable that the WF propagation was affected by the liquid mass flow rate and not by the liquid jet velocity being related to the liquid film velocity even though, in this study, the velocity of the liquid jet was different approximately 2.5 times, and the WF moved faster as the mass flow rate increased. The WF position was well-fitted by a power function of elapsed time, and the constant had a linear relationship with the mass flow rate, while the exponent was in the range of approximately 0.4 – 0.5 which agreed with the results reported in the previous studies on quenching, with a vertical impingement jet.

The heat transfer characteristics during the quenching process were examined. The temperature at the relatively upstream location dropped immediately after the WF reached the respective position, while the temperature at the positions further downstream decreased before the arrival of the WF because of the effect of the precursory cooling induced by the solid heat conduction between the wetted and dry regions. The maximum heat flux decreased as the WF moved downstream, and the attained value was almost the same under the same mass flow rate conditions for the same positions, although the nozzle diameter was changed and the velocity of the liquid jet and formed film was different.

50

The amount of heat removed from the test plate to the liquid film was calculated, and the fraction of the injected liquid contributing to the cooling of the test plate was estimated. For evaluating the fraction, the evaporative fraction was defined as the ratio of the amount of heat removed from the metal plate to the product of the mass flow rate and the latent heat of the liquid in this chapter. The amount of heat removed from the plate increased as the mass flow rate increased for each nozzle diameter, and it assumed a higher value upon using a nozzle with a smaller diameter. However, the evaporative fraction assumed almost the same value for each nozzle diameter and was nearly 10% or less. These results suggest that nearly 90% or more of the injected liquid was splashed away from the test plate without evaporation.

References

[1] C. F. Gomez, C. W. M. van der Geld, J. G. M. Kuerten, M. Bsibsi, and B. P. M. van Esch, "Film boiling in quench cooling with high-temperature jets," *International Journal of Heat and Mass Transfer*, vol. 164, Article 120578, 2021.

[2] S. G. Lee, M. Kaviany, C. J. Kim, and J. Lee, "Quasi-steady front in quench subcooled-jet impingement boiling: Experiment and analysis," *International Journal of Heat and Mass Transfer*, vol. 113, pp. 622-634, 2017.

[3] A. V. S. Oliveira, D. Marechal, J. -L. Borean, V. Schick, J. Teixeira, S. Denis, and M. Gradeck, "Experimental study of the heat transfer of single-jet impingement cooling onto a large heated plate near industrial conditions," *International Journal of Heat and Mass Transfer*, vol. 184, Article 121998, 2022.

[4] D. H. Wolf, F. R. Incropera, and R. Viskanta, "Local jet impingement boiling heat transfer," *International Journal of Heat and Mass Transfer*, vol. 39, no. 7, pp. 1395-1406, 1996.

[5] T. Okawa, K. Yamagata, and Y. Umehara, "Measurement of heat transfer coefficient profile during quenching of a vertical hot wall with a falling liquid film," *Nuclear Engineering and Design*, vol. 363, Article 110629, 2020.

[6] G. Fujii, Y. Daimon, C. Inoue, D. Shiraiwa, N. Tanaka, and K. Furukawa, "Visualization of pulse firing mode in hypergolic bipropellant thruster," *Journal of Propulsion and Power*, vol. 36, no. 5, pp. 671-684, 2020.

[7] L. jun Yang, P. hui Li, and Q. fei Fu, "Liquid sheet formed by a Newtonian jet obliquely impinging on pro/hydrophobic surfaces," *International Journal of Multiphase Flow*, vol. 125, Article 103192, 2020.

[8] M. Monde, "Heat Transfer Characteristics during Quench of High Temperature

Solid," *Journal of Thermal Science and Technology*, vol. 3, no. 2, pp. 292-308, 2008.

[9] C. Agrawal, R. Kumar, A. Gupta, and B. Chatterjee, "Rewetting and maximum surface heat flux during quenching of hot surface by round water jet impingement," *International Journal of Heat and Mass Transfer*, vol. 55, pp. 4772-4782, 2008.

[10] Y. Liu, H. Nakai, Y. Mitsutake, and M. Monde, "Experimental study on transient boiling heat transfer around wetting front during subcooled jet impingement quenching," *Thermal Science and Engineering*, vol. 29, no. 1. pp. 9-17, 2021.

[11] A. H. Nobari, V. Prodanovic, and M. Militzer, "Heat transfer of a stationary steel plate during water jet impingement cooling," *International Journal of Heat and Mass Transfer*, vol. 101, pp. 1138-1150, 2016.

[12] R. K. Bhagat, N. K. Jha, P. F. Linden, and D. I. Wilson, "On the origin of the circular hydraulic jump in a thin liquid film," *Journal of Fluid Mechanics*, vol. 851, p. R5, 2018.

[13] T. Inamura, H. Yanaoka, and T. Tomoda, "Prediction of Mean Droplet Size of Sprays Issued from Wall Impingement Injector," *AIAA Journal*, vol. 42, no. 3, pp. 614–621, 2004.

[14] R. K. Bhagat and D. I. Wilson, "Flow in the thin film created by a coherent turbulent water jet impinging on a vertical wall," *Chemical Engineering Science*, vol. 152, pp. 606-623, 2016.

[15] B. Wang, D. Lin, Q. Xie, Z. Wang, and G. Wang, "Heat transfer characteristics during jet impingement on a high-temperature plate surface," *Applied Thermal Engineering*, vol. 100, pp. 902-910, 2016.

[16] Y. Mitsutake and M. Monde, "Heat transfer during transient cooling of high temperature surface with an impinging jet," *Heat and Mass Transfer/Waerme- und Stoffuebertragung*, vol. 37, no. 4-5, pp. 321-328, 2001.

[17] N. Karwa and P. Stephan, "Experimental investigation of free-surface jet impingement quenching process," *International Journal of Heat and Mass Transfer*, vol. 64, pp. 1118-1126, 2013.

[18] A. Bejan and A. D. Kraus, Heat transfer handbook, vol. 1, *John Wiley & Sons*, 2003.

[19] H. Fujimoto, K. Tatebe, Y. Shiramasa, T. Hama, and H. Takuda, "Heat Transfer Characteristics of a Circular Water Jet Impinging on a Moving Hot Solid," *ISIJ International*, vol. 54, no. 6, pp. 1338-1345, 2014.

[20] Y. Haramura, "Inverse Heat Conduction Solution Utilizing the Difference Method with an Exact Matching Rule," *Thermal science and engineering*, vol. 29, no. 2. pp. 33-43, 2021.

[21] S.V.Patankar, "Numerical heat transfer and fluid flow (1st ed.)," *CRC Press*, 1980.

[22] M. J. E. Savitzky, A.; Golay, "Smoothing and Differentiation of Data by Simplified Least Squares Procedures," *Analytical Chemistry*, vol. 36, no. 8, pp. 1627-1639, 1964.

[23] https://pypi.org/project/csaps/

[24] N. Karwa, T. Gambaryan-Roisman, P. Stephan, and C. Tropea, "Experimental investigation of circular free-surface jet impingement quenching: Transient hydrodynamics and heat transfer," *Experimental Thermal and Fluid Science*, vol. 35, no. 7, pp. 1435-1443, 2011.

[25] N. Hatta, J. Kokado, K. Hanasaki, "Numerical Analysis of Cooling Characteristics for Water Bar," *Transactions of the Iron and Steel Institute of Japan*, vol. 23, no. 7, pp. 555-564, 1983.

[26] J. Hammad, Y. Mitsutake, and M. Monde, "Movement of maximum heat flux and wetting front during quenching of hot cylindrical block," *International Journal of Thermal Sciences*, vol. 43, no. 8 SPEC. ISS., pp. 743-752, 2004.

[27] Y. Daimon, H. Negishi, H. Tani, Y. Matsuura, S. Iihara, and S. Takata, "Flow field and heat transfer analysis in a MON/MMH bipropellant rocket engine," *International Journal of Energetic Materials and Chemical Propulsion*, vol. 16, no. 3, pp. 263-280, 2017.

[28] C. Agrawal, "Surface Quenching by Jet Impingement − A Review," *Steel Research International*, vol. 90, no. 1, pp. 1-22, 2019.

[29] C. L. Tien and L. S. Yao, "Analysis of Conduction-Controlled Rewetting of a Vertical Surface," *Journal of Heat Transfer*, vol. 97, no. 2, pp. 161-165, 1975.

[30] K. H. Sun, G. E. Dix, and C. L. Tien, "Effect of Precursory Cooling on Falling-Film Rewetting," *Journal of Heat Transfer*, vol. 97, no. 3, pp. 360-365, 1975.
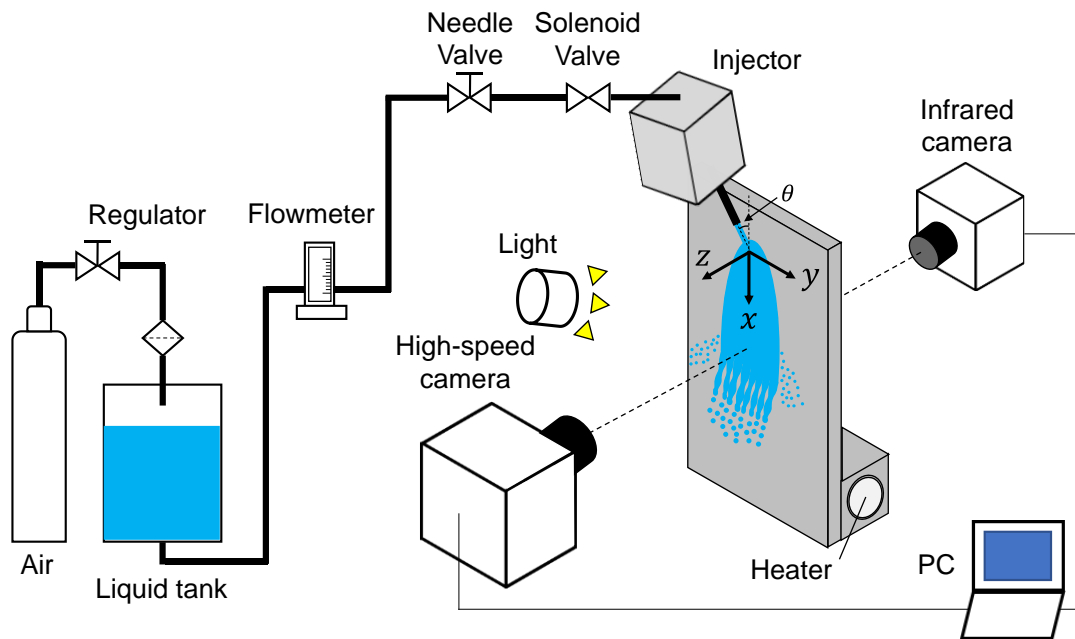
Fig. 3.1 Schematic of the experimental apparatus

(a)

(b)
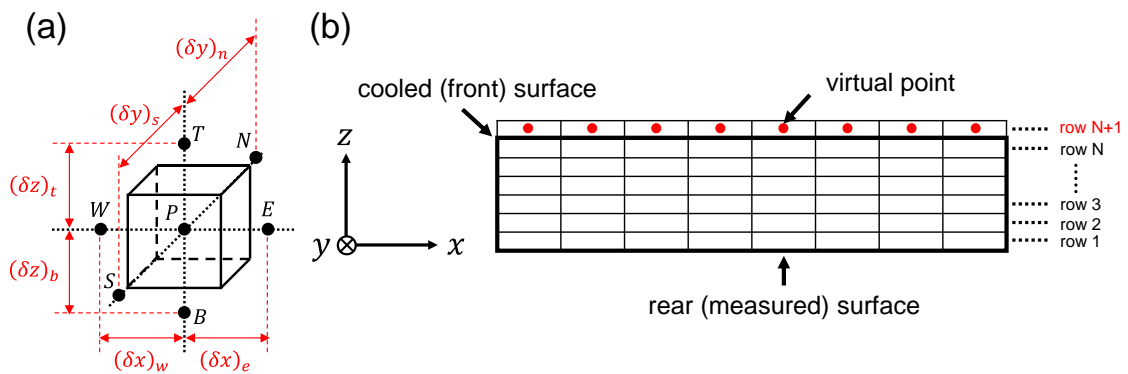
Fig. 3.2 Schematics of control volume P (a) and calculation domain (b).
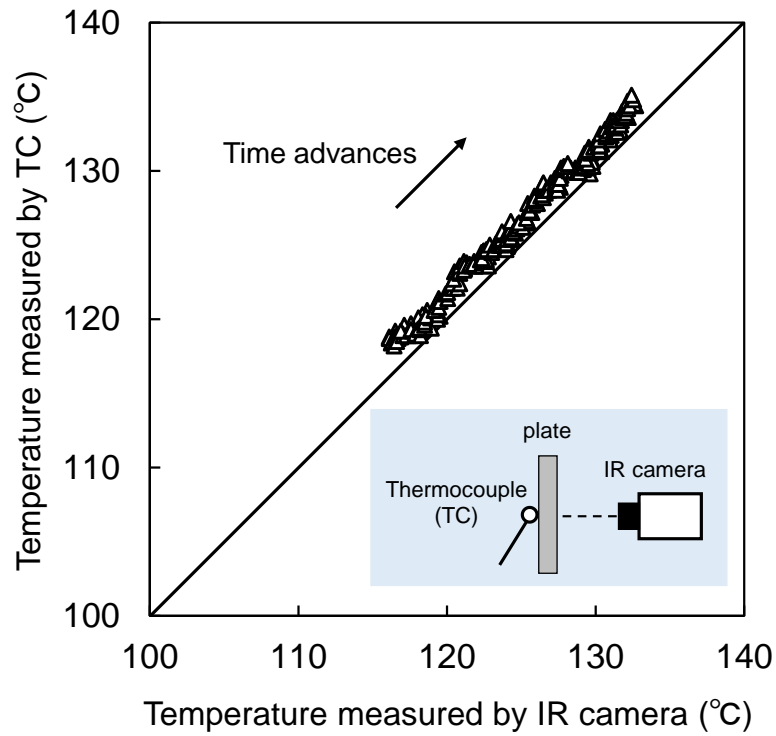
Fig. 3.3 Temperature difference between front surface and rear surface during plate heating

(Ⅰ)：Cubic smoothing spline for spatial temperature distribution at each time
(Ⅱ)：Savitzky-Golay filtering for temperature change at each point
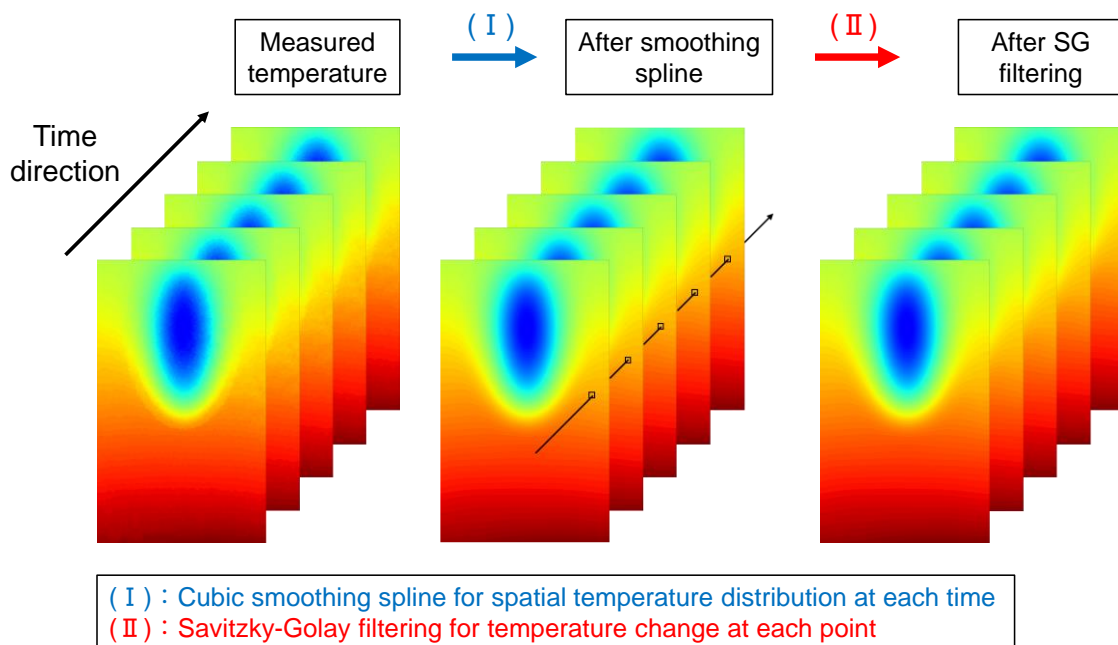
Fig. 3.4 Smoothing procedures of measured temperature profile for solving inverse heat conduction problem
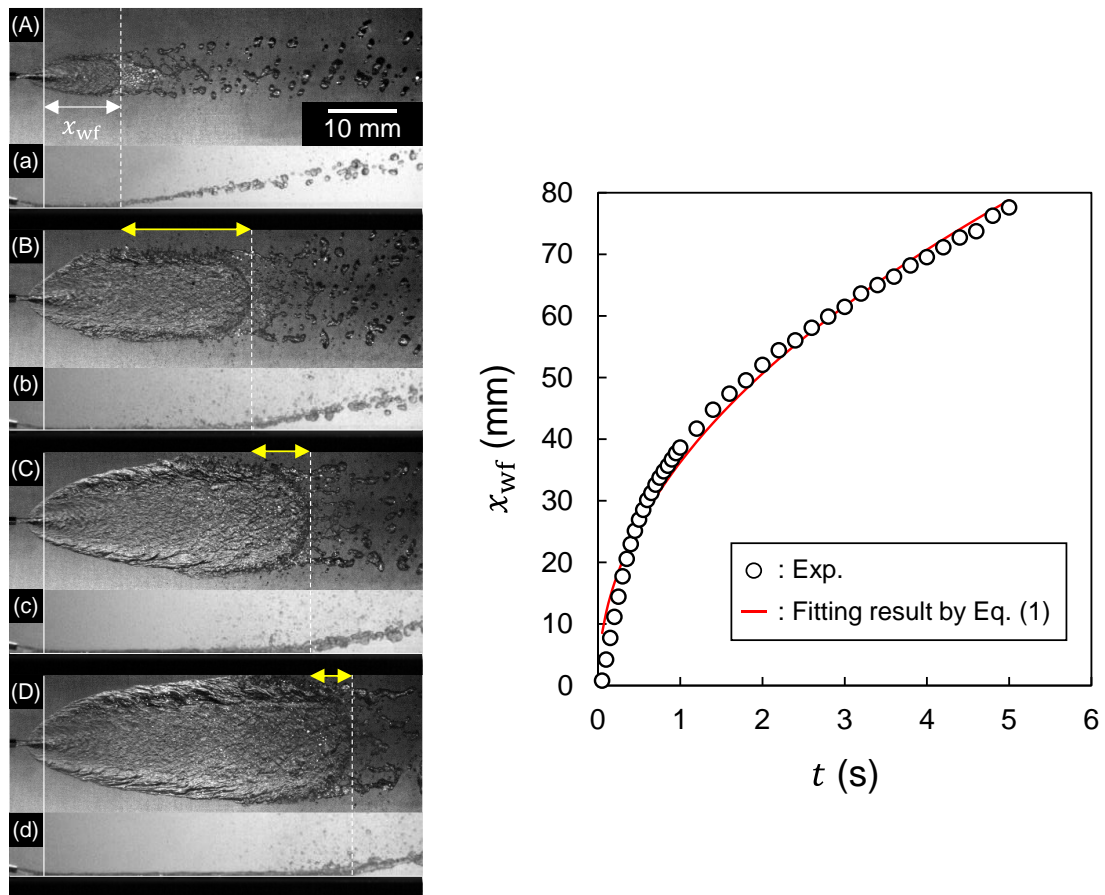
Fig. 3.5 Direct images of liquid film at each elapsed time under the condition of $d = 0.7$ mm and $\dot{m} = 5.0$ g/s (left) and WF position with elapsed time (right). The images of the capital letters and the small letters respectively show the front views and the side views. (A, a): $t = 0.2$ s, (B, b): $t = 0.6$ s, (C, c): $t = 1.0$ s, (D, d): $t = 1.4$ s
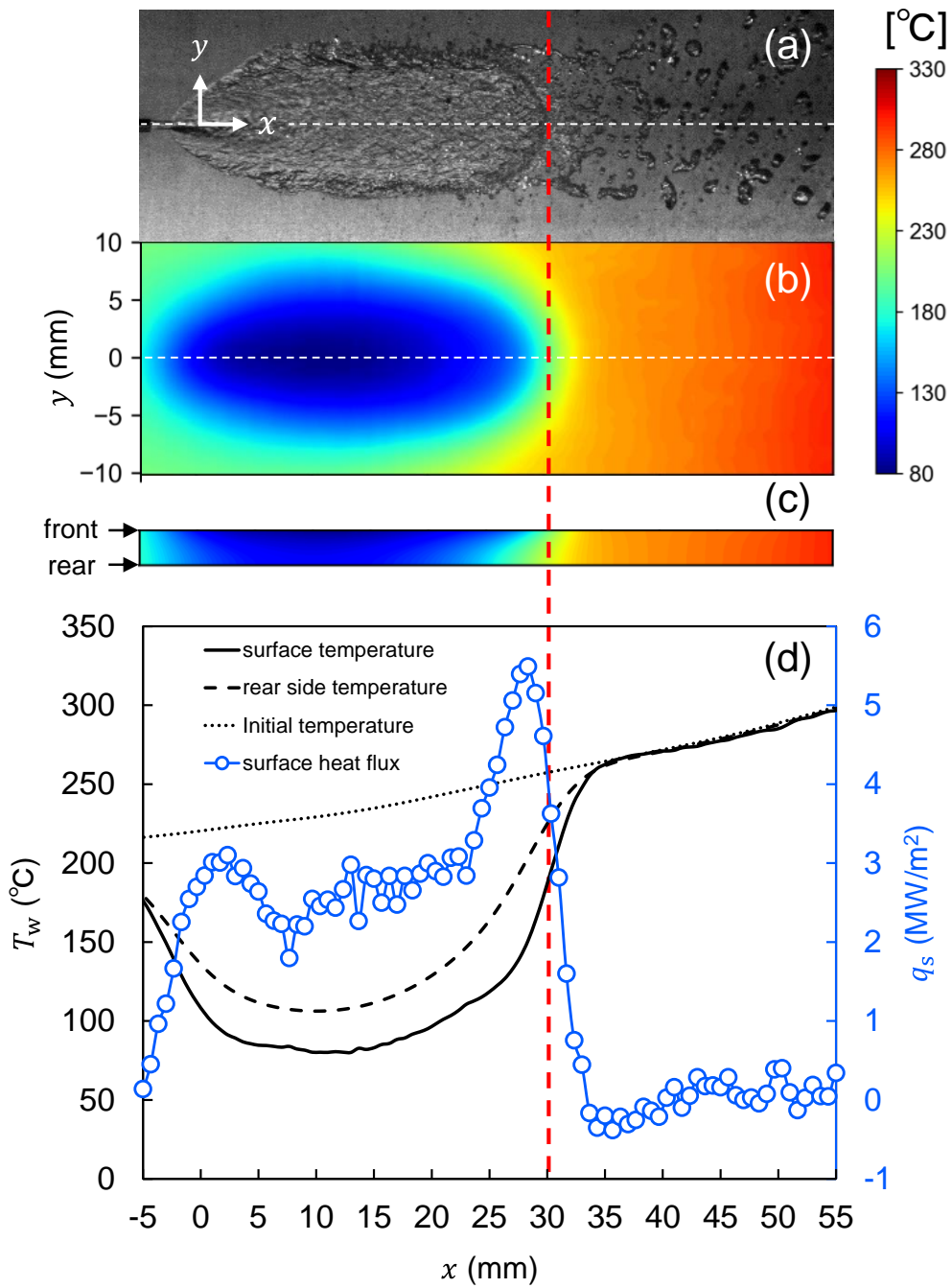
Fig. 3.6 Direct image of the liquid film (a), thermal images of temperature distribution of the front surface (b) and in the xz-plane for $y = 0$ (c), and estimated surface temperature and heat flux distribution along the x-axis for $y = 0$ calculated at the elapsed time of 0.6 s (d). Red broken line indicates the WF position
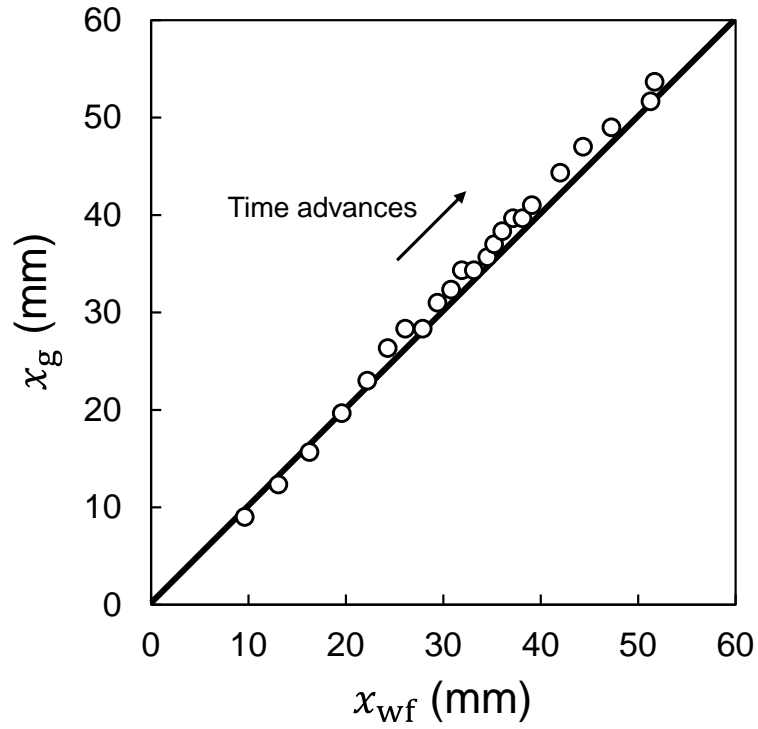
Fig. 3.7 Relationship between WF position and position where spatial temperature gradient takes its maximum value on the x-axis
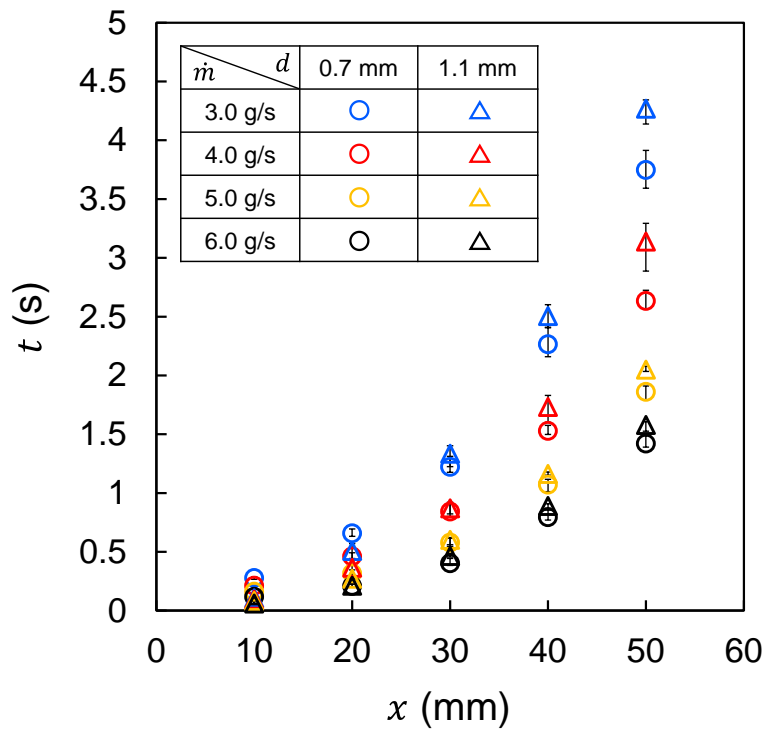
Fig. 3.8 Elapsed time when WF reaches certain positions on the x-axis
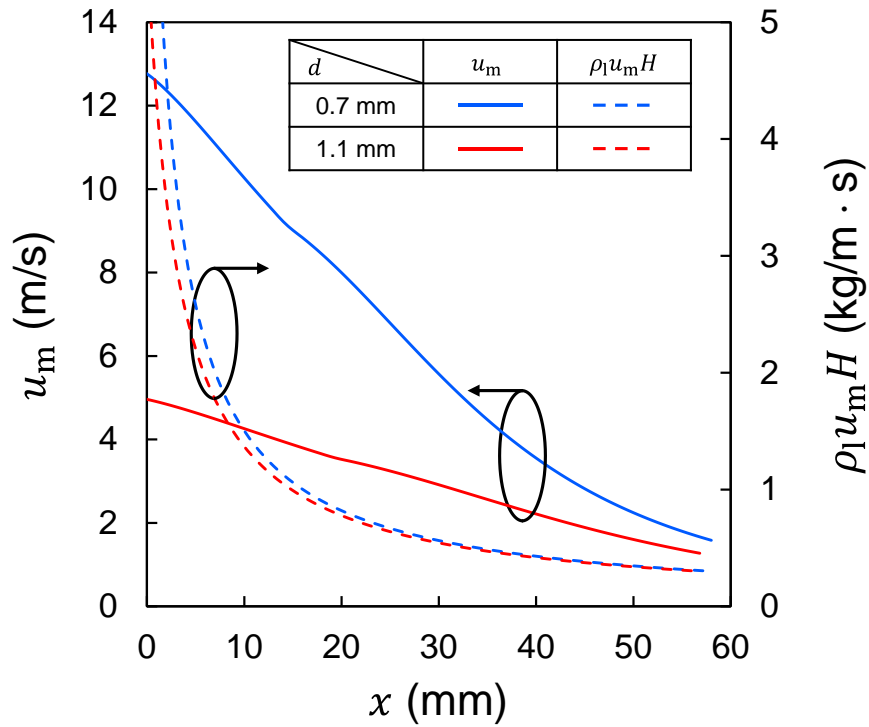
Fig. 3.9 Mean velocity of liquid film and film mass flow rate per unit liquid film width on the x axis under the condition of $\dot{m}$ = 5.0 g/s predicted by the model in [].
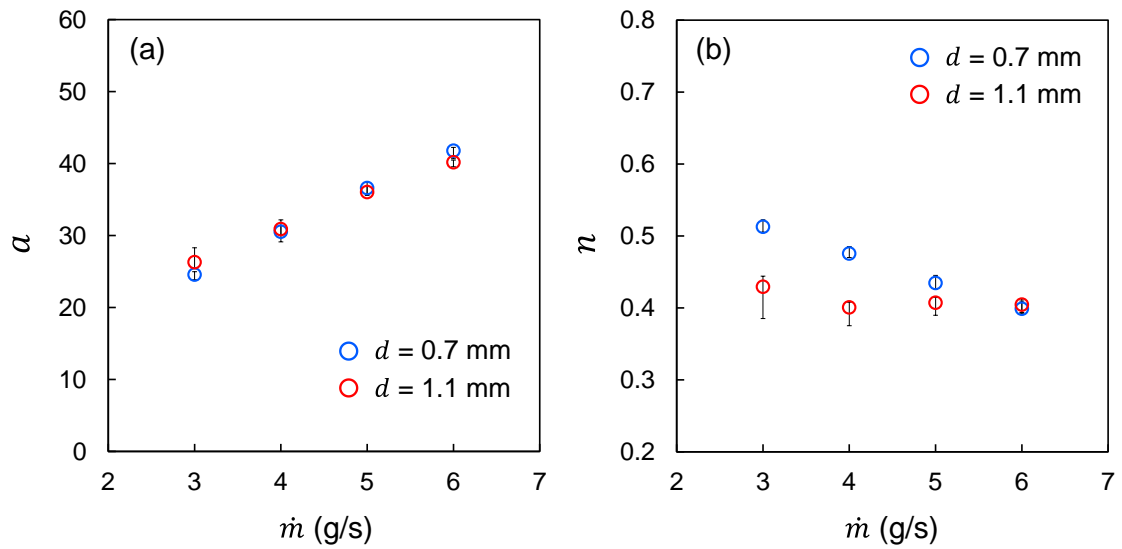
Fig. 3.10 Effects of mass flow rate and jet velocity on constant a (a) and exponent n (b)
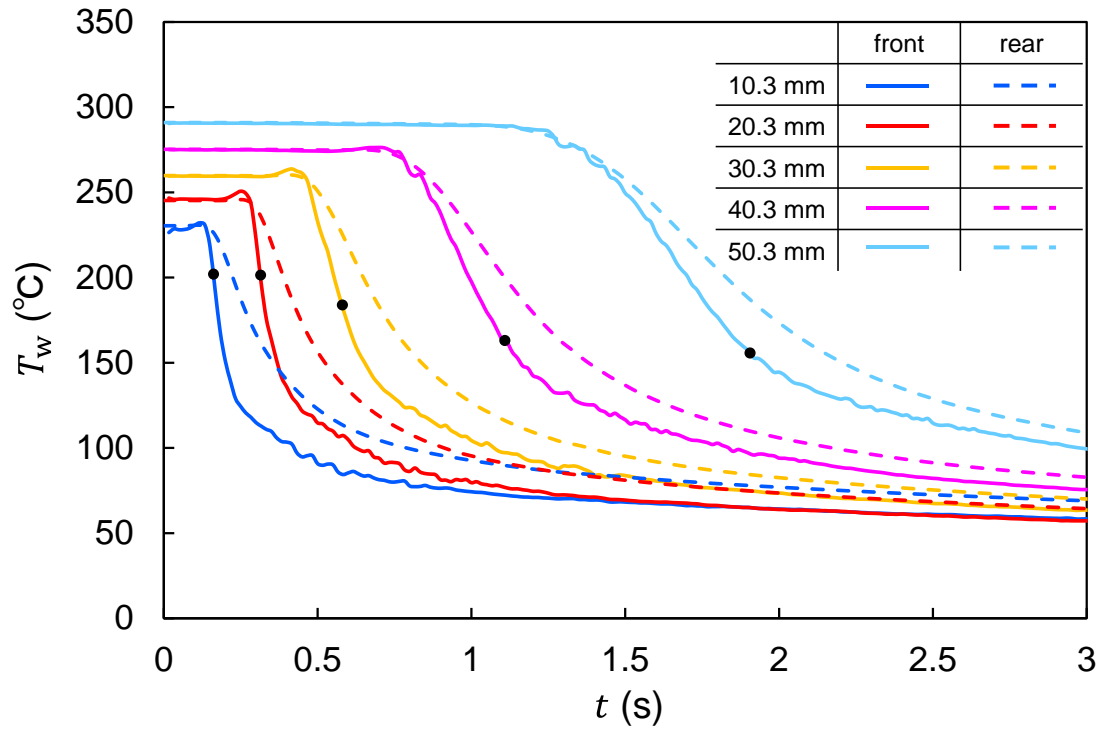
Fig. 3.11 Temperature history at each position on the x-axis under the condition of d = 0.7 mm and $\dot{m}$ = 5.0 g/s. The black dots indicate the temperature at the moment when the WF reached each position
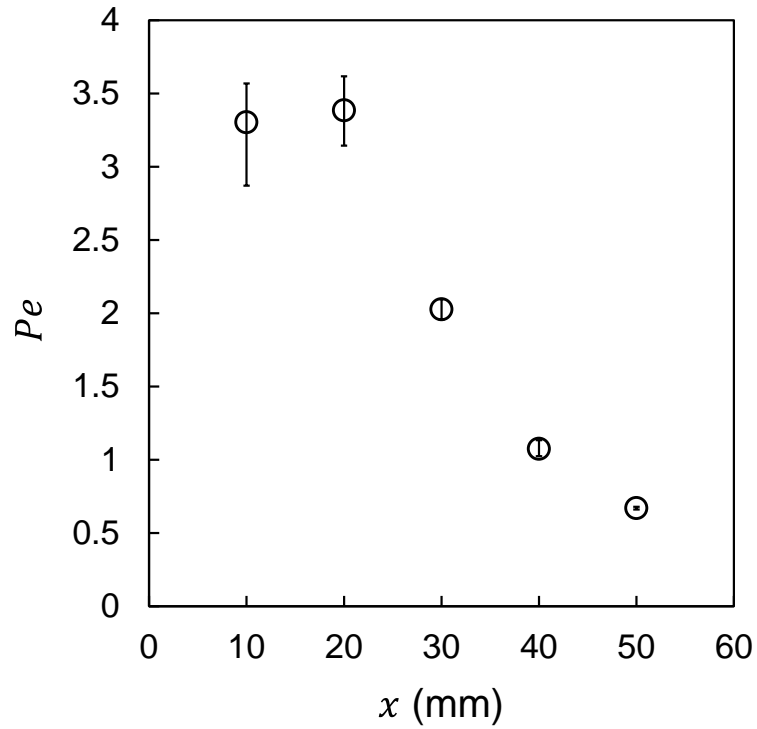
Fig. 3.12 Change in Peclet number under the condition of $d = 0.7$ mm and $\dot{m} = 5.0$ g/s
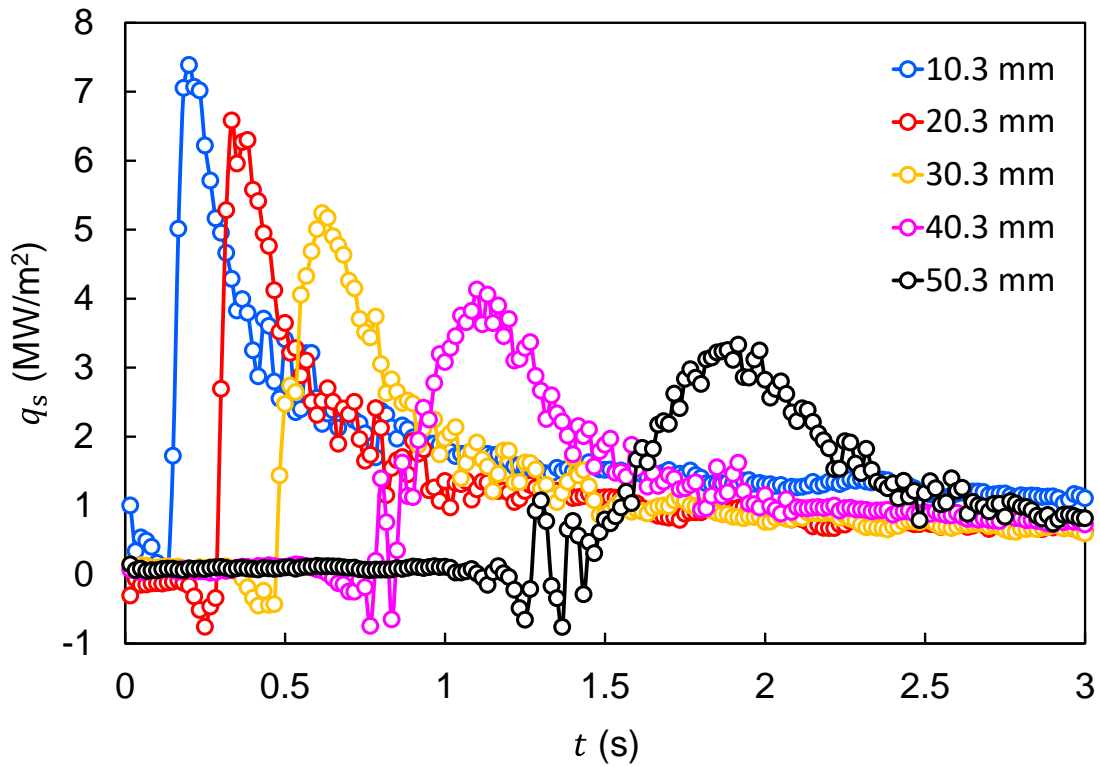
Fig. 3.13 Time history of heat flux at each position on the x-axis under the condition of $d = 0.7$ mm and $\dot{m} = 5.0$ g/s
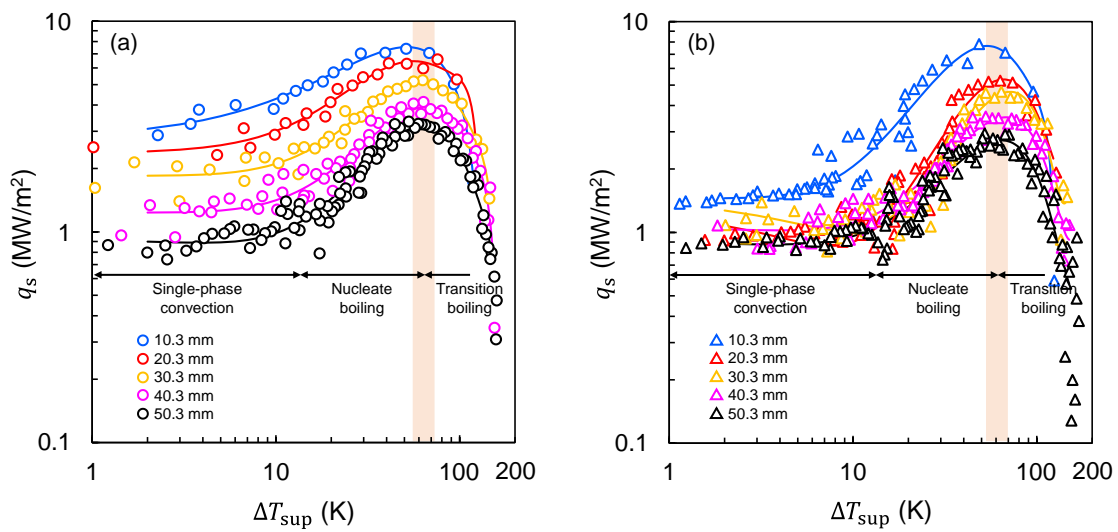
Fig. 3.14 Boiling curves at each position on the x-axis under the condition of $d = 0.7$ mm (a) and $d = 1.1$ mm (b) for $\dot{m} = 5.0$ g/s
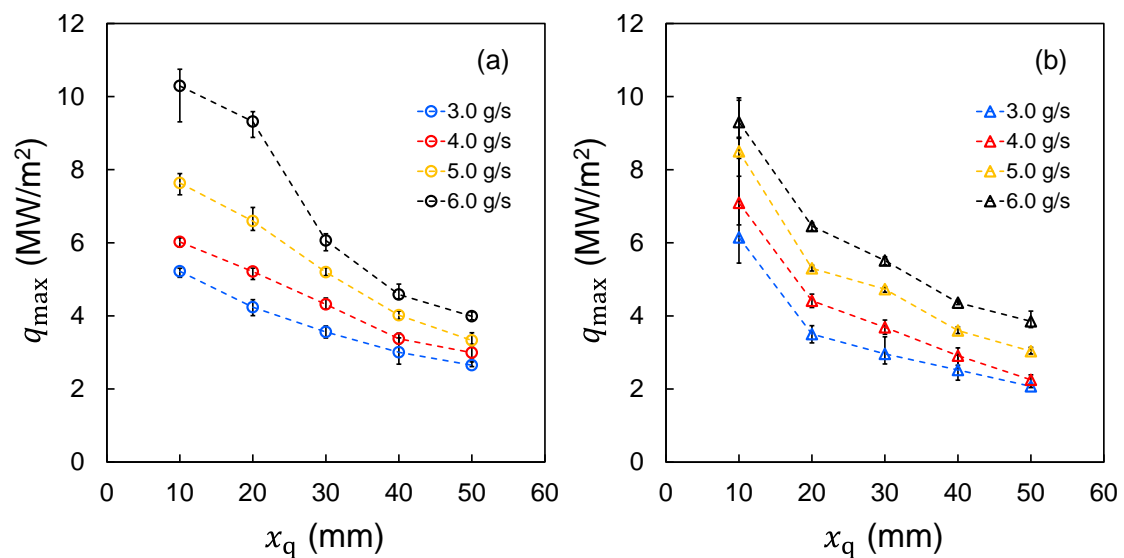
Fig. 3.15 History of maximum heat flux at each position on the x-axis under the condition of $d = 0.7$ mm (a) and $d = 1.1$ mm (b)
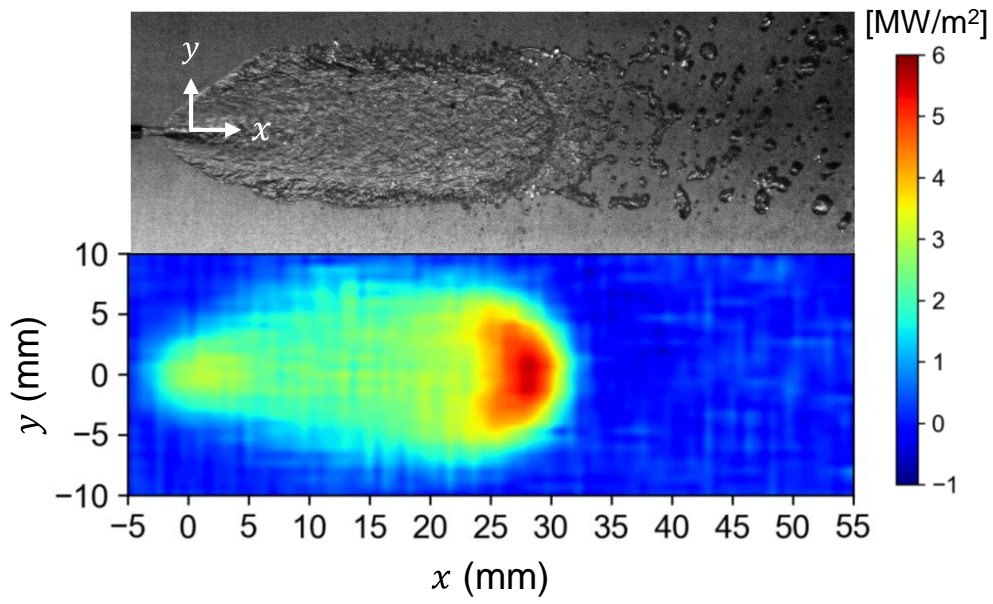
Fig. 3.16 Direct image of liquid film and distribution of heat flux at $t = 0.6$ s under the condition of $d = 0.7$ mm and $\dot{m} = 5.0$ g/s
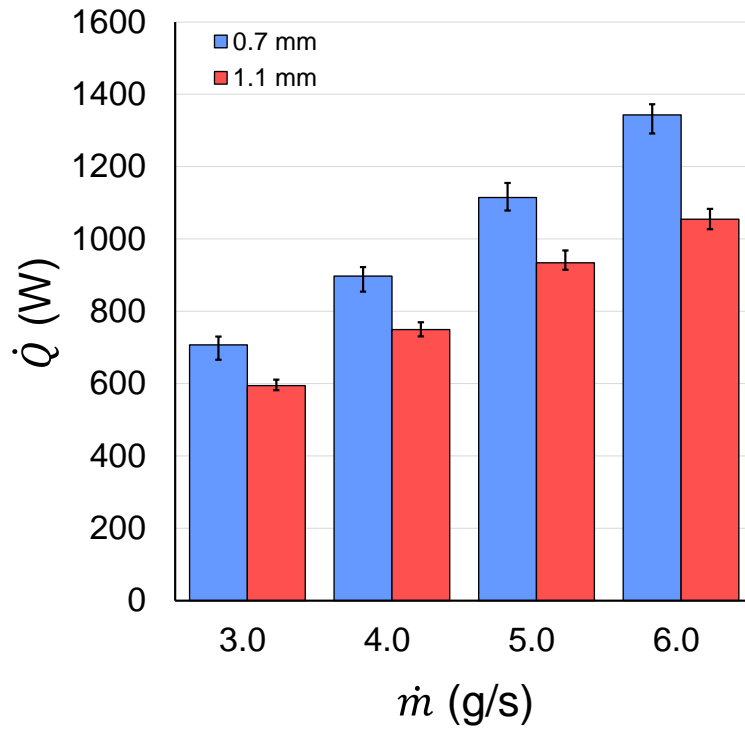
Fig. 3.17 Amount of heat removed from test plate to liquid film at an elapsed time when the WF reached close to $x = 30$ mm
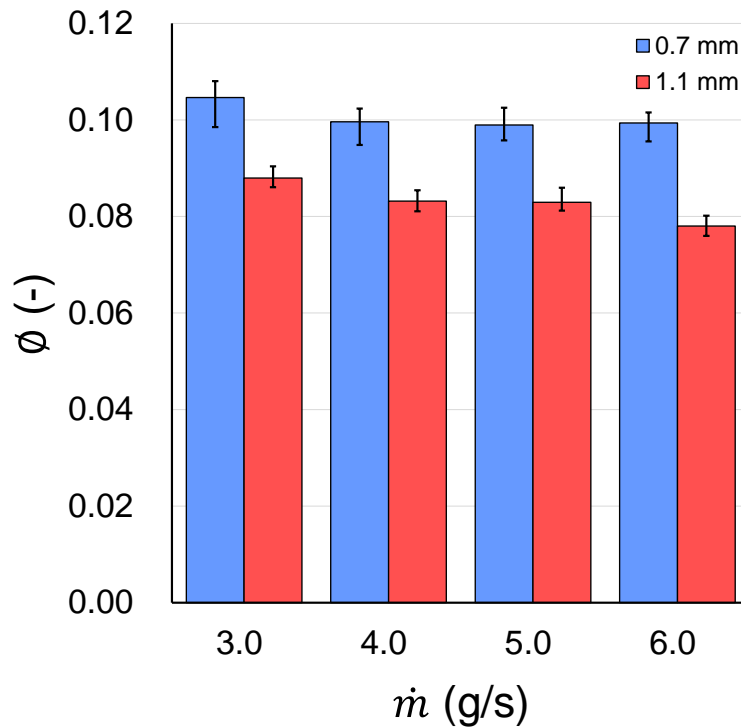
Fig. 3.18 Evaporative fractions at an elapsed time when the WF reached close to $x = 30$ mm

Table 3.1 Experimental conditions

Mass flow rate of test liquid	[g/s]	3.0, 4.0, 5.0, 6.0
Nozzle diameter	[mm]	0.7, 1.1
Jet Reynolds number	[-]	5400, 7200, 9100, 10900 (d = 0.7 mm)
		3500, 4600, 5800, 6900 (d = 1.1 mm)
Impingement angle	[°]	10
Degree of subcooling	[K]	80

Chapter 4 Liquid film and heat transfer characteristics during cooling of a superheated wall through pulsed injection

4.1 Introduction

Pulse firing is one of the major operation modes of bipropellant thrusters for the attitude control of small-scale spacecraft. During the operation of the pulse firing mode, the situation that the fuel jets for film cooling are injected onto the hot surface owing to heat soak-back [1] can appear depending on the conditions of the interval between each pulsed-combustion event. The combustion chamber wall cannot be cooled sufficiently according to the interval and associated heat soak-back conditions. The operational range of the pulse firing mode is determined by the requirements of the cooling performance (i.e., the heat resistance of the thrusters). For better thermal management and a wider operational range of the thrusters, the cooling processes of the hot surface by the liquid jet impingement need to be understood.

Whereas the heat transfer characteristics using continuous liquid jet injection were investigated intensively as introduced in section 1.4.2, the cooling process with intermittently injected liquid jets, which is found in the pulse firing mode of bipropellant thrusters, has not been well understood yet. Recently, Wessenberg et al. [2] investigated the heat transfer efficiency of the pulsed injection of the water jets during the single-phase convection cooling mode. Abishek and Narayanaswamy [3] investigated the effects of the pulsed injection on the boiling heat transfer characteristics such as the heat flux in the nucleate boiling region and the critical heat flux (CHF) by using water and FC72 as the coolant. However, the effects of the pulsed injection of the liquid jet on the heat transfer characteristics has not been well investigated [2], and the researches on the two-phase cooling by the pulsed injection of the liquid jet were very limited [4].

Few studies have also examined the transient formation processes of the liquid film during pulse firing mode in actual bipropellant thrusters. Fujii et al. [5] succeeded for the first time in optically capturing the unsteady liquid film dynamics during the operation of the pulse firing mode by using a quartz glass chamber, while they confirmed that the liquid film length in a glass chamber was longer than that in an actual combustion chamber owing to the lower heat input from the chamber wall. To recognize the difference in the liquid film behavior on both types of chamber walls, the unsteady dynamics of the liquid film on an actual chamber wall also need to be investigated. However, the direct

optical observation of the physical phenomena inside the chamber wall of actual bipropellant thrusters is impractical because actual combustion chambers are generally made of niobium alloy [6], ceramic [7], or precious metals [8]. For a better understanding of the liquid film behavior, it can be quite beneficial if the liquid film behavior inside the chamber could be captured by only measuring the temperature distribution of the outer surface of the chamber wall. Liquid film length at a steady state in an actual chamber is determined from the temperature distribution on the outer surface of the chamber measured by an infrared camera [9], and an infrared imaging method with a high spatial resolution has the potential to give valuable information about the heat transfer characteristics between the liquid film and chamber wall [10].

In the present chapter, therefore, the transient cooling tests of the hot metal plate surface by the pulsed injection of the liquid jet conducted to gain the insight into the liquid film behavior during the pulsed cooling. Since the temperature measured in the opposite side of the cooled surface had proved to represent the cooling process in chapter 3, these measurement techniques were applied on the liquid film behavior during the pulse cooling. Then, the pulse cooling tests with the same amount of the liquid but with different flow rates and duty cycle (DC; the ratio of the injection duration to one period) were examined because the cooling performance is considered to be governed by the balance between the amount of cooling during injection duration and the temperature rise of the metal plate during injection stop period. The continuous cooling test with the time-averaged flow rate of the pulsed cooling tests was also conducted as for the control condition. Additionally, the thermal properties of the metal plate affect the temperature rise of the metal plate, and that eventually influences the heat transfer characteristics of the liquid film. In the present study, therefore, two different metal plates were employed to evaluate the effect of the thermal properties (i.e.; thermal diffusivity or thermal inertia) of the metal plate.

4.2 Experimental description

Figure 4.1 shows a schematic illustration of the experimental setup used in the present study for simultaneous measurement of the liquid film behavior and the temperature distribution. In the present study, the coordinates were defined as shown in the metal plate of Fig. 4.1, and the origin was set to the impingement point of the liquid jet. In this setup, a liquid jet was intermittently injected from the liquid tank pressurized by the compressed air. The opening and closing timing of the solenoid valve were controlled using signals from function generator (NF corporation, WF1948). A rod heater was inserted into the downstream part of the metal plate for heating the metal plate as shown in Fig. 3.1. The

rod heater was utilized to make the situation that the liquid film flows against the direction of the heat input (i.e.; from downstream to upstream) as is the heat flow direction inside the chamber wall of the bipropellant thrusters. In the present study, a liquid film behavior was mainly observed from the side with the backlight technique by using a high-speed camera (Photron FAST-CAM SA-1.1) to capture the wetting front position clearly. Additionally, high-speed imaging from the front (cooled) side was also conducted as in chapter 3. The frame rate and exposure time were 500 fps and 20 μs. The spatial resolution for the side and the front view was 0.16 mm/pixel and 0.09 mm/pixel, respectively. The temperature distribution of the rear surface of the metal plate was measured by an infra-red camera (NIPPON AVIONICS InfReC R550Pro). The frame rate and spatial resolution for the temperature measurement were 60 fps and 0.22 mm/pixel. The rear side of the metal plate was painted with blackbody spray for ensuring an emissivity of 0.94. For investigating the effects of the thermal properties of the metal plate on the pulsed cooling, aluminum alloy (A5052) and copper (C1100) were employed as the test plate with a thickness of 3 mm, a width of 50 mm, and a length of a straight part of 80 mm. The values of the thermal properties of each metal are listed in Table 4.1. The temperature measurement area was restricted with a length of 70 mm and a width of 46 mm. In the present study, the oxidization of the metal surface unavoidably occurred, and the oxide layer on the surface affects the cooling process [11]. Therefore, the metal surface was fully oxide by heating and the cooling tests were conducted several times before the data acquisition to ensure the stable surface properties and reproducibility.

For the test liquid, water was employed as was in chapter 3. The nozzle diameter d (i.e.; liquid jet diameter) and the impingement angle θ were fixed at 1.1 mm and 10°, respectively. The ratio of the distance between the nozzle outlet and the test plate (i.e.; liquid jet length) to the nozzle diameter L/d was set to 6. The test liquid (approximately 20°C) was injected onto the test plate when the temperature of the impingement point was raised to 220°C. For raising the metal temperature, the temperature of the rod heater was set to 600°C and 500°C in the case of aluminum alloy and copper plate respectively to match the temperature of the impingement point to 220°C while forming a stable initial temperature distribution. The initial temperature distribution on the x-axis is shown in Fig. 4.2. For the conditions of the pulsed injection, the pulse frequency f_{p} was set to 1.0 Hz, which corresponded to the pulse period τ_{p} ($=1/f_{\mathrm{p}}$) = 1.0 s. The number of pulses was fixed three. The flow rate of the test liquid and the duty cycle were varied while the total injection quantity of the test liquid was kept constant in each pulse period. Additionally, the continuous injection test with the time-averaged flow rate of the pulsed cooling test was also conducted to compare the total removed heat by the liquid film of

the pulsed and continuous cooling tests. The pulsed injection conditions were summarized in Table 4.2. For each condition, the cooling tests were conducted five times.

To evaluate the heat transfer characteristics between the liquid film and the metal surface, the temperature and heat flux on the front (cooled) surface need to be estimated. For the estimation, the inverse heat conduction problem was solved in the same way as in Chapter 3. Detailed information about the inverse heat conduction problem and the data reduction are described in section 3.2.2. A rectangular computation domain with a width of 46 mm, a length of 70 mm (measurement area), and a thickness of 3 mm were divided into 69×105×3 cells. The treatment of the initial and boundary conditions was the same as that in section 3.2.2. The temperature dependence of the thermal properties was not considered in this chapter.

4.3 Results and discussion

This section first provides an overview of the liquid film behavior and heat transfer characteristics between the liquid film and the metal surface in the pulsed cooling test. Next, the liquid film behavior and the removed heat by the liquid film in the pulsed and continuous cooling tests are compared. In the following, each injection and non-injection period is defined as "N^{th} ON time" and "N^{th} OFF time", respectively. For example, 1st ON time and 1st OFF time under the condition of f_{p} = 1.0 Hz and 50% DC correspond to the periods of t = 0 s ~ 0.5 s and t = 0.5 s ~ 1.0 s, although there are both open and close response time of the solenoid valve to be exact. Additionally, "N^{th} period" indicates the period of t = $(N-1) \cdot \tau_{\text{p}}$ s - $N \cdot \tau_{\text{p}}$ s.

4.3.1 Liquid film behavior and heat transfer characteristics during pulse cooling

In this section, the result for the aluminum alloy under the condition of 50% DC was used as the representative data to explain the liquid film behavior and heat transfer characteristics during the pulsed cooling. Figure 4.3 shows the direct image of the liquid film taken from the front and the distributions of the estimated temperature and heat flux on the front surface at the elapsed time of 0.5 s, corresponding to the end of injection for the 1st period. During the 1st ON time, the wetting front gradually propagated downstream from the start of injection and eventually reached the position shown in Fig. 4.3. In the present study, the distance from the impingement point to the wetting front on the x-axis was defined as x_{wf} as shown in Fig. 4.3. The maximum heat flux was achieved in the

wetted area of the vicinity of the wetting front as shown in section 3.3, while the relatively higher value of the heat flux was observed in the region near the impingement point. These trends of the result during 1st ON time were the same as our previous research for the continuous cooling test in section 3.3.

Figure 4.4 shows the time series of the visualization images and the estimated temperature and heat flux on the front surface during the 1st OFF time. It should be noted that the contour range for the heat flux is different from that in Fig. 4.3. As shown in Fig. 4.4, the residual liquid film was consumed due to evaporation and ejection of the droplet with the rupture of the bubble induced by the nucleate boiling, which is going to be examined in chapter 5 in detail. The nucleate boiling of the residual liquid film occurred in the downstream part because the metal plate was relatively high when the injection of the liquid jet was cut off. The position where the nucleate boiling was observed slightly moved upstream owing to the temperature rise of the metal plate surface, and then, the residual liquid film was fully consumed. The boiling phenomenon of the residual fuel liquid film was also observed during the pulse firing mode in a quartz chamber [5]. The processes of the residual liquid film consumption with the nucleate boiling mentioned above were successfully captured in the results of the surface heat flux distribution estimated by solving the inverse heat conduction problem.

Figure 4.5 shows the cooling processes around the beginning of the 2nd and 3rd periods. The white dashed lines indicate the wetting front position at the end of the previous ON time. For the 2nd period, the liquid film rapidly expanded downstream, and at $t = 1.1$ s, reached the wetting front position at the end of the 1st ON time because the temperature of the metal plate surface did not rise to the initial state of the cooling test during the 1st OFF time as shown in Fig. 4.5. Comparing the 2nd and 3rd periods, it was observed that the liquid film expanded further downstream for the 3rd period in 0.1 s after the start of the third injection because the surface temperature of $t = 2.0$ s was lower than that of $t = 1.0$ s. The surface heat flux immediately after the start of 2nd and 3rd injections indicated a higher value owing to the rapid propagation of the liquid film as shown in $t = 1.05$ and 2.05 s of Fig. 4.5. Subsequently, the value of the surface heat flux decreased especially the region from near the impingement point to the middle of the liquid film because the surface temperature decreased owing to the rapid film propagation, leading to the decrease in the temperature difference between the metal surface and the liquid film. The wetting front rapidly propagated and reached further downstream with each successive injection because the temperature rise of the metal plate during the OFF time did not exceed the degree of the temperature drop in the previous ON time.

To obtain an overview of the liquid film formation and cooling processes during the

pulsed cooling test as indicated thus far, the time history of the wetting front position and the estimated temperature on the front surface at a certain position (x = 30.3 mm) on the x-axis are shown in Fig. 4.6. Results of the continuous cooling test under the same flow rate condition (360 mL/min) are indicated as a dashed line in Fig. 4.6 (a). Additionally, in Fig. 4.6 (b), the time history of the position at which the value of the spatial temperature gradient dT_w/dx on the x-axis took its maximum value x_g was also plotted. The temperature of the metal plate decreased with the number of injections, while its value was higher than that in the continuous cooling test under the same flow rate condition. For the liquid film behavior, the wetting front position of the 2nd and 3rd periods appeared upstream of its position at the previous end of injection owing to the temperature rise during each OFF time and eventually propagated further downstream. In addition, it should be noted that the position of the wetting front corresponding to the position where the value of dT_w/dx achieved its maximum value regardless of the pulse period, as observed in the quenching processes of the continuous injection in chapter 3. The results in this section demonstrated that the liquid film behavior during both the ON and OFF time could be captured by measuring the opposite side temperature of the cooled side and solving the inverse heat conduction problem.

4.3.2 Cooling performance for pulsed cooling

a) Evaluation of wetting front behavior

The wetting front behavior was discussed based on the visualization results. Figure 4.7 shows the wetting front position at the end of each ON time for aluminum alloy and copper plate. The results of continuous cooling at t = 1.0, 2.0, and 3.0 s were also indicated as the gray color bar in Fig. 4.7 for reference. For the 1st period, the wetting front propagated further downstream as DC decreased in both types of metal plates. In the aluminum alloy plate, the position of the wetting front was almost the same for the conditions of from 30% DC to 60% DC and decrease with the increase in DC from 72% to continuous cooling for the 2nd and 3rd periods. On the other hand, the wetting front formed on the copper plate represented approximately the same position in the 2nd period except the condition of 30% DC. Eventually, the position in higher DC conditions (i.e.; conditions close to continuous injection) became the same as the condition of 30% DC. This tendency was considered to be caused by the difference in the temperature rise during the OFF time, which could affect the wetting front propagation in the subsequent ON time, because the injection patterns were the same in both metal plates. Therefore, the position

where the wetting front appeared after the start of 2nd and 3rd injection was analyzed from the visualization images.

Figure 4.8 shows the example of the visualization results at the end of the 1st ON time and from the start of the 2nd injection and the distance between the wetting front position at the end of the Nth ON time and where it appeared in the $(N+1)^{th}$ ON time Δx_b. It was observed from Fig. 4.8 (a) that the liquid film expanded immediately after the start of re-injection and the wetting front appeared upstream of its position at the previous end of the OFF time as mentioned in Section 4.3.1. The difference between the position of WF at the end of 1st ON time and that at the start of 2nd/3rd ON time (Δx_b) in the copper plate was larger than that of the aluminum alloy plate due to the high thermal diffusivity of the copper plate. In addition, for the copper plate, there was almost no difference between Δx_b of the 2nd and 3rd periods, while Δx_b of the 3rd period for the aluminum alloy plate considerably decreased comparing to that of the 2nd period. Thus, the longer OFF time affected the wetting front behavior for the copper plate, leading to the result shown in Fig. 4.7 (b). On the other hand, the effect of the longer OFF time was weak for the aluminum alloy plate, especially during the 2nd OFF time, which led to the further downstream position of the wetting front under the lower DC conditions.

b) Evaluation of wetting front behavior

The removed heat from the metal plate to the liquid film was discussed, and the performance of the pulsed cooling and continuous cooling test was evaluated. The rate of heat transfer from the metal plate to the liquid film $\dot{Q}$ was calculated from Eq. (2).

$$\dot{Q} = \int_{A_{wet}} q_s dA_{wet} \quad A_{wet} : \text{area where } q_s \geq q_{th} \tag{2}$$

The wetted area A_{wet} was determined as the area where the local surface heat flux q_s was equal to or larger than a threshold value q_{th} because the value of A_{wet} was overestimated if the wetted area was simply defined as the area with the positive value of q_s as shown in Fig. 4.4. The value of q_{th} was determined from the value of q_s in the non-cooling (only heating) test; q_{th} = 0.2 and 0.4 MW/m^2 for the aluminum alloy and copper plate, respectively. Figure 4.9 shows the calculated results of $\dot{Q}$ and A_{wet} for the conditions of 30, 50, 80% DC and continuous cooling. For the 1st period, the heat was transferred more rapidly under the lower DC condition due to the higher flow rate of the liquid. The slope $d\dot{Q}/dt$ gradually decreased because the velocity of the wetting front

and the value of the maximum heat flux achieved in the nucleate boiling region decreased as the wetting front was located further downstream as indicated in section 3.3. Especially in the continuous cooling of the aluminum alloy plate, $\dot{Q}$ kept almost constant from around $t = 0.6$ s, although the wetted area gradually expanded. In contrast, $\dot{Q}$ in the copper plate continued to increase with time. There are possible two reasons of this tendency of $\dot{Q}$ in the aluminum alloy plate. One is that the effect of the wetted area expansion competed with that of the decrease in the surface heat flux within the nucleate boiling region. Another is that the single-phase forced convection region gradually became dominant in the wetted area, leading to a small temperature change with time. The temperature of the aluminum alloy plate decreased more easily because the thermal inertia of the aluminum alloy is lower than that of the copper plate. Thus, the ratio of the single-phase forced convection area to the total wetted area was larger for the aluminum alloy plate, and finally the trend of $\dot{Q}$ mentioned above appeared. Immediately after the start of the 2nd injection, $\dot{Q}$ increased more rapidly than in the 1st period and had a sharp spike because the liquid film expanded downstream in a short time as shown in Fig. 4.5. Afterward, $\dot{Q}$ for the aluminum alloy plate kept constant value or decreased while that of the copper plate increased a little bit. The trend of $\dot{Q}$ for the 3rd period was not much different from that for the 2nd period.

To evaluate and compare the heat transfer characteristics in each period, the amount of the removed heat by the liquid film during the Nth pulse period $Q_{N_{th}}$ was calculated by integrating $\dot{Q}$ in the time direction as follows.

$$Q_{N_{th}} = \int_{(N-1)\cdot\tau_p}^{N\cdot\tau_p} \dot{Q}\, dt \tag{3}$$

Figure 4.10 shows the calculated results of $Q_{N_{th}}$. The arrows in each color, which correspond to the color of legends in Fig. 4.10, indicate the value of $Q_{N_{th}}$ for the continuous cooling test calculated from Eq. (3) by setting the Nth period to $t = (N-1)\cdot\tau_p$ - $N\cdot\tau_p$. $Q_{1_{st}}$ increased with the increase in DC for both types of metal plates, even though $\dot{Q}$ was higher and the wetted area further expanded in the lower DC (i.e.; higher flow rate) conditions. This tendency suggested that the longer injection time with the lower flow rate was more effective for cooling with the same usage of the liquid in the situation that the surface temperature was high and the boiling heat transfer was dominant. For the 2nd and 3rd periods in the aluminum alloy, the same tendency appeared in the range from 30% DC to 50% DC, while $Q_{2_{nd}}$ and $Q_{3_{rd}}$ decreased with the increase in DC from 60%. Additionally, the amount of the removed heat did not change much from the 2nd

period to the 3rd period for 72% DC and continuous cooling because $\dot{Q}$ showed constant value in higher DC conditions as shown in Fig. 4.9. This suggested that the shorter injection time with the higher flow rate was a favor to remove the heat in the case that the surface temperature was not much high and the single-phase forced convection region occupied the wetted area. In contrast, $Q_{2_{nd}}$ and $Q_{3_{rd}}$ for the copper plate increased with the increase in DC as was in the 1st period. There were two possible reasons for this. One is that the boiling heat transfer was dominant for each period because of the high thermal inertia. The other is that the wetting front propagation in higher DC was suppressed due to the high thermal diffusivity of the copper plate as discussed in Figs. 4.7 and 4.8. Figure 4.11 shows the time history of the minimum value of the temperature difference $\Delta T_{\min}$ as defined by Eq. (4).

$$\Delta T_{\min}(t) = \min[T_s(x, y, t) - T_s(x, y, 0)] \tag{4}$$

As discussed above, the copper plate was more difficult to be cooled than the aluminum alloy plate for any DC owing to the higher thermal inertia. Figure 4.12 shows the contribution of the heat removal per each degree of wall superheat $\Delta T_{\sup}$ to the total amount of the removed heat during each period. The $dQ_{N_{\text{th}}}/Q_{N_{\text{th}}}$ for the continuous cooling was calculated in the same way as Fig. 4.10. In lower DC conditions (30% DC and 50% DC in Fig. 4.12) for the aluminum alloy plate, the peak of the removed heat for each pulse period appeared in nearly the same range of $\Delta T_{\sup}$ because the temperature relatively became high during each OFF time. In higher DC conditions (80% DC and continuous cooling in Fig. 4.12), however, the peak shifted to the lower $\Delta T_{\sup}$, which meant that the dominant mode of the heat transfer changed from boiling to single-phase forced convection. For the copper plate, the heat was transferred in the narrower range of $\Delta T_{\sup}$ compared to the case of the aluminum alloy plate. In addition, the peak was in a higher degree of wall superheat due to the high thermal inertia as discussed in Fig. 4.11, although the peak gradually shifted in higher DC conditions.

Finally, the performance of the pulsed cooling was compared to that of the continuous one. The total amount of the removed heat $Q_t (= \sum Q_{N_{th}})$ was calculated, and then, the non-dimensional removed heat Q^* defined as Eq. (5) was used for evaluating the cooling performance.

$$Q^* = \frac{Q_{t_{\text{pulse}}}}{Q_{t_{\text{continuous}}}} \tag{5}$$

The calculated results of Q^* is shown in Fig. 4.13. For the aluminum alloy plate, Q^* was greater than unity for each DC condition, which meant more heat was removed in the pulsed cooling test. In addition, Q^* had a peak in the range from 50% DC to 60% DC because $Q_{2_{nd}}$ and $Q_{3_{rd}}$ had a peak in that range. As discussed in Figs. 4.10 and 4.12, it was assumed that the longer injection time with a lower flow rate was more favorable for removing heat when the boiling heat transfer was dominant, and vice versa. Therefore, it could be concluded that the appropriate balance of the ON/OFF time produced the situation that boiling and single-phase forced convection heat transfer competed for the amount of removed heat with each other, resulting in a peak of Q^* for the aluminum alloy plate. In contrast, Q^* monotonously decreased with the decrease in the duty cycle for the copper plate because boiling heat transfer was dominant for removing heat due to the higher thermal inertia, and the wetting front propagation was suppressed owing to the higher thermal diffusivity.

4.4 Conclusions

Cooling tests of the superheated metal plate by intermittent injection of the liquid jet were carried out to enrich the understanding of the liquid film behavior and the heat transfer characteristics during the pulsed cooling processes. The liquid film behavior and the metal temperature were simultaneously measured by using a high-speed camera and an infrared camera. In the pulsed cooling tests, the flow rate and duty cycle were varied under the same injection quantity from the viewpoint that the cooling performance needs to be enhanced with the same usage of the coolant. The continuous cooling test with the time-averaged flow rate of the pulsed cooling was also conducted. In the present study, two types of metal plates (aluminum alloy and copper) were used to investigate the effects of the thermal properties of the metal plate on the cooling performance.

The wetting front of the liquid film gradually propagated downstream after the start of the cooling. Since the injection was cut off, the residual liquid film was consumed with nucleate boiling. Immediately after re-injection, the liquid film rapidly expanded because the temperature rise of the metal plate during the OFF time did not exceed the temperature drop during the previous ON time in the present study. Therefore, the metal plate was cooled with each injection. The unsteady liquid film behavior and heat transfer characteristics were successfully captured by measuring the opposite side temperature of the cooled surface by the liquid film and the solution of the inverse heat conduction problem.

The wetting front position and the amount of the removed heat by the liquid film were

evaluated for each condition. For the 1st pulse, in which boiling was the dominant mode for cooling, the longer injection was more effective for removing heat although the wetting front was shorter in the higher duty cycle. In subsequent pulses, the amount of the removed heat had a peak in the range of a certain duty cycle for the aluminum alloy. This came from the situation that the cooling mode shifted from boiling to single-phase forced convection especially in higher duty cycle conditions. In contrast, the same tendency as the 1st pulse was observed in the copper plate. There were two possible reasons for that trend. One is that the dominant mode of the heat transfer could be boiling during subsequent pulses because the temperature of the copper plate did not easily change due to the high thermal inertia. The other is that the wetting front propagation was more suppressed in longer OFF time conditions owing to the high thermal diffusivity of the plate.

References

[1]   S. Takata, Y. Daimon, K. Sugimori, N. Matsuda, and Y. Tashiro, "Design verification results of japanese 120N Bi-propellant thrusters (HBT-1) based on its first flight in HTV3," *49th AIAA/ASME/SAE/ASEE Joint Propulsion Conference*, AIAA-2013-3754, 2013.

[2]   J. Wassenberg, P. Stephan, and T. Gambaryan-Roisman, "Heat transfer during pulsating liquid jet impingement onto a vertical wall," *Heat and Mass Transfer/Waerme- und Stoffuebertragung*, vol. 57, no. 4, pp. 617-629, 2021.

[3]   S. Abishek and R. Narayanaswamy, "Low Frequency Pulsating Jet Impingement Boiling and Single Phase Heat Transfer," *International Journal of Heat and Mass Transfer*, vol. 159, Article 120052, 2020.

[4]   Q. Ye, Y. Zhang, and J. Wei, "A comprehensive review of pulsating flow on heat transfer enhancement," *Applied Thermal Engineering*, vol. 196, Article 117275, 2021.

[5]   G. Fujii, Y. Daimon, K. Furukawa, C. Inoue, D. Shiraiwa, and N. Tanaka, "Visualization of Coolant Liquid Film Dynamics in Hypergolic Bipropellant Thruster," *Journal of Propulsion and Power*, vol. 38, no. 2, pp. 267-273, 2022.

[6]   R. C. Schindler and L. Schoenman, "Development of a five-pound thrust bipropellant engine," *Journal of Spacecraft and Rockets*, vol. 13, no. 7, pp. 435-442, 1976.

[7]   N. Tanaka, D. Shiraiwa, T. Kaneko, and K. Furukawa, "Development of Low-thrust Thruster with World's Highest Performance Contributing to Life Extension

of Artificial Satellites," *Mitsubishi Heavy Industries Technical Review*, vol. 54, no.4, 2017.

[8]   S. D. Rosenberg and L. Schoenman, "New generation of high-performance engines for space propulsion," *Journal of Propulsion and Power*, vol. 10, no. 1, pp. 40-46, 1994.

[9]   T. Inoue, C. Inoue, G. Fujii, and Y. Daimon, "Evaporation of Three-Dimensional Wavy Liquid Film Entrained by Turbulent Gas Flow," *AIAA Journal*, vol. 60, no. 6, pp. 3805-3812, 2022.

[10]   C. Liu, C. Tang, H. Mu, and Z. Huang, "A data fusion approach with high spatiotemporal resolution for wall temperature measurement upon jet impingement," *International Journal of Heat and Mass Transfer*, vol. 183, Article 122084, 2022.

[11]   K. Tsukamoto et al., "On the onset of quench during spray cooling: The significance of oxide layers," *Applied Thermal Engineering*, vol. 179, Article 115682, 2020.
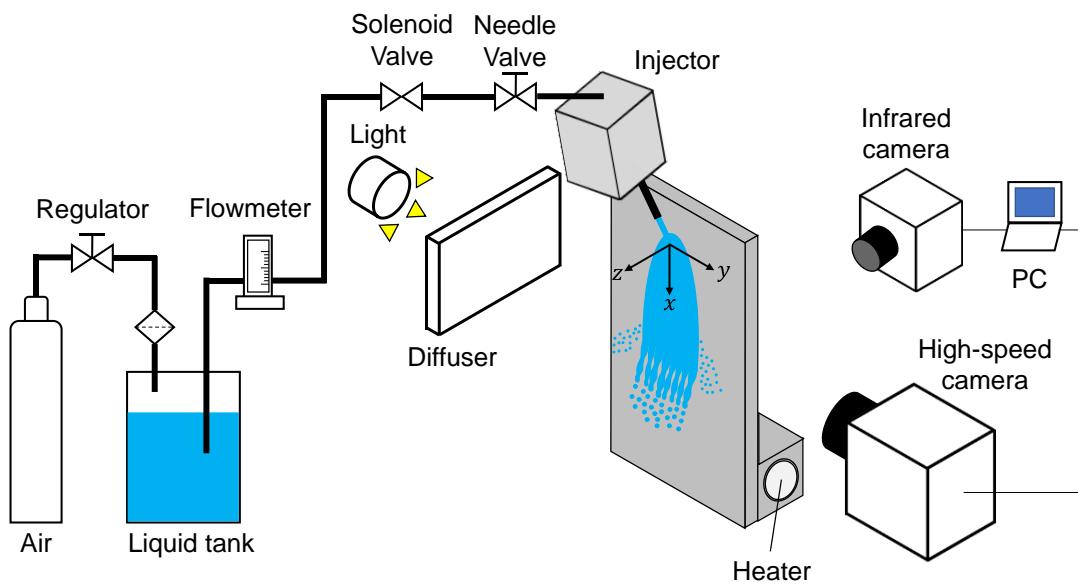
Fig. 4.1 Schematic of the experimental apparatus
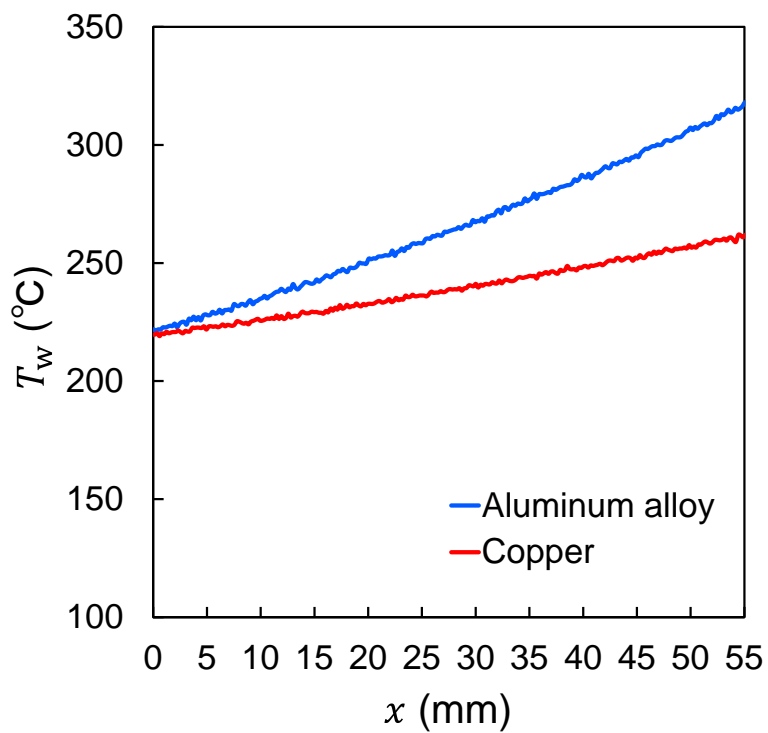
Fig. 4.2 Initial temperature distribution on the x-axis for each metal plate
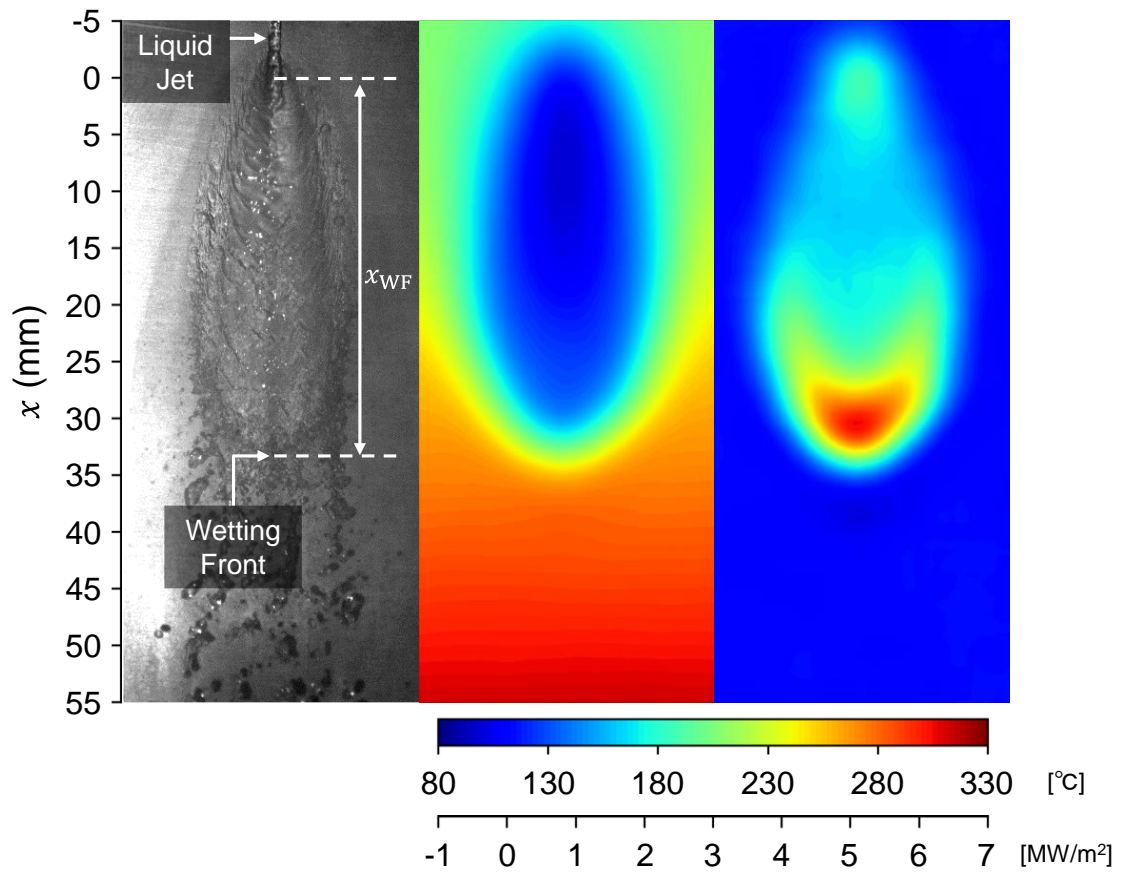
Fig. 4.3 Direct image of liquid film (left) and estimated temperature (middle) and heat flux (right) distribution on the front surface at $t = 0.5$ s.
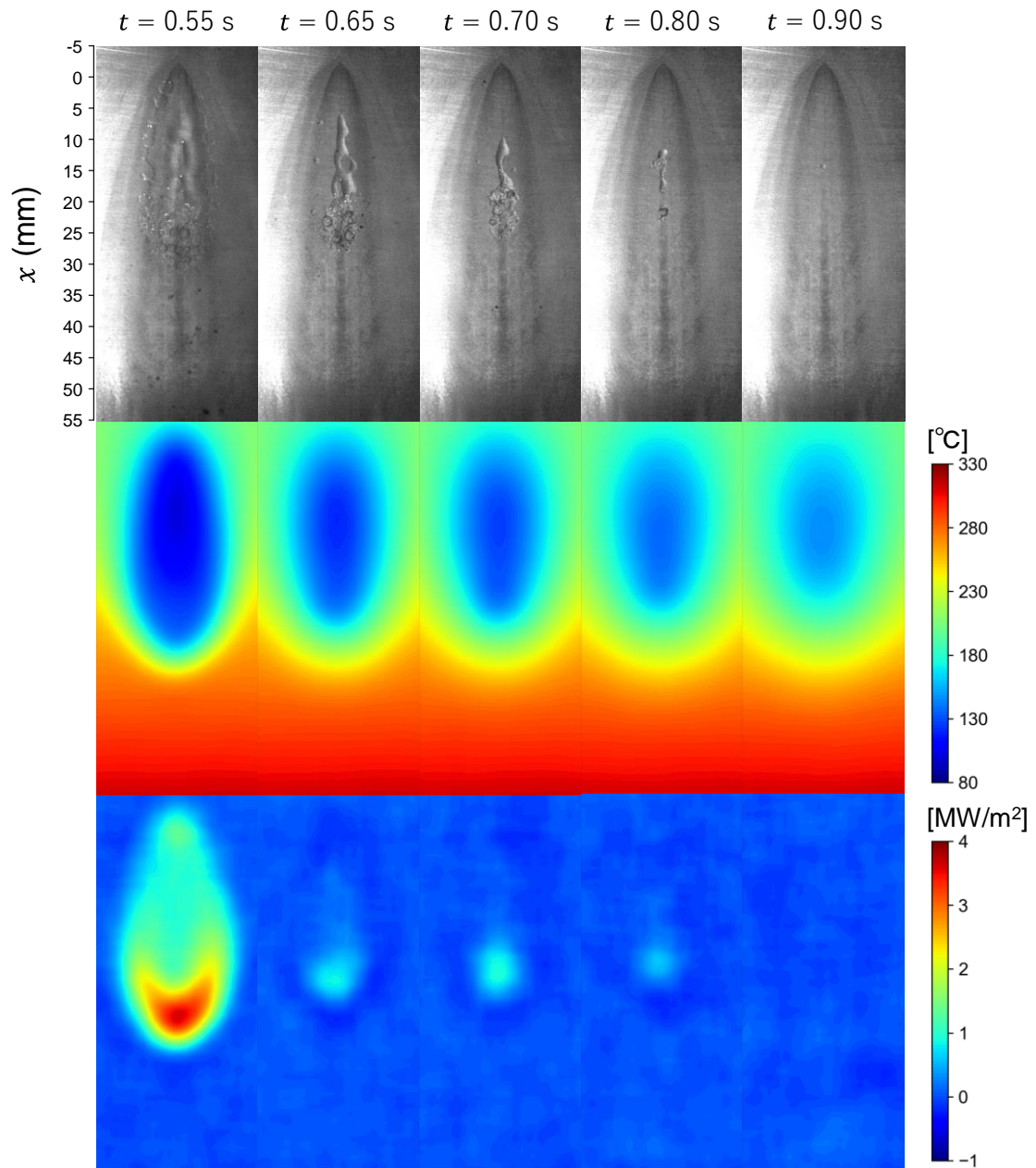
Fig. 4.4 Evaporation process of liquid film during 1st OFF time; direct image (upper)
and estimated temperature (middle) and heat flux (bottom) distribution on the
front surface
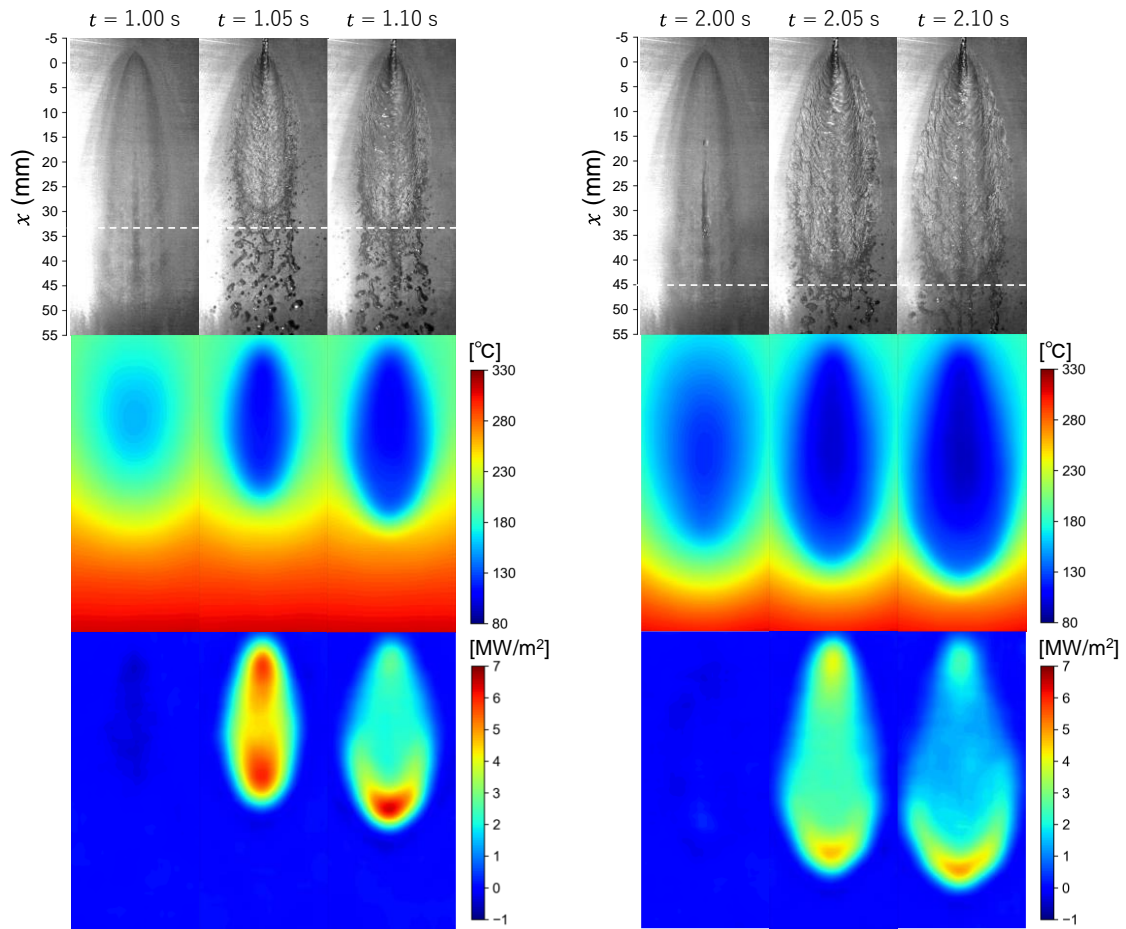
Fig. 4.5 Propagation process of liquid film during 2nd (left) and 3rd (right) period; direct image (upper) and estimated temperature (middle) and heat flux (bottom) distribution on the front surface. White dashed lines in each direct image indicate the wetting front position at the end of the previous ON time.
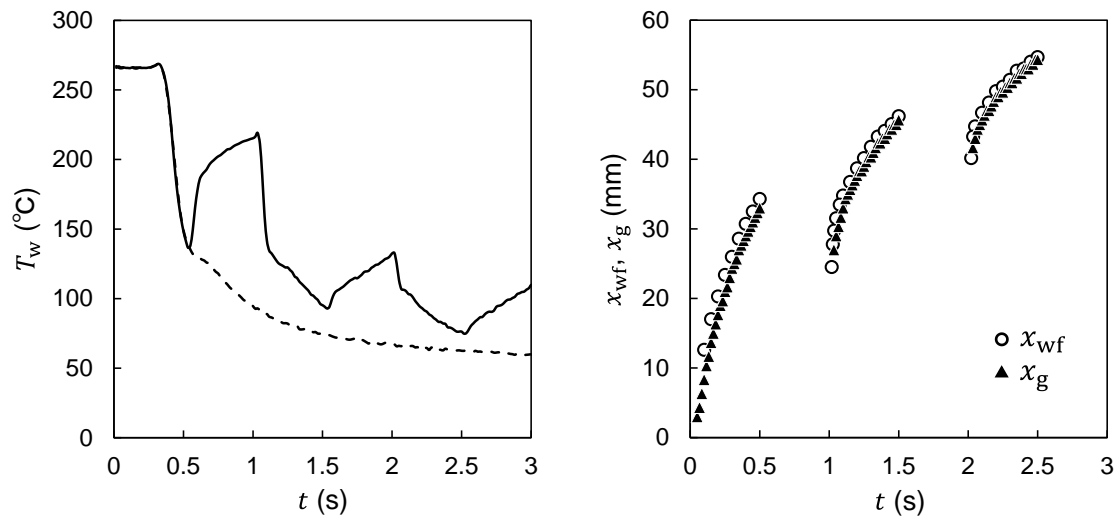
Fig. 4.6 Time history of temperature at $x = 30.3$ mm on the x-axis (left) and position of x_wf and x_g (right)
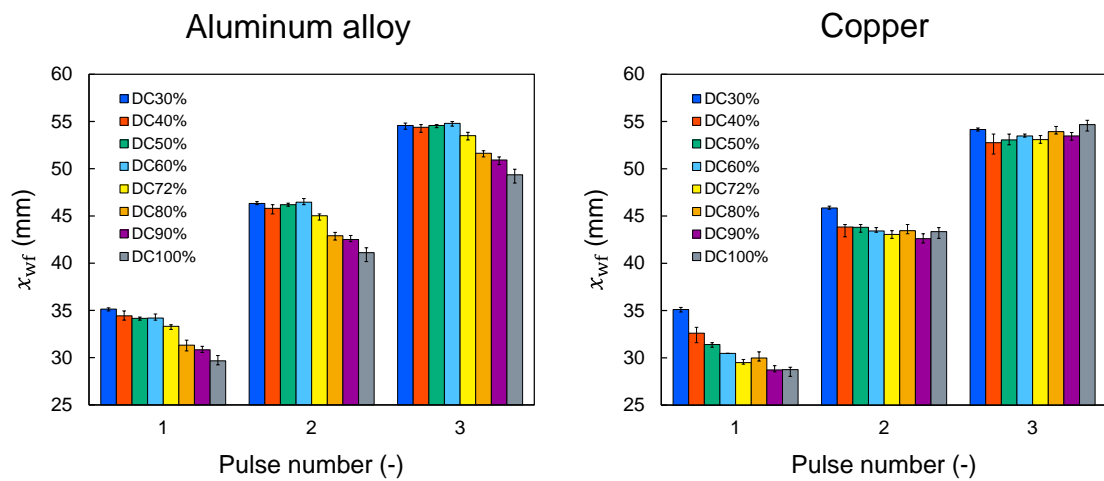
Fig. 4.7 Wetting front position at end of each ON time; (left) aluminum alloy, (right) copper
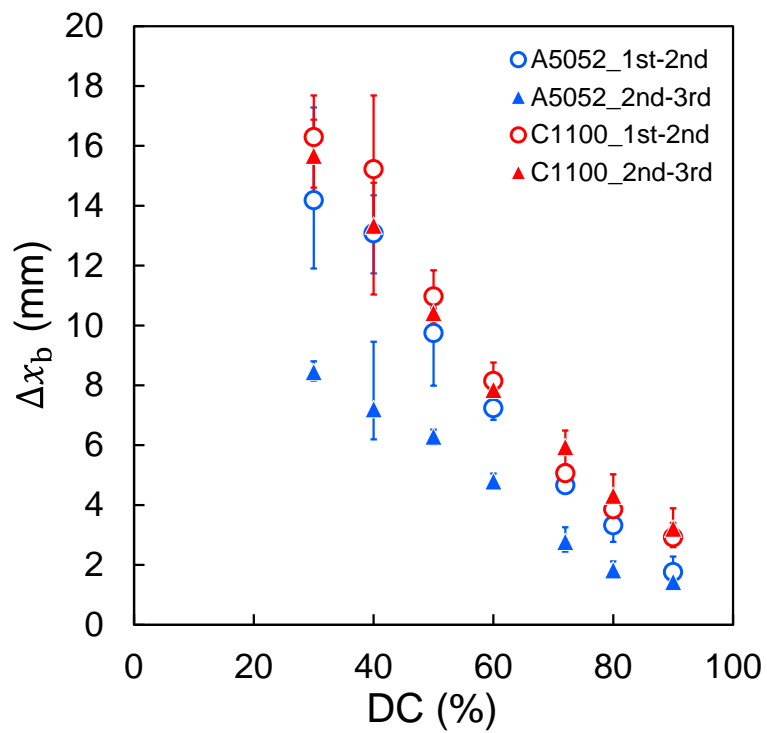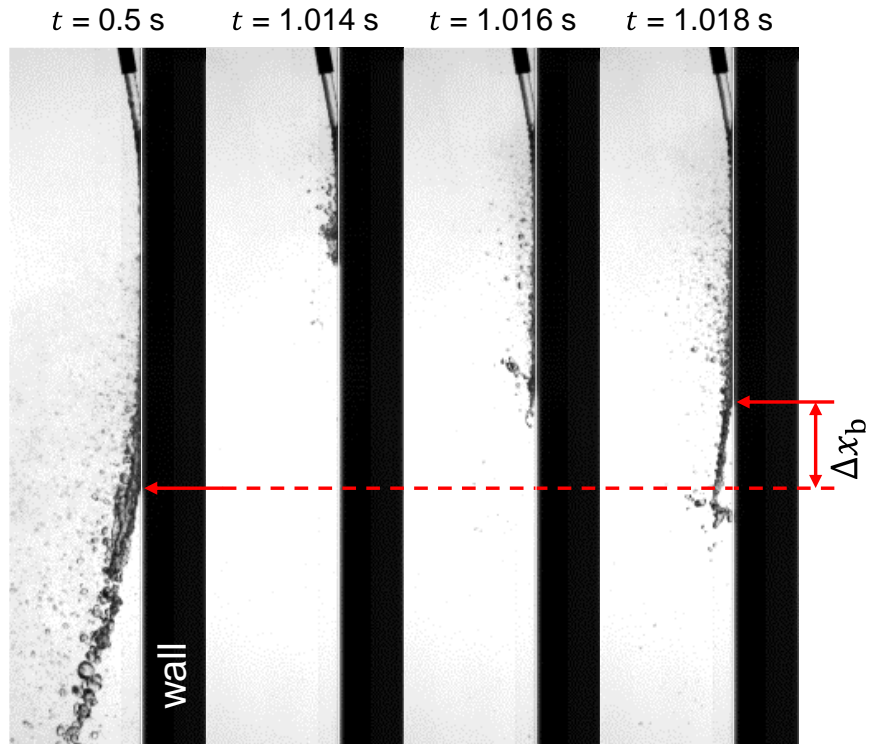
Fig. 4.8 Side view of propagation process of liquid film after re-injection (upper) and Δx_{b} under each condition (bottom)
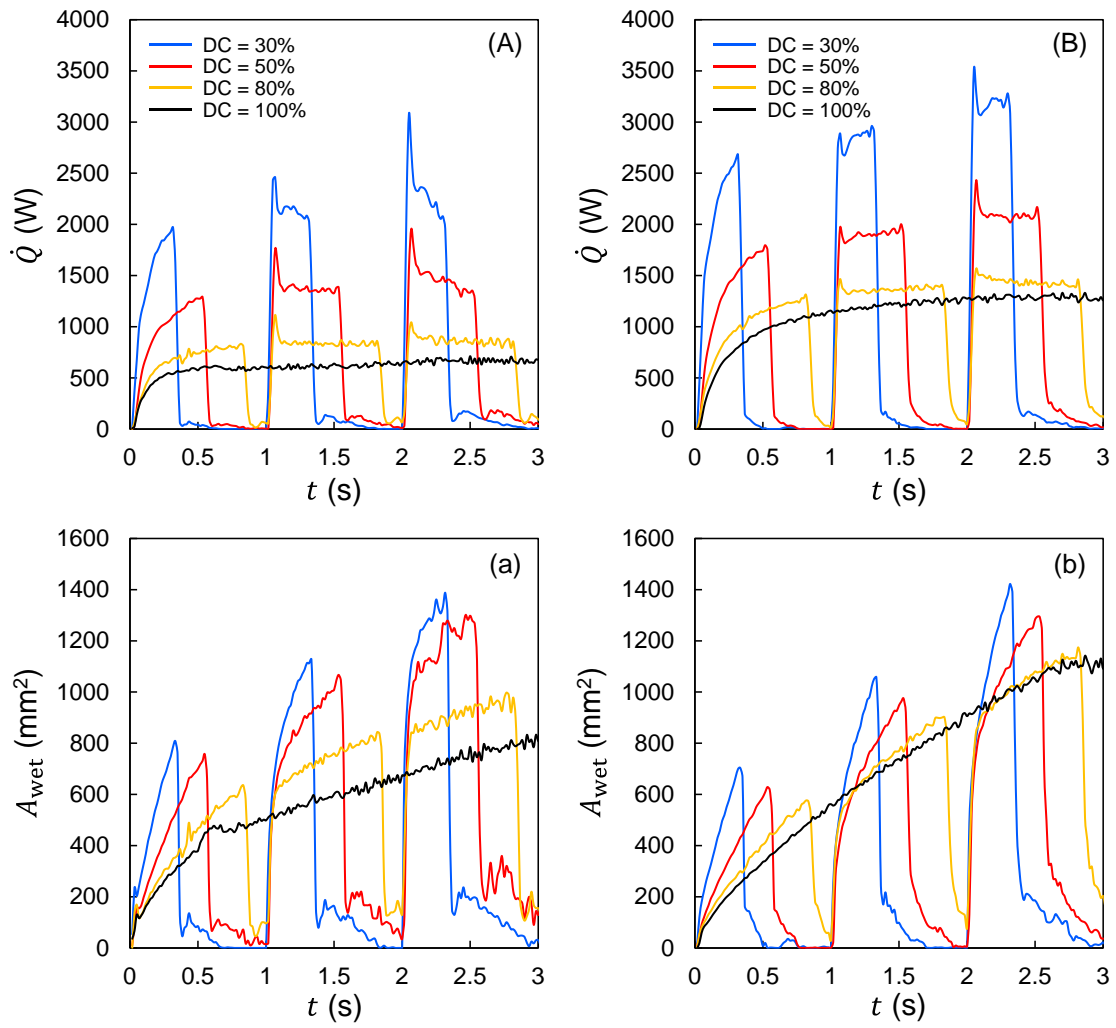
Fig. 4.9 Time history of rate of heat transfer and wetted area; (A, a) aluminum alloy, (B, b) copper.
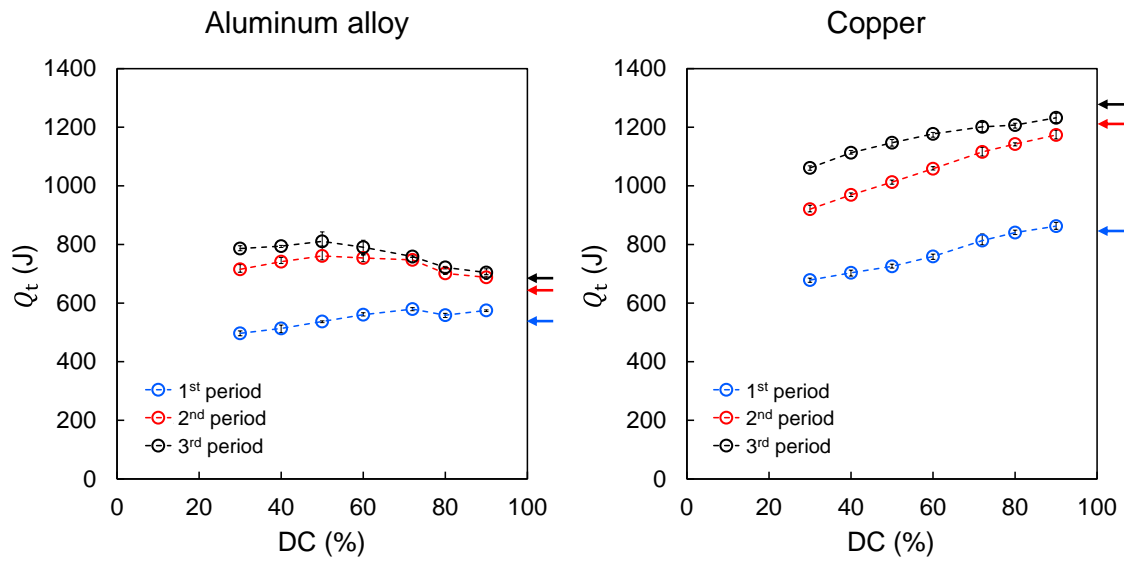
Fig. 4.10 Amount of removed heat during each period; (left) aluminum alloy, (right) copper
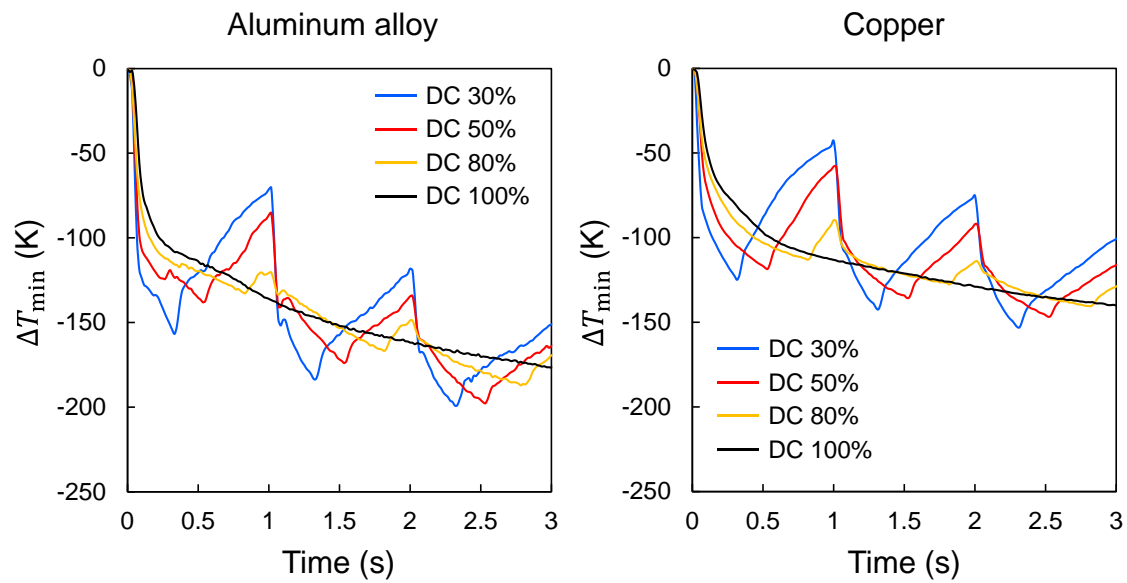
Fig. 4.11 Time history of minimum value of temperature difference defined by Eq. (4); (left) aluminum alloy, (right) copper
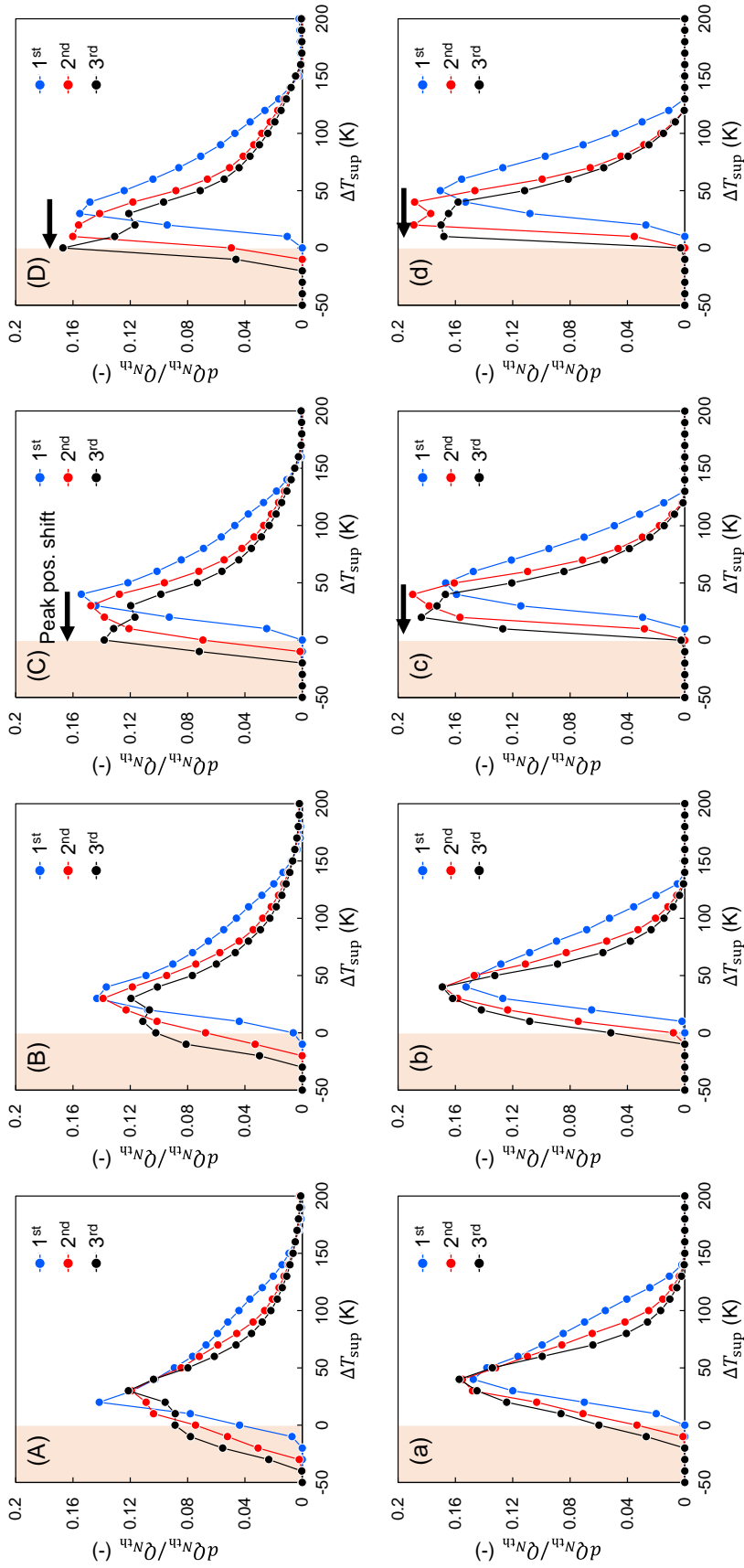
85

Fig. 4.12 Contribution of removed heat per each degree of wall superheat to total amount of removed heat during each period. (A, a) 30% DC, (B, b) 50% DC, (C, c) 80% DC, (D, d) continuous injection. Capital letters and small letters respectively indicate results of aluminum alloy and copper plate
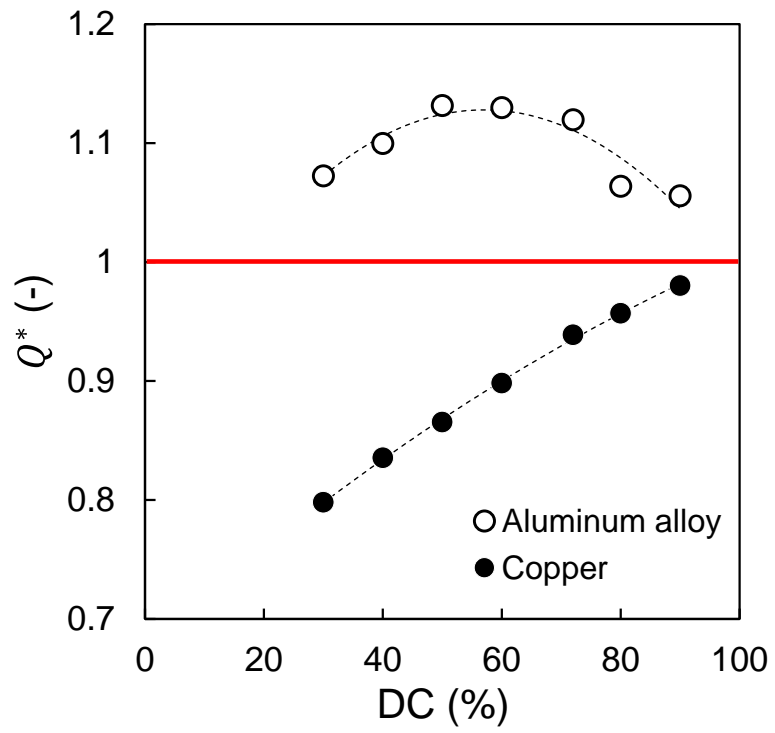
Fig. 4.13 Non-dimensional removed heat by liquid film calculated by Eq. (5)

Table 4.1 Thermal properties of metal plate

Material	Aluminum alloy (A5052)	Copper (C1100)
Density ρ_w, kg/m^3	2680	8900
Specific heat c_w, J/kg$\cdot$K	900	385
Heat conductivity k_w, W/m$\cdot$K	137	391
Thermal diffusivity α_w, m^2/s	5.68×10^{-5}	1.14×10^{-4}
Thermal inertia $\sqrt{\rho_w c_w k_w}$, kJ/(m$^2\cdot$s$^{0.5}\cdot$K)	18.2	36.6

Table 4.2 injection patterns

Duty cycle, %	Flow rate, mL/min	Jet Reynolds number	Injection time, s
30	600	11500	0.30
40	450	8600	0.40
50	360	6900	0.50
60	300	5800	0.60
72	250	4800	0.72
80	225	4300	0.80
90	200	3800	0.90
100 (continuous)	180	3500	3.00

Chapter 5 Boiling induced atomization appeared in a liquid film formed by wall impinging jet on a superheated wall

5.1 Introduction

One of the important factors, which affect the cooling performances in the fields such as liquid rocket engines and emergency cooling systems of the nuclear reactor core, is the droplet entrainment from the liquid film into the core gas flow [1]. The droplet entrainment is caused by the hydrodynamic instabilities of the liquid-gas interface owing to the high shear stress between the fast gas and the liquid film [2] or bubble bursting in the liquid film induced by nucleate boiling [3, 4]. The liquid flow rate for the cooling of the wall is reduced by the droplet entrainment, leading to the deterioration of the cooling performance; shortening of the liquid film length in liquid rocket engines [2], or the burnout in the nuclear reactor systems [5]. Therefore, the total volume of droplet dispersion from the liquid film and its mechanisms need to be elucidated for predicting the cooling performance and preventing the thermal failure of industrial devices. The mechanism of the droplet entrainment by the liquid-gas interface instabilities has been investigated through the visualization measurement [6, 7], and the development of the theoretical model [8]. On the other hand, there is limited information on the droplet dispersion from the liquid film flow by the boiling phenomena [4], although detailed results on the secondary droplets from the interaction with boiling between the droplet and the hot surface can be found in relation to the spray cooling, direct injection engines [9, 10].

The atomization with droplet dispersion from the liquid film induced by boiling phenomena also occurs during the jet impingement cooling process [11]. It is of great importance to know the characteristic values such as the number, size and velocity of the droplets in the cooling processes [12]. In this study, therefore, boiling induced atomization processes that appeared in the liquid film by wall impinging jet on the superheated wall were visualized via magnified high-speed imaging to gain insight into the atomization processes and obtain experimental findings, such as the droplet diameter and velocity produced by the boiling phenomena.

5.2 Experimental description

The basic configuration of the experimental apparatus was the same as that in chapter 4. Unlike in chapter 4, the magnified high-speed imaging system was adopted in the apparatus in this chapter to visualize the atomization processes that appeared in the liquid film in detail. Bellows, a lens (Nikon Zoom-Nikkor, focal length 35-70 mm, F#3.3), and a high-speed camera (Photron FASTCAM SA1.1) were used for the magnified high-speed imaging with the backlight technique. The frame rate was set to 20,000 and 54,000 fps to visualize atomization processes. The exposure time was set to 8.3 μs and 5.4 μs at the frame rate of 20,000 fps and 54,000 fps, respectively. The spatial resolution for magnified imaging was 5.74 μm/pixel. The metal plate (aluminum alloy A5052, 2 mm thick, 50 mm wide and 66 mm long) was heated by using a rod heater. The test liquid was water at a room temperature of approximately 20℃. The same procedure as in chapters 3 and 4 was applied to measure and analyze the temperature of the metal plate. To solve the inverse heat conduction problem, the metal plate with a width of 50 mm, a length of 46 mm (temperature measurement area), and a thickness of 2 mm was divided into 50×46×20 cells. The mass flow rate of the test liquid, nozzle diameter and impingement angle which were parameters affecting the liquid film formation were respectively fixed at 5.0 g/s, 0.7 mm and 10° because the objective of this study was to clarify the boiling-induced atomization appeared in the liquid film on the heated wall. The injection of the test liquid was started when the wall temperature of the impingement point rose to 250℃. Experimental conditions and imaging conditions are listed in Table 5.1.

To investigate the relationship between the liquid film thickness and the splashed droplet, the thickness of the liquid film on the plate with non-heat-input condition (i.e., without boiling) for the steady state was measured using a confocal fiber displacement sensor (Omron ZW-7000). The injection condition for the measurement of the liquid film thickness was the same as that in the visualization test.

5.3 Results and discussion

The contents of this section are composed of the following. Section 5.3.1 represents the characteristic atomization processes observed in the liquid film on the superheated wall. Therefore, the visualization results at a fixed imaging position of $x = 10$ mm are shown in section 5.3.1. In section 5.3.2, atomization processes with the bubble bursting which can be seen in the nucleate boiling regime are visualized by changing the imaging position ($x = 2, 5, 10, 15, 20$ mm) and theoretically investigated. Finally, section 5.3.3

provides the total volume of the dispersed droplet from the liquid film by the nucleate boiling estimated from the measured frequency of the bubble bursting and the mean droplet diameter indicated in section 5.3.2.

Before starting the description of the results and discussion, the several assumptions for measurement and analysis of the atomization processes listed below are adopted.

(1) In the case of the oblique impingement of the liquid jet, the stagnation point and impingement point are strictly different, but it was assumed that both were the same because it was difficult to determine the stagnation point directly from the images.

(2) As described later, the target in this chapter is the atomization processes along the rim of the liquid film. Thus, a coordinate system along the rim of the liquid film should be set up for discussion. However, the liquid film expands as the metal is cooled, leading to the movement of the coordinate system over time. For simplification, therefore, the measurement results and analysis were based on the x axis.

(3) Bubbles do not grow in a perfectly hemispherical or spherical shape. However, only the bubble height (i.e., the distance between the bubble top and the metal surface) can be measured from the obtained images with the present experimental setup. In this chapter, therefore, the bubble height is considered as the bubble radius.

(4) The thermal boundary layer in the liquid film is considered to be laminar, although the turbulent thermal boundary layer is possible to grow in the liquid film when bubble growth occurs.

5.3.1 Characteristic atomization processes appeared in liquid film on superheated wall

Figure 5.1 shows (a) the top view and (b) the side view of the liquid film formed on the superheated wall. The liquid film was fully deflected from the wall at the leading edge, as indicated in chapters 3 and 4. As shown in Fig. 5.1 (a) and (b), many droplets scattered from the rim of the liquid film near the WF (region I) and upstream of the WF (region II). The dispersed droplets in Fig. 5.1(b) were assumed to be caused by the boiling phenomena (nucleate, transition and film boiling). In addition, it was of interest that the size of droplets near the WF seemed to be larger than those upstream the WF.

To investigate the atomization processes in the regions I and II, the measurement position was fixed at $x = 10$ mm and two different timings from the start of injection were selected. Figure 5.2 shows direct images of the liquid film at a different time and the yellow rectangle in each image represents the imaging area (i.e., near the WF and

upstream the WF). Figure 5.3 shows the sequential events observed at each visualized area in Figs. 5.2(a) and (b) In Fig. 5.3, the flow direction of the liquid film was from the left side to the right side. In Fig. 5.3(a), the atomization process in the region I of Fig. 5.2(b) with a relatively higher degree of wall superheat is shown, and it was clearly observed that the amplitude of the unstable wave on the ligament surface increased and the large droplet pinched off from the ligament. In Fig. 5.3(b) corresponding to the region II of Fig. 5.2(b), on the other hand, the nucleate boiling can be clearly observed. The bubble grew according to Eq. (5.1) as shown in Fig. 5.4, which meant the bubble growth was determined by the heat transfer from the liquid phase to the gas phase [13].

$$b \sim \sqrt{\alpha t^*} \qquad (5.1)$$

b, α and t^* denote the bubble radius, the thermal diffusivity of the liquid and the elapsed time since the bubble start to grow, respectively. The bubble eventually burst, leading to the subsequent fragmentation from the ligament to the small droplets. It was reported that two kinds of droplets (i.e., jet droplets and film droplets) could be produced through the bubble bursting event [14]. Under the condition of the present experiment, no jet drops were observed because only a dry patch was formed on the wall after the bursting event, while many film drops were produced as shown in Fig. 5.3(b). Here, the thickness of the bubble cap h and droplet diameter d from the bubble bursting was considered. Figure 5.5 shows the direct images and schematic illustrations of a sequential event of the fragmentation processes with bubble bursting. From these images, the retraction velocity of the liquid film after the puncture of the bubble, which is known as Taylor-Culick velocity V_{TC} [15, 16] indicated in Eq. (5.2), was measured, and then, the value of h was estimated.

$$V_{\mathrm{TC}} = \sqrt{\frac{2\sigma}{\rho_{\mathrm{l}} h}} \qquad (5.2)$$

σ and ρ_{l} are the surface tension and density of the liquid, respectively. Figure 5.6 shows the relationship between the bubble radius just before rupture b^* and the estimated value of h calculated from Eq. (5.2). Although there was variation owing to the measurement from images (because the estimated value of h is proportional to v^2 as indicated in Eq. (5.2)), it can be seen that $h \approx 10$ μm at any b^*. Then, the size of droplets from bursting bubbles was analyzed although droplets that were in focus and clearly visible were able

to be measured at only four of the results in Fig. 5.6 (shown as black plots). In the previous study, the mean droplet diameter $\langle d \rangle$ from the bursting was scaled as Eq. (5.3) considering that a Rayleigh-Taylor instability induced by centripetal acceleration during retraction lead to the formation of ligaments which were then stretched out by centrifugation and the subsequent disintegration due to a Plateau-Rayleigh instability [17, 18].

$$\langle d \rangle \sim b^{*3/8} h^{5/8} \tag{5.3}$$

Figure 5.7 shows the measurement result of the droplet diameter according to Eq. (5.3) using the estimated value of h. The droplet size of film droplets may be well predicted by Eq. (5.3) although there were only four cases in which droplets were clearly visible to be measured.

Then, the relationship between the ejection velocity and the droplet diameter was investigated. Figure 5.8 shows the measurement results of the droplet velocity in z direction v_n against the droplet diameter. For the measurement of v_n, only spherical droplets were analyzed to facilitate the analysis. The bold line in Fig. 5.8 indicates the local Weber number, which was defined as Eq. (5.4), of unity.

$$We = \frac{\rho_l v_n^2 d}{\sigma} \tag{5.4}$$

Although the plots were scattered in a certain range owing to the image measurement, v_n was distributed around $We \sim O(1)$, which indicated that v_n and d were governed by the relationship between the inertia force of the ligament and the surface tension. The fragmentation from the ligament occurred around $We \sim O(1)$.

5.3.2 Droplet size produced by the nucleate boiling in the liquid film

Results in section 5.3.1 indicated that the droplet diameter from the bursting bubble was determined by the maximum bubble radius and bubble cap thickness. They are likely to change along the flow direction of the liquid film because the superheated state of the liquid film varies based on location. In this section, therefore, the variation of the maximum bubble radius, bubble cap thickness, and mean droplet diameter along the flow direction was evaluated by the visualization results at each position (x = 2, 5, 10, 15, 20 mm).

Figure 5.9 shows a schematic of the nucleate boiling induced atomization that appeared in the rim of the liquid film formed by the impinging jet. The initially cold liquid film is gradually heated by the wall inside the thermal boundary layer and its thickness increases from the stagnation point as the liquid film flows downstream. Based on assumption (4), the thermal boundary layer thickness δ_α at a certain distance from the stagnation point x' is given by

$$\delta_\alpha \sim \sqrt{\alpha \cdot t(x')} \tag{5.5}$$

where $t(x')$ denote the constant and the time it takes for the liquid film to move to the position x' from the stagnation point, respectively. $t(x')$ can be represented by Eq. (5.5) using the advection velocity of the liquid film u_f, according to assumption (2).

$$t(x') = \int_0^{x'} \frac{d\xi}{u_f(\xi)} \tag{5.6}$$

From assumption (1) (i.e., $x' = x$), $t(x)$ can be estimated by measuring the advection velocity of the liquid film. In Fig. 5.10(a), the rim of the liquid film at a certain time and 5.56 μs after that time (equivalent to 3 frames at the frame rate of 54,000 fps) are shown. u_f at each position was obtained by the traveled distance of the ligament formed by the boiling. Fig. 5.10(b) shows the measurement and calculated results of u_f and $t(x)$ at each position from the impingement point, in which the error bars of u_f are the standard error. The liquid film moved at the constant velocity of about 5 m/s up to $x = 5$ mm and then decelerated because the liquid film was fully covered by the boundary layer, leading to the rapid increase of $t(x)$ further downstream.

At each point, the bubble grew according to Eq. (5.1) as shown in Fig. 5.4. Assuming that the volume equivalent to δ_α^3 evaporates on the wall, being the bubble with the radius of b. Considering the mass conservation just before bursting, the following equation can be deduced by using the maximum bubble radius of b^*.

$$\rho_l \delta_\alpha^3 \approx \rho_g b^{*3} \tag{5.7}$$

ρ_l and ρ_g denote the density of the working fluid at the liquid phase and gas phase, respectively. In the present study, the working fluid was water and b^* was derived from Eq. (5.7) by using the density of water at both phase under atmospheric pressure.

$$b^* \approx 12\delta_\alpha \qquad\qquad (5.8)$$

Figure 5.11 shows the relationship between b^* and δ_α, in which δ_α was calculated from Eq. (5.5) and $t(x)$ shown in Fig. 5.10(b). For b^* in Fig. 5.11, the averaged values of about 120 measured data at each position is indicated. The maximum bubble radius increased along the flow direction of the liquid film because the thermal boundary layer developed further downstream. Eq. (5.8) could predict the order of magnitude of b^* and its trend against δ_α.

Next, the variation of the bubble cap thickness h along the flow direction was investigated. As discussed in Fig. 5.7, Eq. (5.3) proposed by Lhuissier and Villermaux [17, 18] well predicted the relationship of b^*, h, and $\langle d \rangle$. Here, the value of h was estimated from Eq. (5.3) by measuring b^* and the produced droplet diameter d from the visualization images because b^* and d could be measured more easily than V_{TC}. Figure 5.12 shows the estimated results of h at each position, in which the error bars are the standard error. Additionally, the averaged value of h at $x = 10$ mm estimated from Eq. (5.3) (i.e.; the averaged value of the plots in Fig. 5.6). As shown in Fig. 5.12, the bubble cap thickened further downstream. The bubble cap thickness can be associated in some way with the liquid film thickness H because some part of the liquid film above the nucleation point is elevated as the bubble grows. Figure 5.13 shows the distribution of H at the rim along the flow direction. The liquid film thickness at the rim also increased further downstream, which can lead to the thickening of the bubble cap.

Finally, Figure 5.14 shows the averaged value of the droplet diameter at each position. The error bars are the standard error. As shown in Fig. 5.14, the larger droplets were produced further downstream through the bubble bursting event because the maximum bubble size and bubble cap thickness increased as the liquid film moved downstream as mentioned above.

5.3.3 Estimation of the total volume of dispersed droplets from a liquid film

In this section, the total volume of the dispersed droplets from the liquid film is estimated. First, the frequency of the bubble bursting was measured from the visualization image. The measurement area was again fixed at $x = 10$ mm. Figure 5.15 shows the time history of the degree of wall superheat ΔT_{sup} and the surface heat flux q_s estimated by solving the inverse heat conduction problem. The number of times of the bubble bursting C was counted every Δt in the periods highlighted in orange in Fig. 5.15 (Δt; time step of the temperature measurement). Figure 5.16 shows the counting results against the

degree of wall superheat. The frequency of the bubble bursting per unit area F was calculated from the width and depth of the measurement area, Δt, and C. The width of the measurement area Δx was 1.44 mm. The depth of the measurement area was assumed to be equal to the lope width w_{lp} which meant the width of the thickened region of the liquid film in the y direction, because the bubble growth and bursting occurred in the thickened region. Figure 5.17 shows the measurement result of the liquid film thickness distribution in the y direction. From Fig. 5.17, the lope width was set to 1 mm. As shown in Fig. 5.16, the number of the bubble bursting decreased with the decrease in ΔT_{sup} because the number of the active nucleation site and the bubble growth rate decreases as the surface temperature of the wall decreases. To verify the counting value of C, the heat flux from the metal surface was estimated by following equation.

$$q_{est} = \rho_v \cdot \left(\frac{2}{3}\pi b^{*3}\right) \cdot h_{lv} \cdot F \tag{11}$$

h_{lv} denotes the latent heat. The calculated results of q_{est} are shown in Fig. 5.18 with the estimated heat flux by solving the inverse problem. Although the value of q_{est} was lower than q_s because the heat value determined by b^* did not include all the heat removed from the wall by the liquid film, the order of magnitude of q_{est} (~1 MW/m^2) was equal to that of q_s. Therefore, the counting results of C was reasonable.

Using the measurement results of C, the accumulated volume of dispersed droplets from the liquid film was then estimated. Figure 5.19 shows the direct image of the liquid film at $t = 0.6$ s taken from the top, and the accumulated volume of dispersed droplets at this time was estimated. The white grids in Fig. 5.19 indicate the grids for solving the inverse problem; the estimated temperature could be obtained for each grid. For the estimation of the dispersed droplets, the rim of the liquid film was divided into five sections as shown in the areas highlighted in each color in Fig. 5.19. Each section in Fig. 5.19 is named section 1, 2, 3, 4, and 5 from left to right, and section 1, 2, 3, 4, and 5 include $x = 2, 5, 10, 15,$ and 20 mm, respectively. The accumulated volume of dispersed droplets from each section $\dot{m}_{di}$ ($i = 1, 2, 3, 4,$ and 5) was calculated to estimate the total volume from the liquid film $\dot{m}_d$ ($= \sum 2\dot{m}_{di}$). Figure 5.20 shows the averaged value of ΔT_{sup} in each section. ΔT_{sup} generally increased further downstream although only the value in section 1 showed the opposite trend because the liquid film width of the region was smaller than that in other sections and the temperature did not easily decrease. Using the value of ΔT_{sup} in Fig. 5.20, the represented value of F in each section can be derived from the tentative approximation formula of ΔT_{sup} and F as indicated in Fig.

5.16. When the value of $\langle d \rangle$ in each section is represented by that at $x = 2, 5, 10, 15,$ and 20 mm in Fig. 5.14, $\dot{m}_{di}$ can be calculated by the following equation.

$$\dot{m}_{di} = \rho_l \cdot \left\{ \frac{4}{3} \pi \left(\frac{\langle d \rangle_i}{2} \right)^3 \right\} \cdot (F \cdot w_{lp} \cdot l_i) \cdot N_d \tag{12}$$

l_i and N_d denote the length of each section and the number of droplets produced in one event of bubble bursting. From the visualization images, it was found that $N_d \sim 1$, and the value of N_d for the calculation of $\dot{m}_{di}$ was tentatively determined to be 4, referring to the direct images in Fig. 5.5. Figure 5.21 shows the calculated results of $\dot{m}_{di}$ or $\dot{m}_{di}/\dot{m}$, in which $\dot{m}$ indicates the mass flow rate of the injected test liquid ($\dot{m} = 5.0$ g/s). Even though ΔT_{sup} in section 1 was higher than that in section 2 and 3, $\dot{m}_{d1}$ took the smallest value because $\langle d \rangle_1$ was the smallest. From section 2 to section 5, the value of $\dot{m}_{di}$ increased rapidly further downstream because the effects of ΔT_{sup} and $\langle d \rangle_i$ superimposed on $\dot{m}_{di}$. However, the ratio of the accumulated volume of dispersed droplets from each section to the injection flow rate of the test liquid $2\dot{m}_{di}/\dot{m}$ was less than 1%, and $\dot{m}_d/\dot{m}$ was reached only 2%. Consequently, it can be concluded that the total volume of dispersed droplets induced by the nucleate boiling from the liquid film is negligible against the injection flow rate of the liquid during jet impingement cooling.

5.4 Conclusions

To clarify the boiling induced atomization processes occurred in the liquid film through the wall impinging jet on the superheated wall, the fragmentation events were visualized via the magnified high-speed imaging with the backlight technique.

In the liquid film, two characteristic types of atomization processes were mainly visualized. One was that the large droplet pinched off from the ligament formed on the relatively high temperature wall (i.e., near the wetting front). The other was that the droplets were produced through the bubble bursting event in the nucleate boiling regime.

For the droplets from the bursting bubble produced by the nucleate boiling, the ejection velocity of the droplets was distributed around the local Weber number of unity and determined by the relationship between the inertia force of the ligament and the surface tension. The mean diameter of the droplets was characterized by the maximum radius of the bubble and bubble cap thickness. In addition, the further downstream, the larger droplets dispersed from the liquid film because the maximum bubble radius and

bubble cap thickness increased owing to the development of the thermal boundary layer and liquid film thickness along the flow direction.

The accumulated volume of the dispersed droplets from the rim of the liquid film increased further downstream because both the droplet size and frequency of bubble bursting increased. However, the loss of the liquid flow rate for cooling caused by the boiling induced atomization was negligible.

References

[1]   M. Ishii and Grolmes, M. A., "Inception criteria for droplet entrainment in two-phase concurrent film flow," *AIChE Journal*, vol. 21, no. 2, pp. 308-318, 1975.

[2]   S. R. Shine and S. S. Nidhi, "Review on film cooling of liquid rocket engines," *Propulsion and Power Research*, vol. 7, no. 1, pp. 1-18, 2018.

[3]   T. Ubara, H. Asano, and K. Sugimoto, "Heat transfer enhancement of falling film evaporation on a horizontal tube by thermal spray coating," *Applied Sciences (Switzerland)*, vol. 10, issue. 5, Article 1632, 2020.

[4]   J. Tabuchi, R. Firman, T. Okawa, K. Katono, H. Furuichi, and Y. Narushima, "Influence of various parameters on the onset criteria for boiling entrainment from a falling liquid film," *The Proceedings of the Thermal Engineering Conference*, Session ID 0073, 2021 (in Japanese).

[5]   J. G. Collier and J. R. Thome, "Convective boiling and condensation, third edition," *Clarendon Press*, 1994.

[6]   A. V. Cherdantsev, D. B. Hann, and B. J. Azzopardi, "Study of gas-sheared liquid film in horizontal rectangular duct using high-speed LIF technique: Three-dimensional wavy structure and its relation to liquid entrainment," *International Journal of Multiphase Flow*, vol. 67, pp. 52-64, 2014.

[7]   C. Shinan, Y. Weidong, S. Mengjie, L. Mengyao, and S. Qiyu, "Investigation on wavy characteristics of shear-driven water film using the planar laser induced fluorescence method," *International Journal of Multiphase Flow*, vol. 118, pp. 242-253, 2019.

[8]   C. Inoue and I. Maeda, "On the droplet entrainment from gas sheared liquid film," *Physics of Fluids*, vol. 33, Article 011705, 2021.

[9]   A. L. N. Moreira, A. S. Moita, and M. R. Panão, "Advances and challenges in explaining fuel spray impingement: How much of single droplet impact research is useful?," *Progress in Energy and Combustion Science*, vol. 36, no. 5, pp. 554-580, 2010.

[10] G. Liang and I. Mudawar, "Review of drop impact on heated walls," *International Journal of Heat and Mass Transfer*, vol. 106, pp. 103-126, 2017.

[11] M. Monde, "Heat Transfer Characteristics during Quench of High Temperature Solid," *Journal of Thermal Science and Technology*, vol. 3, no. 2, pp. 292–308, 2008.

[12] J. Breitenbach, J. Kissing, I. V. Roisman, and C. Tropea, "Characterization of secondary droplets during thermal atomization regime," *Experimental Thermal and Fluid Science*, vol. 98, pp. 516-522, 2018.

[13] V. P. Carey, "Liquid-vapor phase-change phenomena: an introduction to the thermophysics of vaporization and condensation processes in heat transfer equipment," *CRC Press*, 2018.

[14] D. C. Blanchard and L. D. Syzdek, "Film drop production as a function of bubble size," *Journal of Geophysical Research*, vol. 93, issue C4, pp. 3649-3654, 1988.

[15] F. E. C. Culick, "Comments on a Ruptured Soap Film," *Journal of Applied Physics*, vol. 31, no. 6, pp. 1128-1129, 1960.

[16] A. B. Pandit and J. F. Davidson, "Hydrodynamics of the rupture of thin liquid films," *Journal of Fluid Mechanics*, vol. 212, pp. 11-24, 1990.

[17] H. Lhuissier and E. Villermaux, "Bursting bubbles," *Physics of Fluids*, vol. 21, no. 9, pp. 1-2, 2009.

[18] H. Lhuissier and E. Villermaux, "Bursting bubble aerosols," *Journal of Fluid Mechanics*, vol. 696, pp. 5-44, 2012.
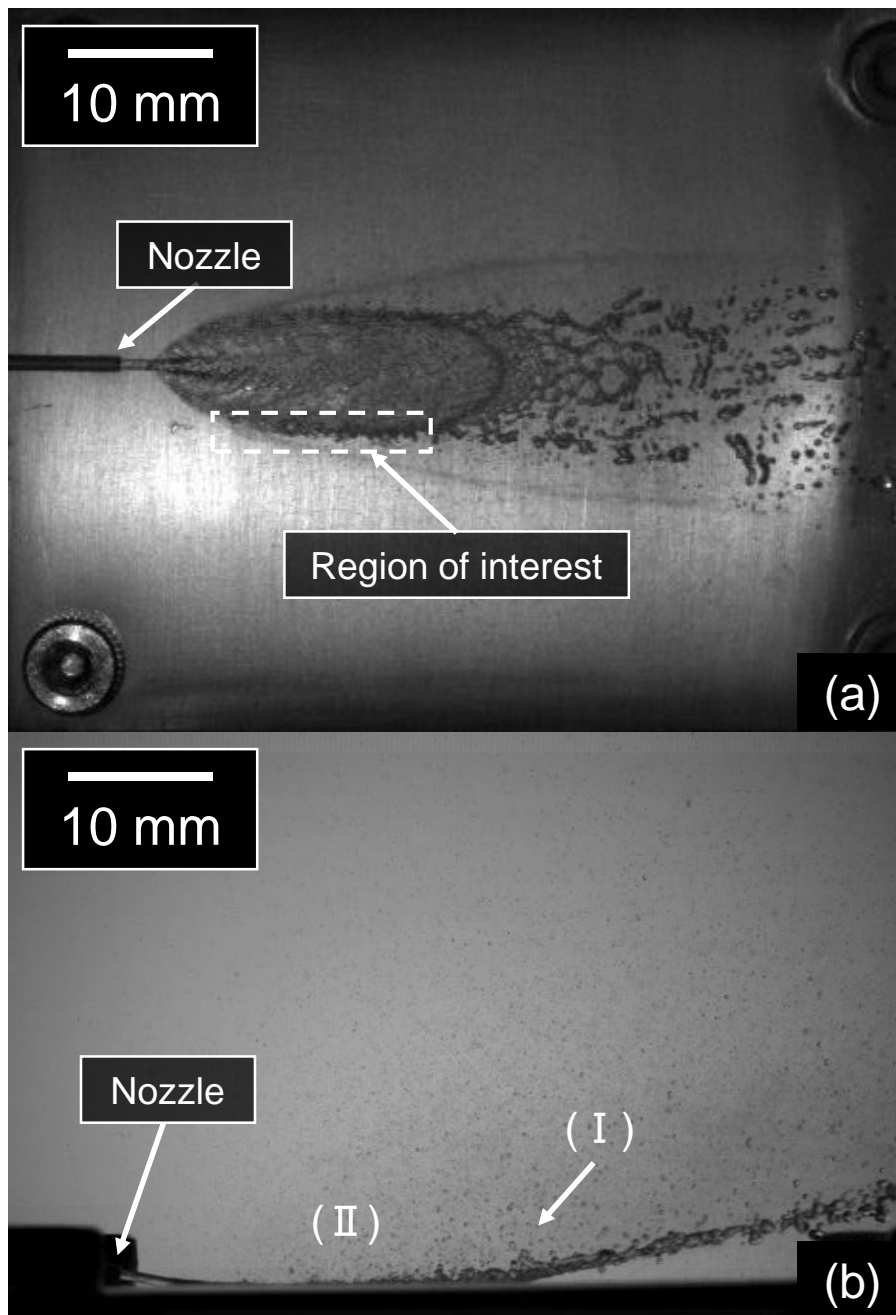
Fig. 5.1 Direct image of liquid film formed on a heated wall; (a) from top of the liquid film, (b) from side of the liquid film
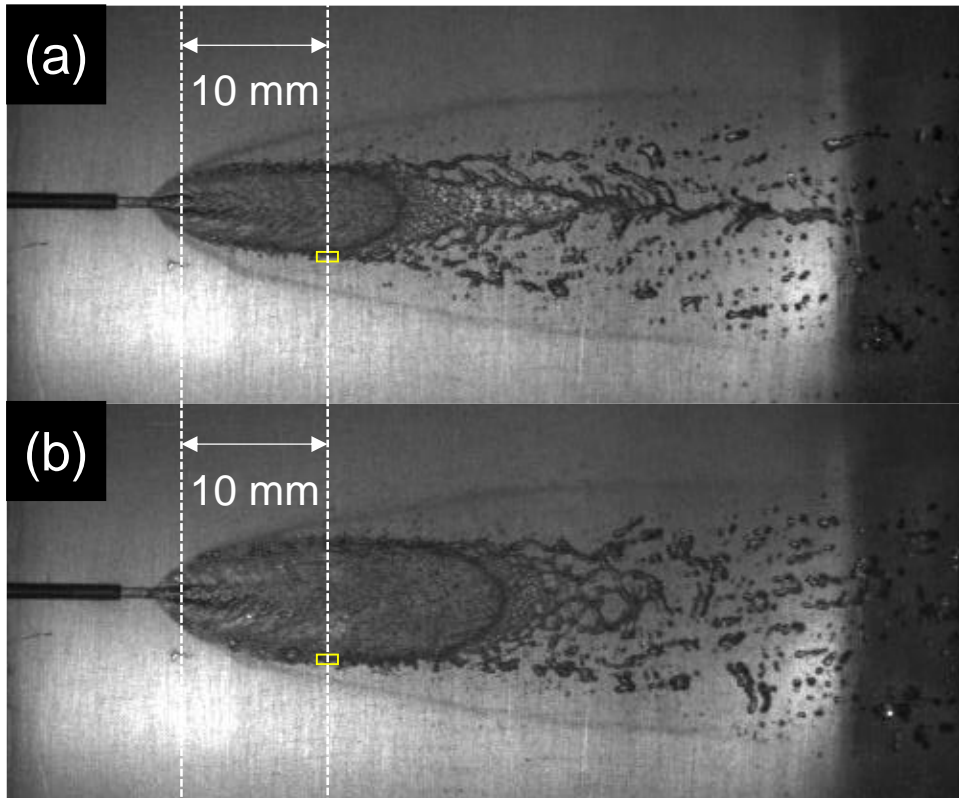
Fig. 5.2 Measurement position on a liquid film (a) 0.30 s after start of injection, (b) 0.50 s after start of injection
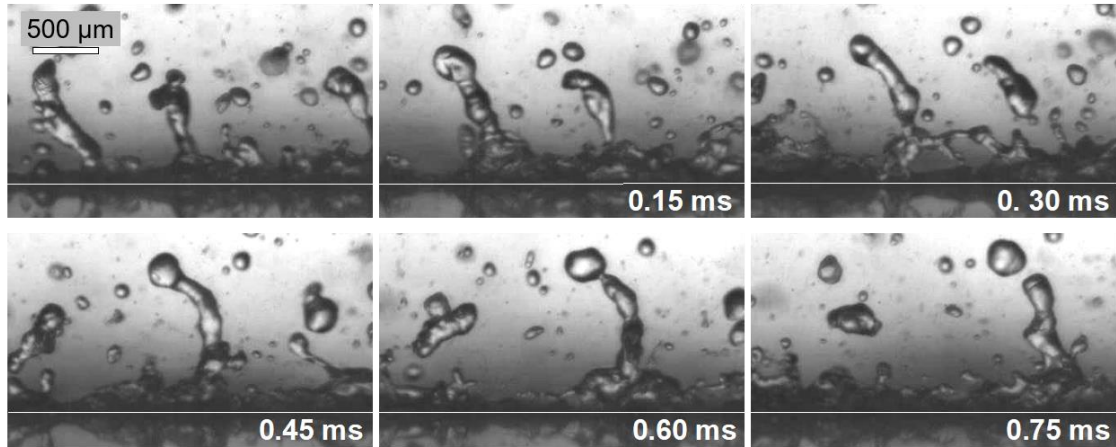
(a) Disintegration of droplets at the position near WF obtained at 0.3 s after start of injection
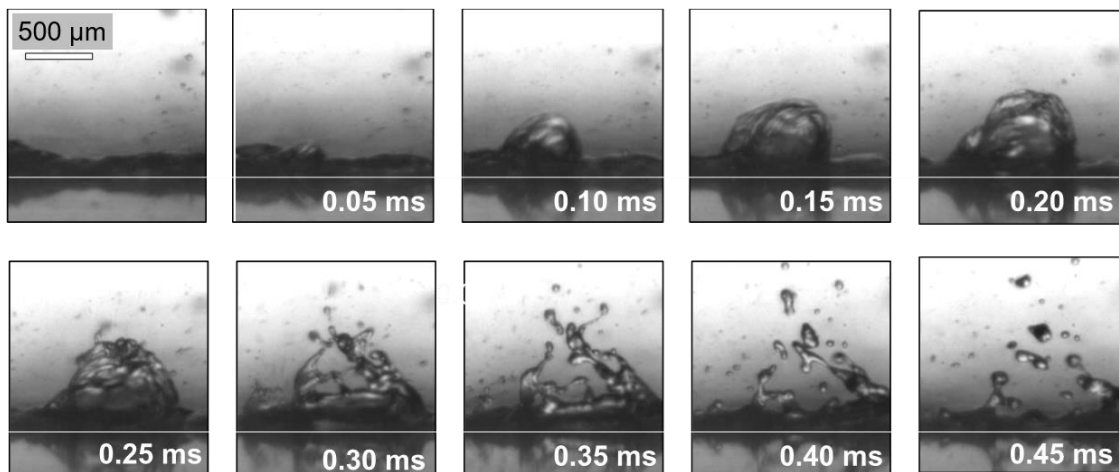
(b) Fragmentation via bubble bursting at the position away from WF obtained at 0.5 s after start of injection

Fig. 5.3 Time series of boiling induced atomization at different timing
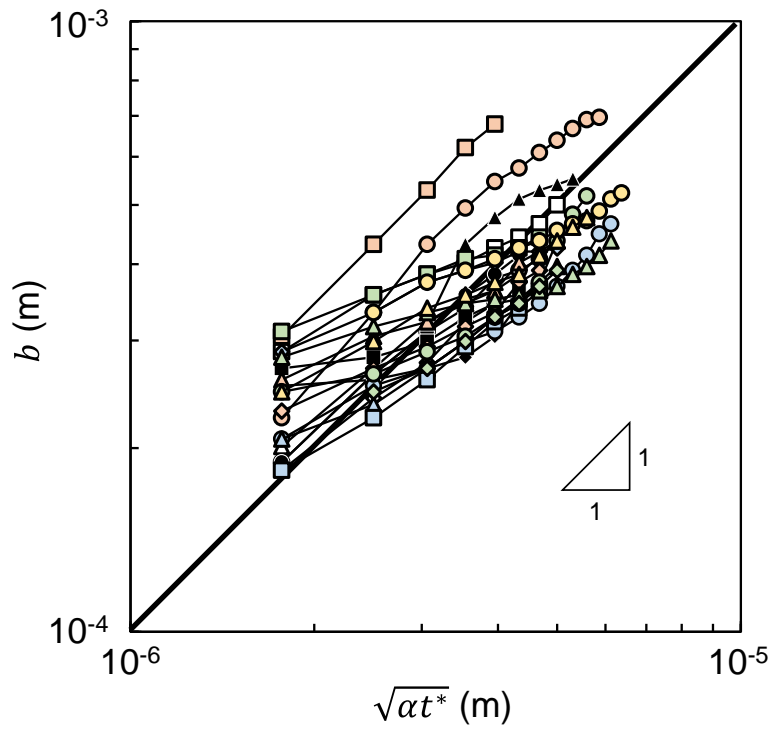
Fig. 5.4 Heat-transfer-governed bubble growth process
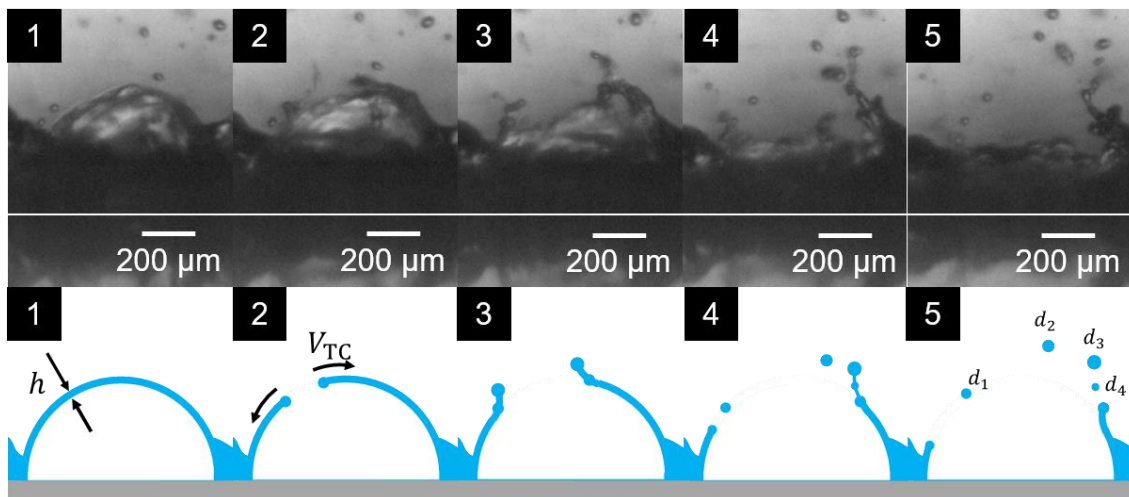
Fig. 5.5 Direct images and schematic illustration of fragmentation processes with bubble bursting for measuring Taylor-Culick velocity
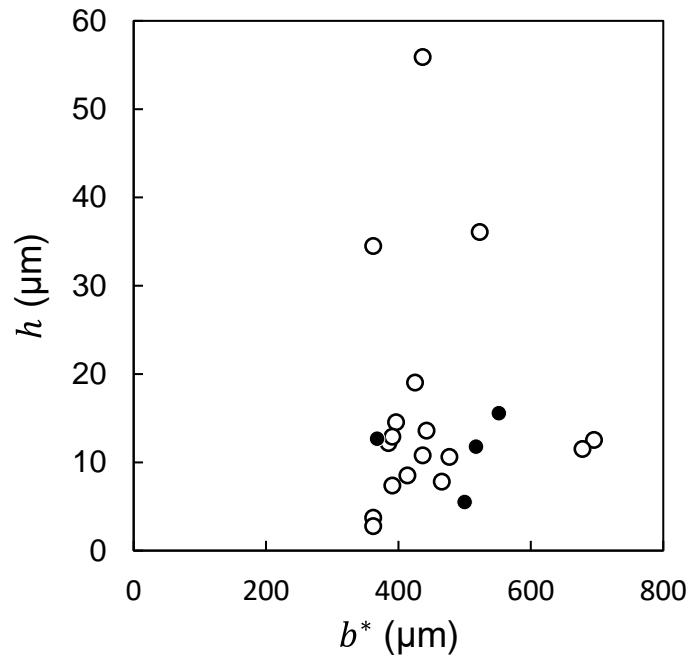
Fig. 5.6 Estimated value of thickness of bubble cap
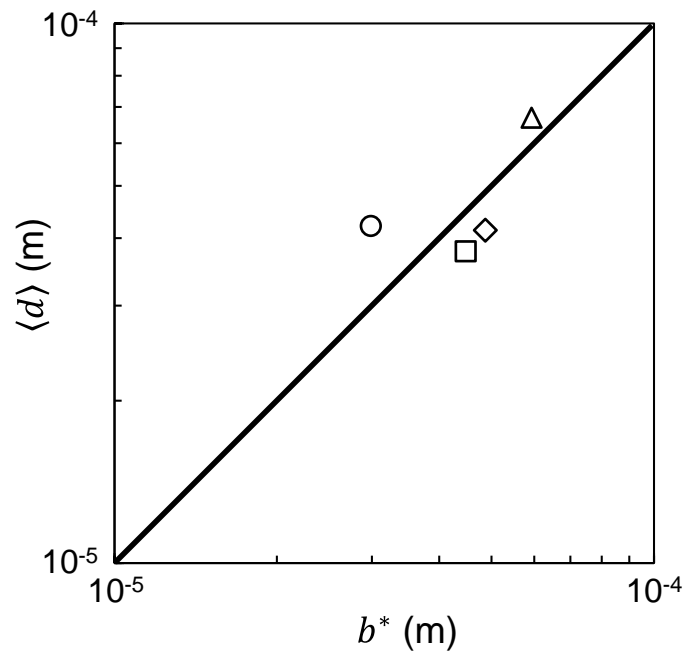
Fig. 5.7 Mean diameter of some droplets from bursting bubble at x = 10 mm. The bold line indicates Eq. (5.3).
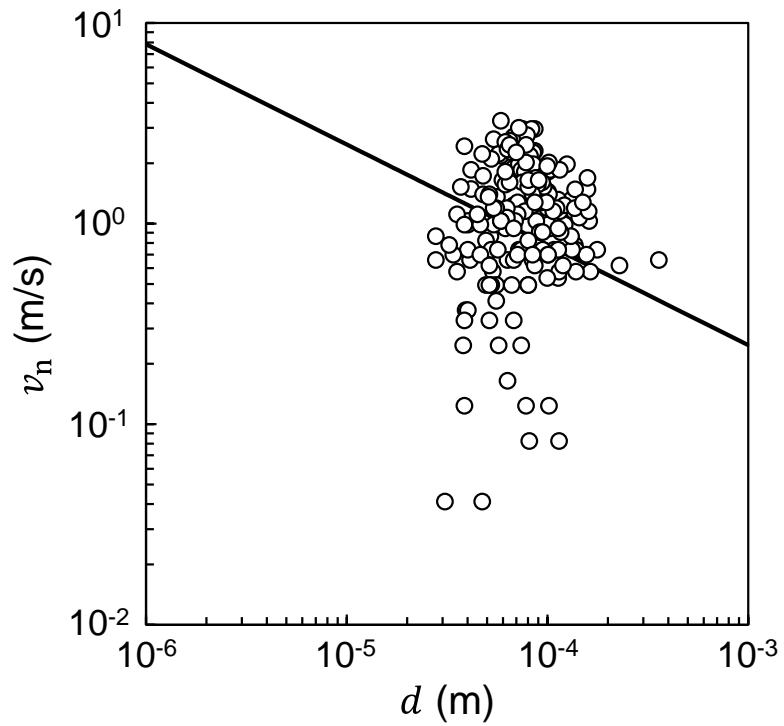
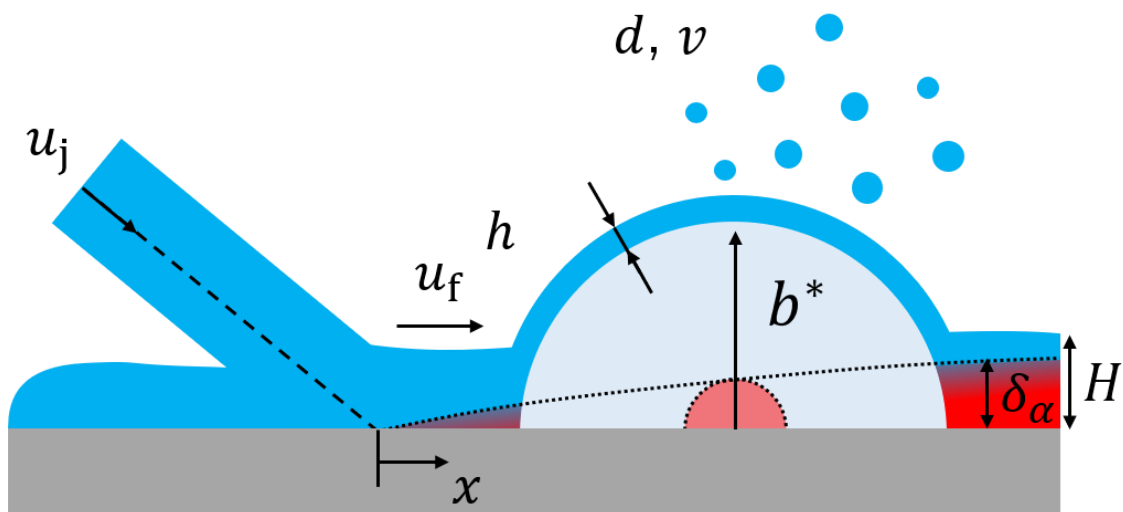Fig. 5.8 Relationship between ejection velocity and droplet diameter. The bold line indicates We defined by Eq. (5.4) of unity.

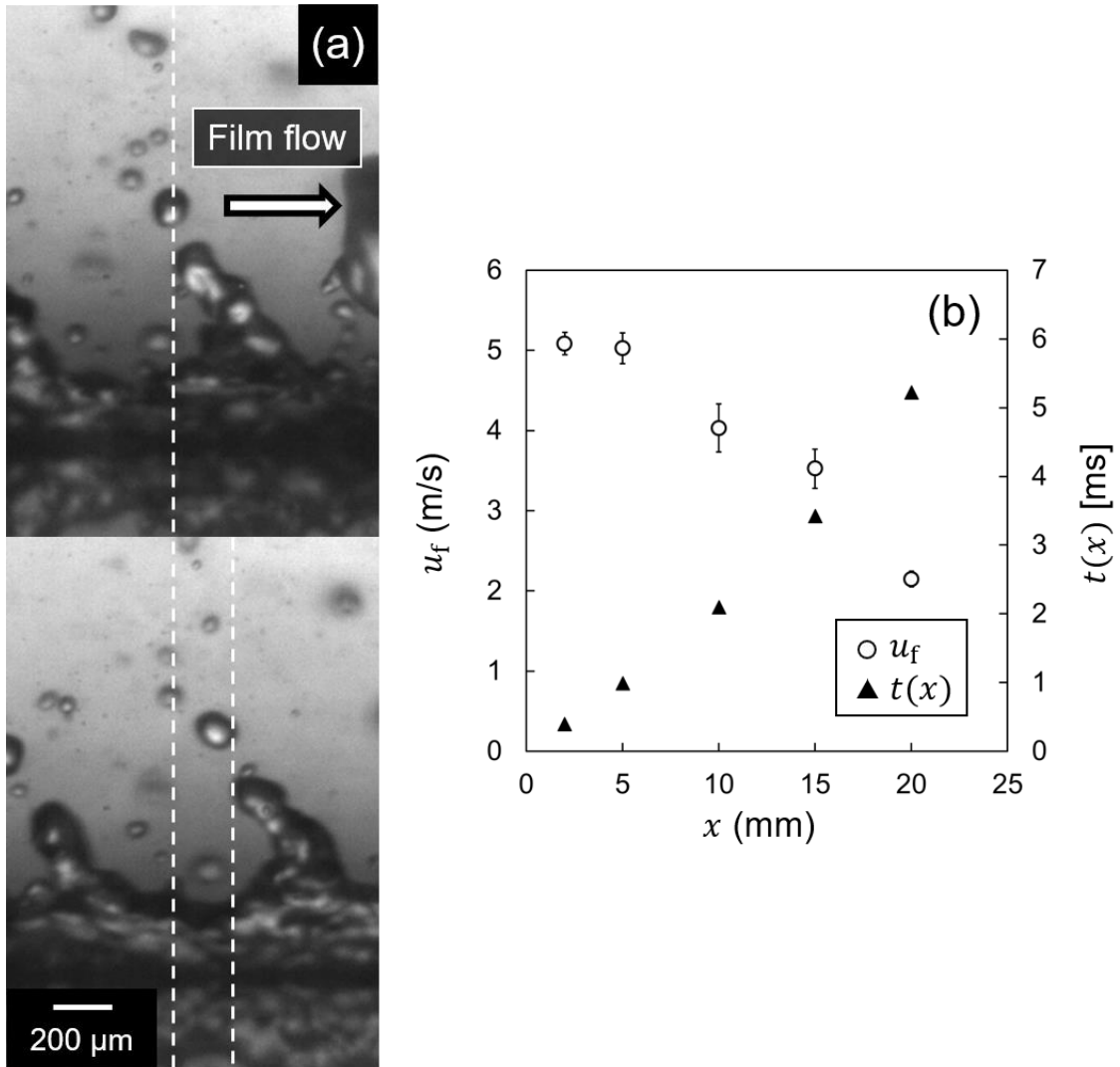Fig. 5.9 Schematic of nucleate boiling induced atomization appeared in a liquid film

Fig. 5.10 Magnified images of the ligament on the rim at a certain time (upper) and 5.56 μs after that time (bottom) (a) and liquid film velocity and calculated time required to reach at each position (b)
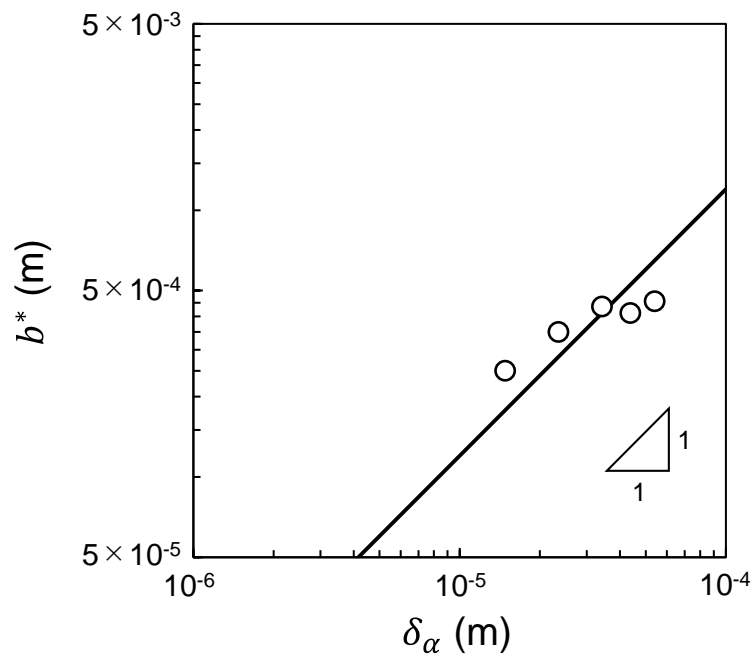
Fig. 5.11 Relationship between maximum bubble radius and thermal boundary layer thickness with a prefactor in Eq. (5.5) of 2. The bold line indicates Eq. (5.8).
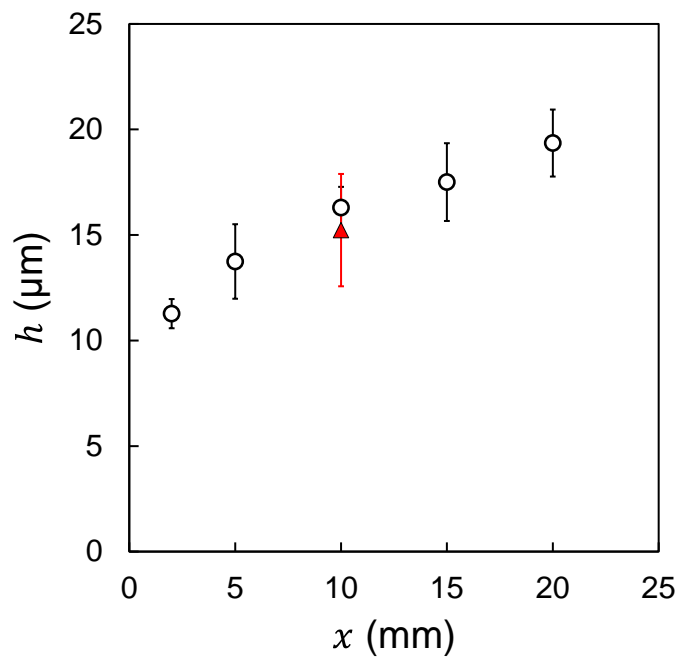

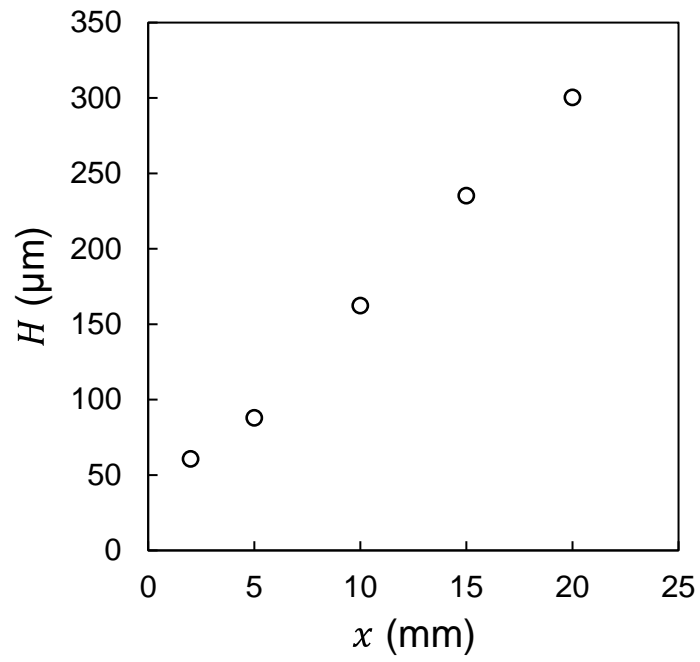Fig. 5.12 Change of bubble cap thickness along the flow direction of liquid film

Fig. 5.13 Distribution of liquid film thickness at the rim along the flow direction
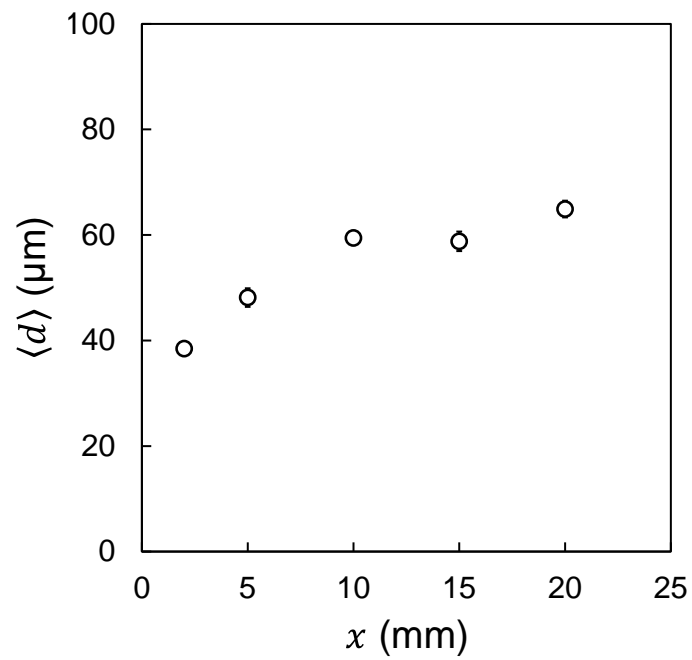

Fig. 5.14 Mean diameter of the droplets produced from the liquid film at each position
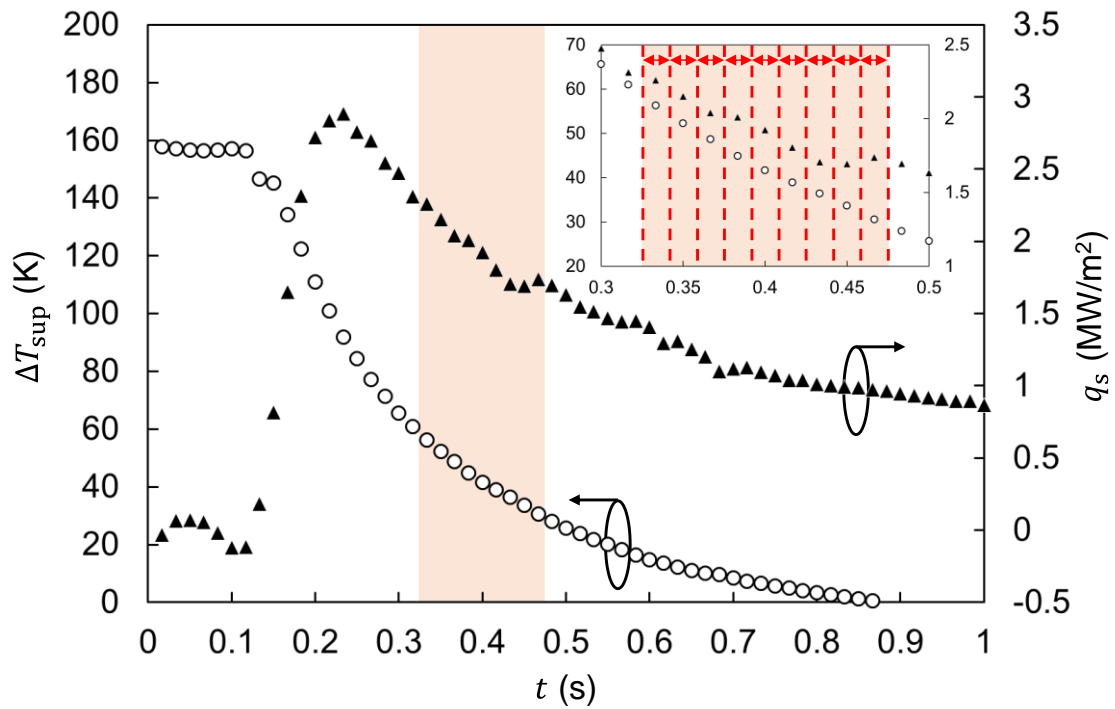
Fig. 5.15 Time history of degree of wall superheat and estimated surface heat flux

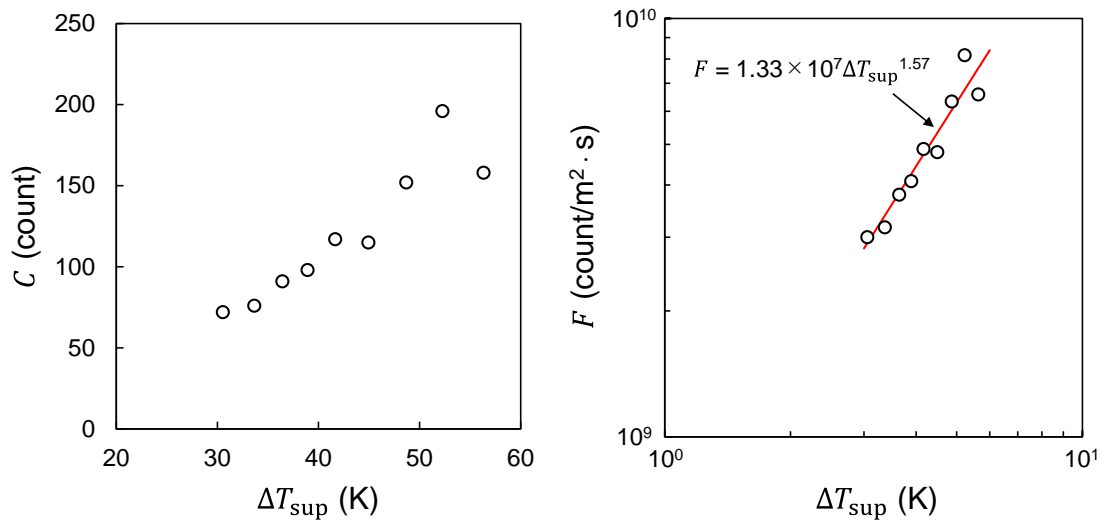$F = 1.33 \times 10^7 \Delta T_{\text{sup}}^{1.57}$

Fig. 5.16 Number and frequency of bubble bursting against degree of wall superheat
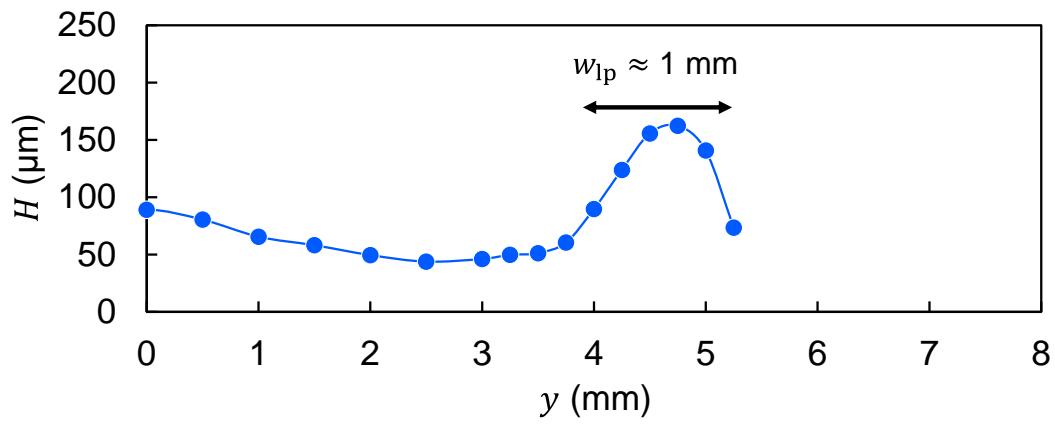
Fig. 5.17 Distribution of liquid film thickness in the y direction at $x = 10$ mm
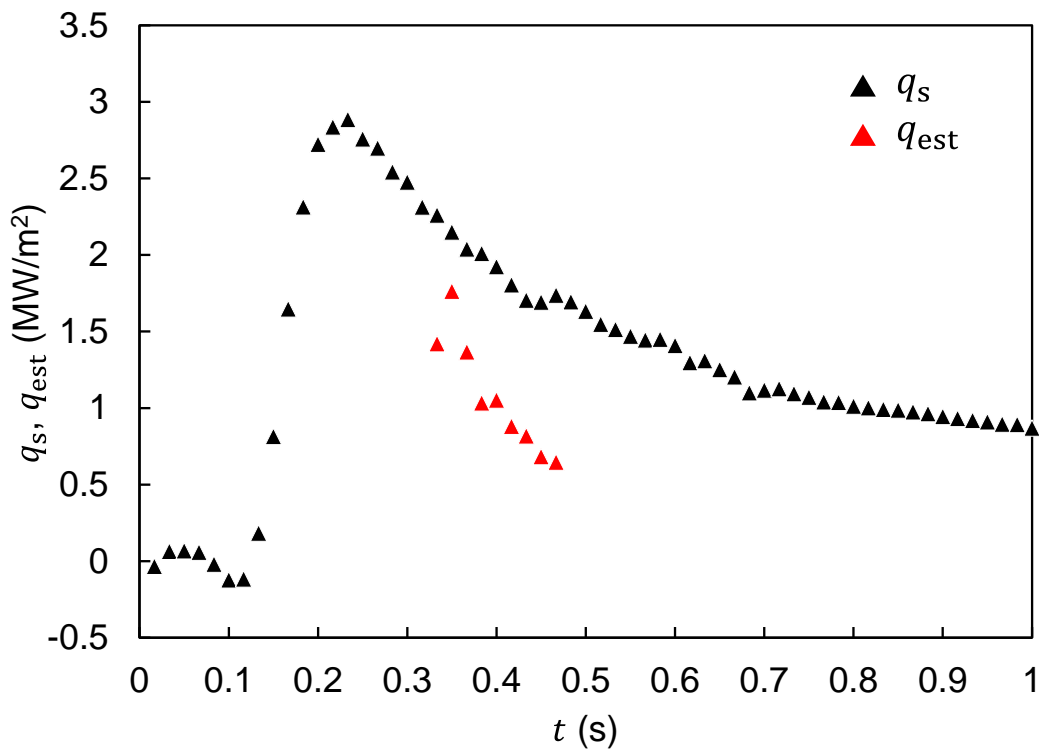
Fig. 5.18 Comparison of estimated surface heat flux and heat flux determined by frequency of bubble bursting and maximum bubble diameter
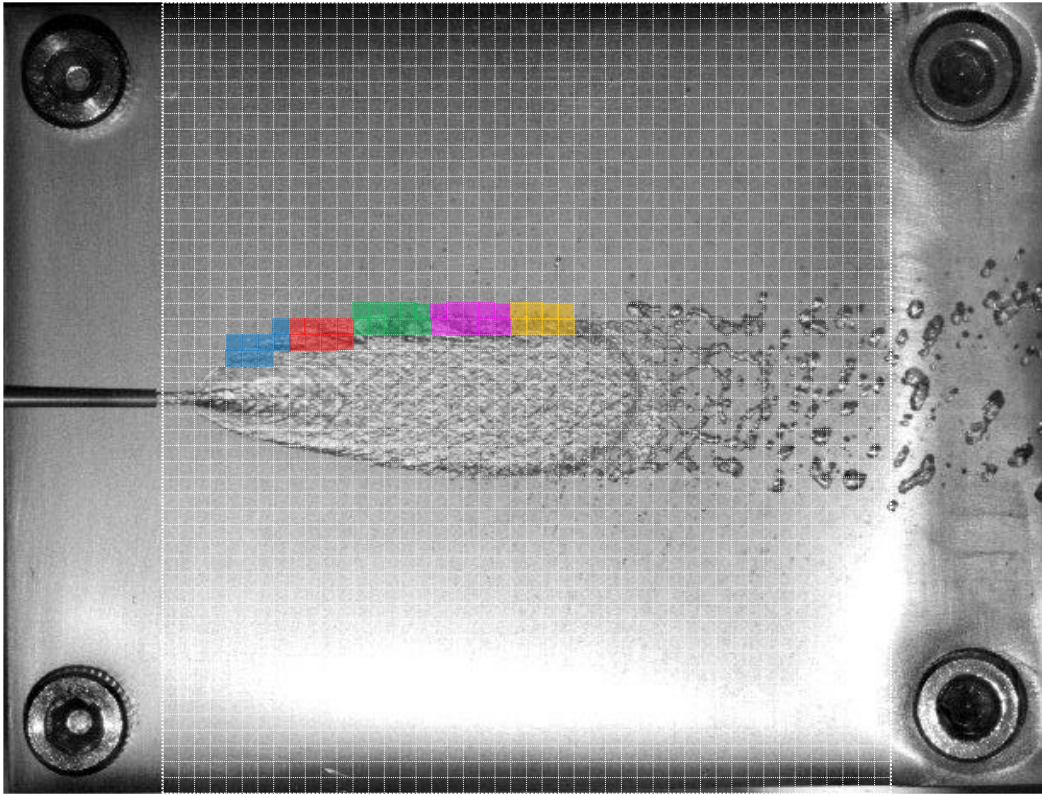
Fig. 5.19 Direct image of liquid film at $t = 0.6$ s taken from the top
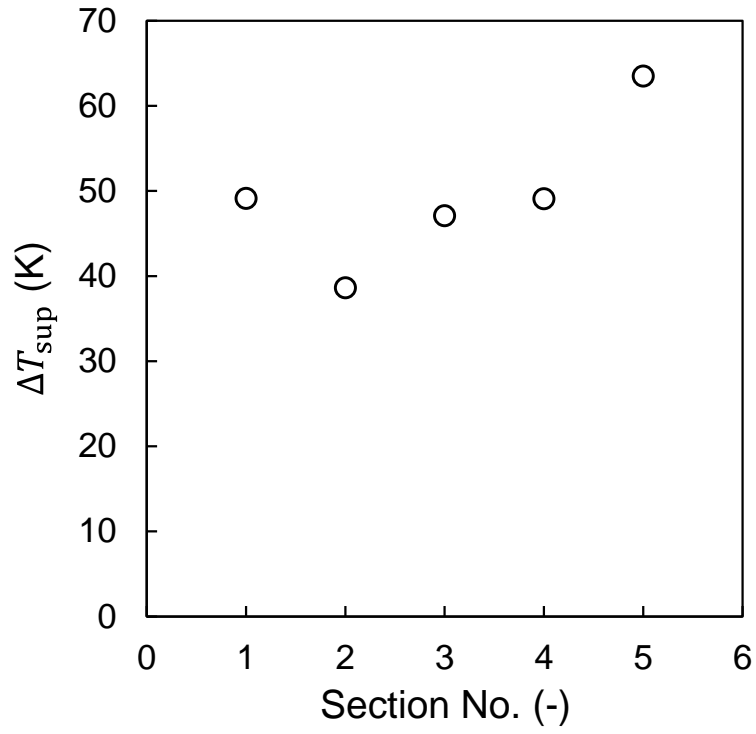
Fig. 5.20 Averaged value of degree of wall superheat in each section
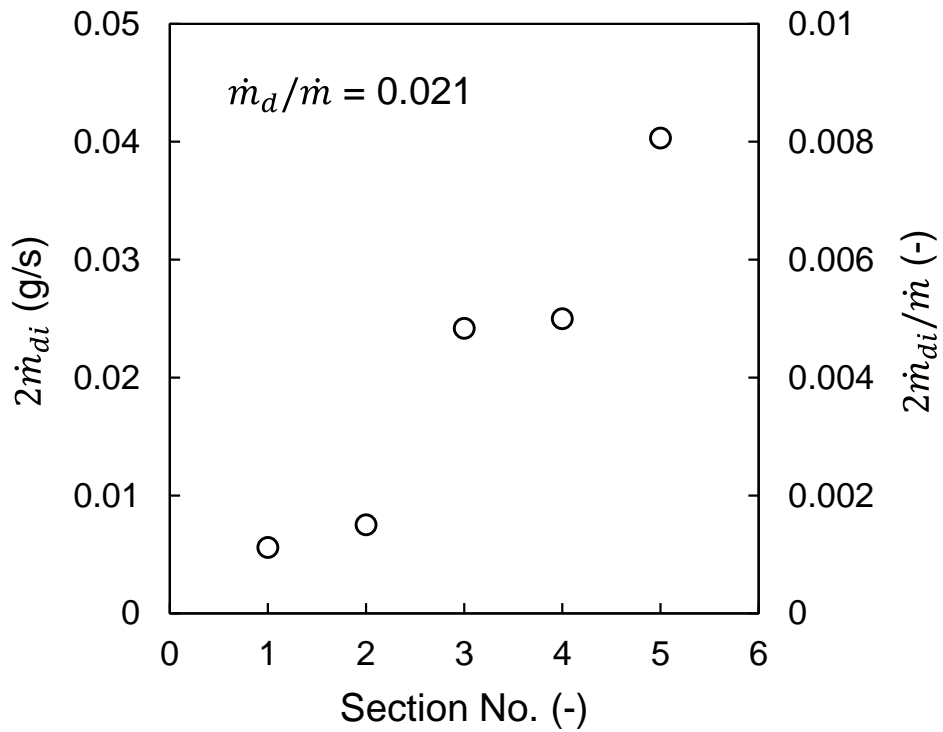
Fig. 5.21 Accumulated volume of scattered droplets from each section

Table 5.1 Experimental conditions and imaging conditions

Mass flow rate of test liquid	[g/s]	5.0
Nozzle diameter	[mm]	0.7
Impingement angle	[deg.]	10
Frame rate for magnified high-speed imaging	[fps]	20000, 54000
Frame rate for IR imaging	[fps]	60

Chapter 6 Summary and recommendations for future work

6.1 Summary

Bipropellant thrusters, which are used for attitude control and orbit maneuvering of small-scale spacecraft and satellites, employ a liquid film cooling technique, in which a part of the liquid fuel is injected onto the chamber wall to form liquid films, for avoiding thermal failure of the combustion chamber. To realize the reduction and optimization of the liquid fuel for liquid film cooling based not on the empirical knowledge or numerous combustion tests but on an understanding of the physical phenomena, a deeper understanding of the fundamental phenomena of liquid film cooling is in great demand.

In this study, the formation processes of liquid film and heat transfer characteristics between the formed liquid film and the heated chamber wall were experimentally and theoretically investigated to extract the key physical parameters which govern the liquid film formation.

In chapter 1, the background and the objective of this study is described through a literature review of the role of rocket engines in the space industry, the classification of rocket engines, overviews of the key physical phenomena inside the combustion chamber of bipropellant thrusters, and the previous studies on the liquid film formation processes.

In chapter 2, the liquid film distribution on a cold wall surface below the saturated temperature of the liquid was investigated by varying injection parameters including liquid flow rate, nozzle diameter, impingement angle, and liquid jet length to find out the key physical parameters to the formation of the liquid film. The main findings in chapter 2 are summarized as follows.
(1) When the liquid jet length became longer, the number of dispersed droplets increased near the impingement point of the liquid jet. However, the distance from the nozzle exit to the impinging point have no significant influence on the liquid film distribution when the distance is shorter than the breakup length.
(2) The maximum film width, which is one of the important length scales representing the liquid film distribution, increased with the increase in both the liquid jet velocity and impingement angle.
(3) The vertical component of the liquid jet velocity to the wall surface indicated a linear relationship with the maximum film width under each nozzle diameter condition. The

slope of the linear relationships was different with each nozzle diameter, which indicated the nozzle diameter was one of the factors affecting the film distribution.

(4) The maximum film width divided by the nozzle diameter could be uniformly organized in terms of the product of the Weber number and the sinusoid of the impingement angle, based on a dimensional analysis.

In chapter 3, the quenching of a heated metal plate with a spatial temperature gradient by continuous injection of a liquid jet was conducted to investigate the formation processes of the liquid film on a superheated surface. The visualization of the liquid film behavior by a high-speed camera and the temperature measurement of the metal plate by an infrared camera was synchronized to connect the liquid film state and the heat transfer characteristics. The effects of the liquid jet velocity and liquid flow rate on the liquid film formation were examined. The main findings in chapter 3 are summarized as follows.

(1) To estimate the temperature and heat flux on the cooled surface by the liquid film from the measurement temperature profile on the opposite surface, the numerical scheme for solving the inverse problem of the transient three-dimensional heat conduction was developed.

(2) The leading edge of the liquid film called the wetting front where a large amount of the liquid deflected from the wall surface appeared in the present study. The wetting front gradually propagated downstream, and the propagation velocity decreased as the wetting front moved downstream. The wetting front propagated faster with the increase in the liquid flow rate under each nozzle diameter condition.

(3) The wetting front propagation was governed by not the liquid jet velocity but the liquid flow rate, which suggested that the liquid flow rate, that is, the amount of the liquid supplied to the WF was significant to the faster propagation of the wetting front.

(4) The position of the wetting front was corresponded to the position where the temperature gradient along the flow direction of the liquid film took maximum value.

(5) The maximum value of the heat flux, which appeared in the vicinity of the wetting front, decreased as the wetting front moved downstream because the liquid film temperature increased further downstream. In addition, the maximum heat flux increased with an increase in the liquid flow rate because the liquid film temperature near the wetting front was lower owing to the higher heat capacity of the liquid film.

(6) Nearly 90% or more of the injected liquid was deflected away from the wall surface without evaporation.

In chapter 4, transient cooling of the superheated metal plate by intermittent injection of the liquid jet was conducted to obtain a better understanding of the liquid film behavior during the pulsed cooling processes. From the results in chapter 3, injection patterns under the same injection quantity of the liquid were examined on two types of metal plates (aluminum alloy and copper). The main findings in chapter 4 are summarized as follows.

(1) The trend of the wetting front propagation during the 1st injection duration was the same as that observed in chapter 3. During the injection stop period, the residual liquid film on the metal surface was consumed with nucleate boiling. In the present study, the wetting front propagated further downstream with each injection because the temperature rise of the metal plate during the injection stop period did not exceed the temperature drop during the previous injection period.

(2) The unsteady liquid film behavior and heat transfer characteristics during both the injection and injection stop period were successfully captured by measuring the change of the temperature distribution on the backside and the solution of the inverse heat conduction problem developed in chapter 3.

(3) In both of the plates, the longer injection period with the lower liquid flow rate was effective in the heat removal during the 1st period, in which boiling heat transfer was dominant for heat removal. In the aluminum alloy, the amount of the removed heat by the liquid film had a peak at a certain duty cycle because the metal temperature easily decreased owing to the lower thermal inertia and the cooling mode shifted from boiling to single-phase forced convection, especially in higher duty cycle conditions. On the other hand, for the copper plate, the tendency of the amount of the removed heat against the duty cycle in the 2nd and 3rd period was the same as that in the 1st period because the metal temperature did not easily decrease and the wetting front propagation was more suppressed in longer OFF time conditions due to the higher thermal diffusivity of the metal plate.

In chapter 5, the boiling induced atomization processes that appeared in the liquid film on a superheated surface were visualized via magnified high-speed imaging with the backlight technique to obtain information about the characteristic values of the dispersed droplets which may cause the reduction of the liquid film flow rate. The main findings in chapter 5 are summarized as follows.

(1) Two characteristic types of atomization processes were mainly visualized. One was that the large droplet pinched off from the ligament formed on the relatively high temperature wall (i.e., near the wetting front). The other was that the droplets were

produced through the bubble bursting event in the nucleate boiling regime.

(2) The ejection velocity of the droplets was distributed around the local Weber number of unity and determined by the relationship between the inertia force of the ligament and the surface tension.

(3) The droplet diameter produced via the bubble bursting event in the nucleate boiling regime was well characterized by both the maximum bubble diameter and the bubble cap thickness.

(4) The thermal boundary layer thickness was convinced as the characteristic length scale determining the amount of evaporation and the maximum bubble size. The bubble cap thickened further downstream. From these, the size of droplets produced via the bubble bursting became larger downstream.

(5) The accumulated amount of the dispersed droplets from the rim of the liquid film increased further downstream because both the droplet size and frequency of bubble bursting increased. However, the loss of the liquid flow rate for cooling caused by the boiling induced atomization was negligible.

As mentioned above, the results of experimental and theoretical analysis of the liquid film formation processes via an oblique jet impingement were summarized in this thesis. The findings obtained in the present study can lead to well-controlled thermal management and higher performance of bipropellant thrusters.

6.2 Recommendations for future work

As a final part of the thesis, the remaining issues of the present study and prospective of this research topic are discussed.

First, the remaining issues of the present study are listed below.

(1) The effects of the physical properties on the formation processes of the liquid film need to be investigated furthermore. For the liquid film distribution on a cold wall, the developed theoretical model predicting the maximum film width includes the term of the surface tension, and the effect should be investigated by using different working fluids or aqueous solutions. For the liquid film behavior and heat transfer characteristics of the liquid film, the effect of evaporation characteristics should be investigated because it affects both the heat transfer characteristics of the liquid film and the behavior of the residual liquid film during the pulsed cooling.

(2) The effects of the surface state on the formation processes and heat transfer

characteristics of the liquid film should be investigated. For the distribution of the liquid film on a cold wall, the data of the maximum film width obtained in this study indicate a trend slightly shallower slope than the theoretical model. One of the possible reasons is that the effect of the wettability did not include in the proposed model. The effect of wettability needs to be incorporate properly for the improvement of the model. For the liquid film behavior and heat transfer characteristics of the liquid film, the effects of both surface roughness and oxide film on the surface should be evaluated quantitively and modeled for being incorporated into the prediction of the liquid film length in bipropellant thrusters, because there is a piece of experimental evidence conducted by JAXA that the liquid film length was drastically changed when the wall surface state varied even though the injection condition of the propellant was the same.

(3) The most important issue is to elucidate the physical mechanism of why the liquid film is splashed away from a superheated surface. The mechanism of the wetting front needs to be modeled including the effects mentioned above and introduced for the theoretical model for predicting the liquid film length.

Finally, the prospectives of this research topic are discussed. In the present study, the existence of the fast combustion gas was neglected to investigate the liquid film/wall surface interaction in detail. As the next step of the present study, the liquid film behavior in the presence of a high-speed gas flow adjacent to liquid film should be investigated to understand the liquid film/fast gas interaction. For the cooling processes on a hot surface, there are two possible effects of the presence of high-speed gas flow that are thought to affect heat transfer characteristics. One is the reduction of the liquid film flow rate for cooling owing to the droplet entrainment induced by the liquid/gas interface instability. The other is that the liquid film flow becomes the Couette flow. When the velocity distribution in the liquid film changes, the temperature distribution also changes, which strongly affect the bubble dynamics for the boiling phenomena and the heat transfer characteristics between the liquid film and the wall. These possible effects should be investigated in detail and evaluated quantitively in future work.

List of publications

Chapter 2

[1] **Noritaka Sako**, Jun Hayashi, Yu Daimon, Hiroumi Tani, and Hiroshi Kawanabe, "Experimental analysis of the spreading of a liquid film on a bipropellant thruster chamber wall," *Journal of Thermal Science and Technology*, vol. 16, issue 1, pages JTST0008, 2021, https://doi.org/10.1299/jtst.2021jtst0008.

Chapter 3

[2] **Noritaka Sako**, Kouhei Noda, Jun Hayashi, Yu Daimon, and Hiroshi Kawanabe, "Quenching of a heated wall with spatial temperature gradient using a liquid film through oblique jet impingement," *International Journal of Heat and Mass Transfer*, vol. 192, Article 122925, 2022, https://doi.org/10.1016/j.ijheatmasstransfer.2022.122925.

Chapter 4

[3] **Noritaka Sako**, Kouhei Noda, Jun Hayashi, Yu Daimon, and Hiroshi Kawanabe, "Liquid film and heat transfer characteristics during superheated wall cooling via pulsed injection of a liquid jet," *International Journal of Heat and Mass Transfer*, vol. 205, Article 123934, 2023, https://doi.org/10.1016/j.ijheatmasstransfer.2023.123934.

Chapter 5

[4] **Noritaka Sako**, Jun Hayashi, Chihiro Inoue, Hiroshi Kawanabe, and Yu Daimon, "Boiling induced atomization appeared in the liquid film by wall impinging jet on the superheated wall," *Proceedings of International Conference on Liquid Atomization and Spray Systems ICLASS 2021*, Paper 287, 2021, https://doi.org/10.2218/iclass.2021.6007.

Others

[5] **Noritaka Sako**, Kouhei Noda, Jun Hayashi, Yu Daimon, and Hiroshi Kawanabe, "Heat Transfer Characteristics of Liquid Film Formed on a Superheated Wall during Pulsed Injection of Liquid Jet," *AIAA SCITECH 2023 Forum*, AIAA-2023-0512, 2023, https://doi.org/10.2514/6.2023-0512.

[6] Yu Daimon, Masaharu Nakajima, **Noritaka Sako**, Jun Hayashi, Hiroshi Kawanabe, and Himeko Yamamoto, "Laminar Diffusion Flame-holding Characteristics in Cross-flow Formed at the Wake of the Injector Post," *AIAA SCITECH 2023 Forum*, AIAA-2023-0901, 2023, https://doi.org/10.2514/6.2023-0901.

Conference papers

[1] **Noritaka Sako**, Jun Hayashi, Yu Daimon, Hiroumi Tani, and Hiroshi Kawanabe, "Visualization of Liquid Film for Film Cooling Formed on Combustion Chamber Wall of Bipropellant Thruster", *The Proceedings of the Second Pacific Rim Thermal Engineering Conference*, Maui, Hawaii, USA, 2019.

[2] **Noritaka Sako**, Kouhei Noda, Jun Hayashi, Yu Daimon, Hiroumi Tani, and Hiroshi Kawanabe, "Heat transfer characteristics of thin liquid film formed on a heated wall with spatial temperature gradient," *The Proceedings of the Thermal Engineering Conference*, Online, 2020 (in Japanese).

[3] **Noritaka Sako**, Kouhei Noda, Jun Hayashi, and Hiroshi Kawanabe, "STUDY ON LIQUID FILM COOLING BY WALL-IMPINGING JET IN A BIPROPELLANT THRUSTER," *The Proceedings of the 20th Seoul National – Kyoto – Tsinghua University Thermal Engineering Conference*, Online, 2020.

[4] **Noritaka Sako**, Jun Hayashi, Chihiro Inoue, Hiroshi Kawanabe, and Yu Daimon, "Nucleate boiling induced atomization appeared in the thin liquid film on the heated solid wall," *The Proceedings of the 29th ILASS-Japan Symposium*, Online, 2020 (in Japanese).

[5] Kouhei Noda, **Noritaka Sako**, Jun Hayashi, Yu Daimon, and Hiroshi Kawanabe, "Cooling of the Heated Wall Surface by Liquid Film during a Repetitive Pulsed

Injection of Liquid Jet," *The Proceedings of the Thermal Engineering Conference*, Online, 2021 (in Japanese).

[6] **Noritaka Sako**, Jun Hayashi, Hiroshi Kawanabe, Takahiro Sako, and Masashi Katsuki, "Numerical analysis on nitrogen origin of NOx formed in an ammonia/air flame," *The Proceedings of the 59th Symposium (Japanese) on Combustion*, Online, 2021 (in Japanese).

[7] Masaharu Nakajima, **Noritaka Sako**, Jun Hayashi, Yu Daimon, and Hiroshi Kawanabe, "Flammable characteristics of diffusion flame in the cross flow at the wake of step," *The Proceedings of the 59th Symposium (Japanese) on Combustion*, Online, 2021 (in Japanese).

[8] **Noritaka Sako**, Kouhei Noda, Jun Hayashi, and Hiroshi Kawanabe, "STUDY ON LIQUID FILM DEVELOPMENT AND ITS HEAT TRANSFER PROCESS THROUGH AN IMPINGING JET ON A SUPERHEATED WALL," *The Proceedings of the 21st Kyoto - Tsinghua - Seoul National University Thermal Engineering Conference*, Online, 2021.

[9] **Noritaka Sako**, Jun Hayashi, Chihiro Inoue, Hiroshi Kawanabe, and Yu Daimon, "Bubble bursting and subsequent fragmentation induced by nucleate boiling in a liquid film," *The Proceedings of the 30th ILASS-Japan Symposium*, Online, 2021 (in Japanese).

[10] **Noritaka Sako**, Jun Hayashi, Hiroshi Kawanabe, Takahiro Sako, and Masashi Katsuki, "Numerical analysis on formation characteristics of Fuel-NOx in $NH_3/CH_4/Air$ flame," *The Proceedings of the Thermal Engineering Conference*, Tokyo, Japan, 2022 (in Japanese).

[11] Masaharu Nakajima, **Noritaka Sako**, Jun Hayashi, Yu Daimon, and Hiroshi Kawanabe, "Effects of velocities of fuel and oxidizer on the flame stability of diffusion flame formed in crossflow," *The Proceedings of the Fluids Engineering Conference*, Kumamoto, Japan, 2022 (in Japanese).

Acknowledgement

I would like to deeply thank my supervisor, Prof. Hiroshi Kawanabe, for the endless support and constant guidance of my study from the 4th year undergraduate to the Doctoral course. Owing to his supervision, I was able to learn how to develop my research in a constructive manner and finally complete this thesis.

Besides my supervisor, I would like to express my sincerest gratitude to Prof. Jun Hayashi. His insightful comment and continuous encouragement helped me all through my research. In addition, valuable discussions with him broadened my horizons and improved the quality of my study.

In addition, I must thank Prof. Hitoshi Fujimoto and Associate Prof. Naoto Horibe for his insightful comments and hard questions which enabled my thesis to be improved. Especially, Associate Prof. Naoto Horibe also gave technical support and comments through my doctoral course.

I would like to express my special gratitude to Dr. Yu Daimon at JAXA for his continuous support and thoughtful advice for my research. I learned a lot as a researcher.

I also would like to thank Associate Prof. Chihiro Inoue at Kyushu Univ., Dr. Hiroumi Tani at JAXA (currently at Space X), and Emeritus Prof. Masashi Katsuki at Osaka Univ. for valuable discussions.

I am indebted to Mr. Kouhei Noda, Mr. Masaharu Nakajima, Mr. Kakeru Mizukoshi, Mr. Taishi Kataoka, and other students at Combustion and Power Engineering Laboratory who worked with me and gave powerful support through my doctoral course.

I also thank the officers, Mrs. Wakako Takamura and Mrs. Miki Okuyama. Their great support helped me to conduct my research so smoothly.

Last but not least, I would like to express my utmost gratitude to my family, Takahiro, Satoko, and Kaori for their warm love, understanding, encouragement, and support.

Noritaka Sako